SIMULATION AND EXPERIMENTAL STUDIES ON INDIRECT EVAPORATIVE COOLING SYSTEM WITH POROUS MATERIAL

SHI WENCHAO

PhD

The Hong Kong Polytechnic University

2023

The Hong Kong Polytechnic University

Department of Building Environment and Energy Engineering

SIMULATION AND EXPERIMENTAL STUDIES ON INDIRECT EVAPORATIVE COOLING SYSTEM WITH POROUS MATERIAL

Shi Wenchao

A thesis submitted in partial fulfilment of the requirements for the Degree of Doctor of Philosophy

June 2023

CERTIFICATE OF ORIGINALITY

I hereby declare that this thesis is my own work and that, to the best of my knowledge and belief, it reproduces no material previously published or written, nor material that has been accepted for the award of any other degree or diploma, except where due acknowledgement has been made in the text.

(Signed)

SHI WENCHAO (Name of student)

Abstract

Indirect evaporative cooling, an air-conditioning (AC) approach based on physical evaporation process, is one of the promising ways for energy saving of central air-conditioning systems, especially in dry-weather regions with low wet-bulb temperature. Researchers have recently established various simulation models with higher accuracy for different types of indirect evaporative coolers (IECs) and optimized the experimental schemes for both IECs and spraying systems. Existing studies show that reliable cooling performance can be guaranteed by stable and continuous water spraying on the secondary air channel surface. However, the water retention ability and wettability are usually unsatisfactory in the traditional IEC due to the effect of gravity and surface property. Because water can only transiently adhere to the vertical channel wall, the IEC has always been highly dependent on water spray systems, which consumes much energy, and thus limits further improvement of the system coefficient of performance (COP). It has been generally realized that more space needs to be provided for water storage, and porous material is promising for solving this problem because its small cavities are natural rooms for the liquid holdup. Accordingly, a novel plate-type cross-flow indirect evaporative cooler with porous material (PIEC) was newly proposed in this thesis. The developed porous structure in the IEC can effectively improve the water retention ability of the secondary air channel surface, which is beneficial to reducing the system's dependence on the water spraying system.

Firstly, the feasibility of using the porous material in the secondary air channel of the plate-type cross-flow IEC for liquid holdup was experimentally demonstrated, and the cooling performance of the PIEC was achieved under different spraying modes. The hybrid plate, comprising a porous nickel layer sintered on a stainless-steel sheet, was designed and manufactured. The porous nickel is to store water, while the smooth stainless-steel plate can

prevent water from seeping into the primary air channel. A water retention test was conducted for the hybrid plate, which showed that the sprayed water can be collected in the porous zone to support evaporation during the non-spraying period. Then, a cross-flow PIEC prototype assembled by hybrid plates was tested in the laboratory. Experimental results confirmed that the PIEC could not only cool the air under consistent spraying, but also keep the cooling effect for a period of time at the cost of a slight temperature rise when water spraying was interrupted, which indicates the relief of dependence on the spraying water.

Secondly, a three-dimensional (3-D) PIEC simulation model was established based on the computational fluid dynamics (CFD) approach to forecasting the cooling performance of the PIEC with different inlet air conditions under consistent and periodic spraying conditions. Results predicted by this 3-D model were compared with the data obtained from the previous experimental study for validation, which are in good agreement. Using this model, the temperature and humidity distributions in the PIEC were presented over time when intermittent spraying was implemented. In addition, the effects of various parameters on the dynamic variation of the primary air outlet temperature, average wet-bulb efficiencies, and non-spraying intervals have been quantitatively investigated.

Thirdly, considering the high computational requirements and resource consumption of the established 3-D PIEC model, response surface methodology (RSM)-based regression models were developed for this novel heat exchanger. These models were developed to forecast the system performance more simply under the consistent spraying and periodic spraying modes. The analysis of variance (ANOVA) was carried out for each response, and the influence of the single factors and interactive terms of the controllable parameters on the response was both revealed. In addition, a multi-objective optimization of the operating parameters of the PIEC has been achieved based on the desirability function approach.

Finally, the PIEC system performance was investigated and compared from the energy, exergy, and environmental (3E) perspectives under different spraying modes to exhibit the advantages of using the period spraying resulting from the application of porous media. Results show that the periodic spraying scheme can substantially improve the COP among the studied cases, albeit with minor temperature fluctuations. Furthermore, the periodic spraying mode increased exergy efficiency and reduced exergy loss ratio due to the decreased temperature potential difference in the primary air side and humidity potential difference in the secondary air side. Regarding the environmental benefits, the greenhouse gas emission of the PIEC in the periodic spraying scenarios is less than that under the conventional consistent spraying mode.

The key academic contributions derived from this thesis are summarized as follows: 1) A cross-flow PIEC was proposed to improve the liquid holdup on the secondary air channel surface so as to alleviate the dependence on consistent water spraying operations. 2) The feasibility of using the porous material and implementing the periodic spraying to replace the traditional consistent spraying were fully verified by the designed experiments. 3) The established 3-D model lays the foundation for predicting the PIEC performance under consistent and intermittent spraying conditions, and the RSM-based regression models of the selected responses offer a more straightforward approach for IEC performance forecasting and optimization. 4) The advantages of the period spraying operation resulting from using the porous media in the IEC were presented based on the performance comparison under the two spraying modes from 3E perspectives. Overall, the novel PIEC proposed in this thesis exhibits enhanced water retention ability and reduced dependence on spraying systems compared to traditional IECs, providing valuable insights for the development of next-generation IECs.

Keywords: Air conditioning; Indirect evaporative cooling; Porous material; Consistent and intermittent spraying strategies; Experiments; Simulation; Response surface methodology; 3E evaluation

Research output during Ph.D. study

Published papers (First or corresponding author):

1) H. Yang*, **W. Shi***, Y. Chen, and Y. Min, "Research development of indirect evaporative cooling technology: An updated review," *Renewable and Sustainable Energy Reviews,* vol. 145, p. 111082, 2021/07/01/ 2021

2) **W. Shi**, Y. Min, Y. Chen, and H. Yang, "Development of a three-dimensional numerical model of indirect evaporative cooler incorporating with air dehumidification," *International Journal of Heat and Mass Transfer,* vol. 185, 2022.

3) **W. Shi**, Y. Min, X. Ma, Y. Chen, and H. Yang, "Performance evaluation of a novel plate-type porous indirect evaporative cooling system: An experimental study," *Journal of Building Engineering,* vol. 48, p. 103898, 2022/05/01/ 2022.

4) **W. Shi**, Y. Min, X. Ma, Y. Chen, and H. Yang, "Dynamic performance evaluation of porous indirect evaporative cooling system with intermittent spraying strategies," *Applied Energy,* vol. 311, 2022.

5) **W. Shi**, X. Ma, Y. Gu, Y. Min, and H. Yang, "Indirect evaporative cooling maps of China: Optimal and quick performance identification based on a data-driven model," *Energy Conversion and Management,* vol. 268, p. 116047, 2022/09/15/ 2022.

6) **W. Shi**, H. Yang, X. Ma, and X. Liu, "A novel indirect evaporative cooler with porous media under dual spraying modes: A comparative analysis from energy, exergy, and environmental perspectives," *Journal of Building Engineering,* vol. 76, p. 106874, 2023/10/01/ 2023.

7) **W. Shi**, H. Yang, X. Ma, and X. Liu, "Techno-economic evaluation and environmental benefit of hybrid evaporative cooling system in hot-humid regions," Sustainable Cities and Society, vol. 97, p. 104735, 2023/10/01/ 2023.

Conference papers:

1) **W. Shi**, X. Ma, H. Yang. Numerical study of indirect evaporative cooler using porous media with dynamic time-dependent performance prediction. (Applied Energy Symposium: MIT A+B 2021)

2) **W. Shi**, H. Yang, X. Ma, X. Liu. Techno-economic evaluation and environmental benefit of hybrid evaporative cooling system in hot-humid regions. 3rd International Conference for Global Chinese Academia on Energy and Built Environment.

Published papers (co-author):

1) Y. Min, **W. Shi**, B. Shen, Y. Chen, and H. Yang, "Enhancing the cooling and dehumidification performance of indirect evaporative cooler by hydrophobic-coated primary air channels," *International Journal of Heat and Mass Transfer,* vol. 179, p. 121733, 2021/11/01/ 2021.
2) X. Ma, **W. Shi**, and H. Yang, "Study on water spraying distribution to improve the energy recovery performance of indirect evaporative coolers with nozzle arrangement optimization," *Applied Energy,* vol. 318, 2022.
3) Y. Min, Y. Chen, **W. Shi**, and H. Yang, "Applicability of indirect evaporative cooler for energy recovery in hot and humid areas: Comparison with heat recovery wheel," *Applied Energy,* vol. 287, 2021.
4) X. Ma, **W. Shi,** and H. Yang, "Improving the performance of indirect evaporative cooler for energy recovery from the perspective of nozzle configuration: A CFD model analysis," *Journal of Building Engineering,* vol. 76, p. 107195, 2023/10/01/ 2023.

On-going manuscripts (First author):

1) **W. Shi**, H. Yang, X. Ma, X. Liu. Performance prediction and optimization of cross-flow indirect evaporative cooler by regression model based on response surface methodology, Submitted to *Energy*, under 2nd review.

On-going manuscripts (Co-author):

1) X. Ma, **W. Shi**, and H. Yang, Spray parameter analysis and performance optimization of indirect evaporative cooler considering surface wettability, " Journal of Building Engineering. (With editor)

Projects and reports

1) H. Yang, Y. Min, **W. Shi**, and X. Ma. Study on Indirect Evaporative Cooling (IEC) Technology for Primary Air Handling Unit (PAU) (One-year project)

2) H. Yang, C. Qiu, and **W. Shi**. Study on energy-lighting-thermal comfort performance of vacuum glazing retrofitting for application in Hong Kong (One-year project)

<u>Invention patent application:</u>

H. Yang, **W. Shi**, Y. Chen, Y. Min, and X. Ma, A cross-flow plate-type heat exchanger with intermittent spraying and indirect evaporative cooling unit (Application No.: 202210816233.3; under review - In Chinese)

<u>Draft of research proposals:</u>

1) Development of solar photovoltaic integrated vacuum glazing technology for energy saving in buildings. BEEE Research Fund, 2023.
2) Research and development of energy saving and fire prevention of vacuum glazing technology for application in buildings. Green Tech Fund of Hong Kong (Third round), 2022-2023.

Acknowledgements

It is my great honor and pleasure to take this valuable opportunity to express my sincere appreciation for the selfless and help from my chief supervisor - Prof. Yang Hongxing, co-supervisor - Prof. Lu Lin, and student-attachment host supervisor - Prof. Liu Xiaohua.

Firstly and foremost, I would like to express my most sincere appreciation and gratitude to my chief supervisor, Prof. Yang Hongxing. I can always receive the warmest support and help from him when I suffer from difficulties in work and life. His expert guidance, continuous encouragement, and constant support provide a solid foundation for my current thesis and also future research career.

It is also my honor to show my appreciation to Prof. Lu Lin. Thanks so much for her valuable suggestions and insightful view on this research.

My sincerest gratitude also goes to Prof. Liu Xiaohua and all her research group members, who gave me the best opportunity and a lot of guidance both in my research and life career during the student attachment program at Tsinghua University.

Furthermore, I would like to express my thanks to all the members in the Renewable Energy Research Group (RERG) for their help and companion, in particular Dr. Chen Yi, Dr. Min Yunran, Dr. Chen Jianheng, and Dr. Wang Qiliang. I also would like to give my appreciation to the staff and the technicians for their great support.

I also appreciate the financial support from The Hong Kong Polytechnic University and two General Research Funding Projects (Ref. No.: 15213219 and 15200420). It would be impossible to complete my Ph.D. study without strong financial support from them.

Finally, I would like to give my special thanks to my beloved parents for their sacrifice for me without expecting any return. Without their considerate support and deep love, it is impossible for me to accomplish my Ph.D. study.

Table of content

List of figures in the thesis

List of tables in the thesis

Nomenclature

a_w	Water activity
c	Molar concentration of gas, kg/m^3
c_{pa}	Specific heat of air, J/(kg·°C)
c_{pw}	Specific heat of water, J/(kg·°C)
C	Mass concentration, mol/m^3
D_{cap}	Capillary diffusivity, m^2/s
D_{va}	Diffusivity between vapor and air, m^2/s
d	Channel gap, m
d_e	hydraulic diameter of channel, m
d_{por}	Average pore diameter, um
f_{Re}	Friction coefficient
g	Acceleration of gravity, m/s^2
H	Height of cooler, m
H_{loss}	Water head loss, m
h	Heat transfer coefficient, W/(m^2 ·°C)
h_{fg}	Latent heat of vaporization of water, J/kg
h_m	Mass transfer coefficient, kg/ (m^2 ·s)
i	Enthalpy, kJ/kg
k	Thermal conductivity, W/(m·K)
L	Length of cooler, m
M	Molecular weight, kg/mol
M_{db}	Dry basis Moisture content, kg/kg
M_{wb}	Wet basis Moisture content, kg/kg

m	Mass flow rate, kg/(m^3·s)
m_{ratio}	Ratio of primary to secondary air flow volume
$\boldsymbol{n}$	Mass flux, kg/(m^2·s)
Nu	Nusselt number
P	Pressure, pa
Pr	Prandtl number
Q	Cooling capacity, W
R	Gas constant, J/(mol·K)
Re	Reynolds number
S	Saturation
Sh	Sherwood number
T	Temperature, K
t	Temperature, ℃
U	Uncertainty
u,v,w	Velocity on the x, y, z coordinate directions, m/s
V	Air volumetric flowrate, m^3/s
W	Power, W

Greek symbols

ω	Moisture content of air, g/kg
δ	Thickness, mm
θ	Dimensionless temperature
λ	Thermal conductivity W/(m·℃)
ρ	Density, kg/m^3
μ	Dynamic viscosity, Pa·s

υ	Kinematic viscosity, m^2/s
η	Effectiveness
ε_{en}	Enlargement coefficient
δ	Thickness, mm
ε	Porosity
κ	Absolute permeability, m^2
κ_r	Relative permeability
τ	Time, s

Subscripts

p	Primary air channel
s	Secondary air channel
c	Cooling
a	Air
dew	Dew point
ev	Evaporation
g	Gas phase
ir	Irreducible
in	Inlet air
l	Liquid phase

out	Outlet air
s	Solid phase
sat	Saturated value
sf	Surface
v	Vapor
w	Water film
wb	Wet-bulb

Abbreviation

1/2/3-D	One/two/three dimensional
AC	Air conditioning
CFD	Computational fluid dynamics
COP	Coefficient of performance
DEC	Direct evaporative cooling
DPIEC	Dew point indirect evaporative cooler
DWC	Dropwise condensation
EC	Evaporative cooling
Exp.	Experiment
FWC	Filmwise condensation
IEC	Indirect evaporative cooler
LDD	Liquid desiccant dehumidifier
NTU	Number of transfer unit

PC	Passive cooling
PUA	Packaged unit of air conditioner
PIEC	Indirect evaporative cooler with porous media on secondary channel wall
RIEC	Regenerative indirect evaporative cooler
RH	Relative humidity
Sim.	Simulation
VCRS	Vapor compression refrigeration system

Chapter 1 Background and Introduction

1.1 Background

Achieving the carbon peak and carbon neutrality requires the transformation of the energy system and the reduction of energy use [1]. Building energy consumption accounts for 40% of the total primary energy consumption in developed economies [2]. One of the main drivers of increased building energy use is the trend toward equipment electrification. With the rise of technology and automation in buildings, more and more energy systems are being powered by electricity, from lighting and heating, ventilation and air conditioning (HVAC) systems to appliances and electronics. Another factor that has contributed to increased building energy consumption is climate change [3]. Due to temperature rise from global warming, buildings require more energy to maintain comfortable indoor environment, particularly in hot and humid climates. This has led to a surge in demand for air conditioning, which is one of the most energy-intensive building systems. Additionally, greater affordability for consumers has contributed to increased energy consumption in buildings.

The swift expansion of the construction sector poses a potential pressure on the goal of reaching peak CO_2 emissions by 2030 in mainland China [4], and failing to meet this target could lead to undue strain on the energy supply system [5]. These circumstances highlight the importance to employ rigorous energy-efficient approaches in building sectors. In Hong Kong, as shown in Fig. 1.1.1, the building sector consumes 90% of total electricity and correspond to over 60% of total carbon emissions [6]. Different building service systems provide various functions for human activities, while 31% of the electricity consumption for air conditioning (AC) system is still the most significant energy consumer among all items, which is followed by refrigeration and lighting.

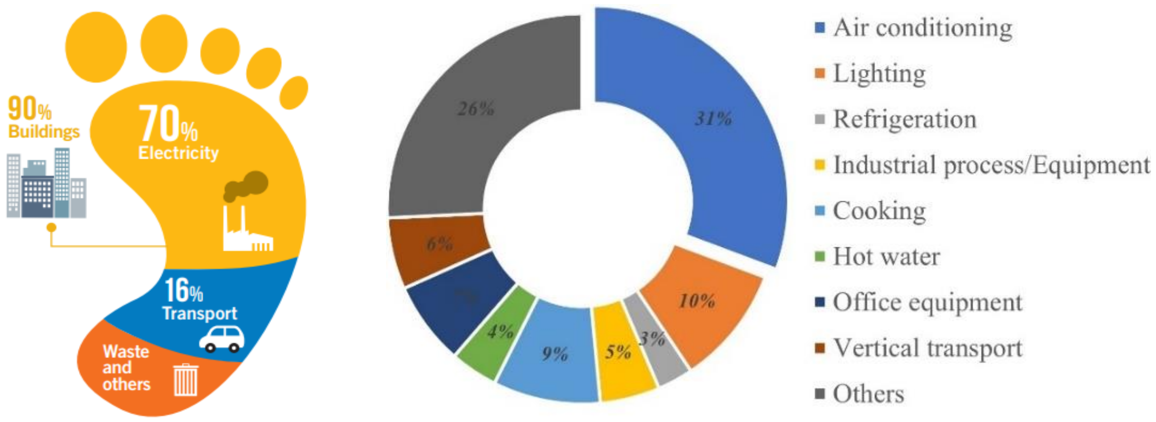

(a) (b)

Fig. 1.1.1 (a) Electricity generation - the largest source of local carbon emission (b) Electricity consumption by end-user in Hong Kong

The AC system regulates indoor thermal comfort and provides fresh air for indoor personnel. However, with the wider application of mechanical vapor compression (MVC) devices, it consumes much more energy. According to the International Energy Agency (IEA), adopting efficient cooling scenarios can almost halve energy consumption for AC, reducing investment and operating costs by 3 trillion US dollars between now and 2050. As a large energy consumer, it should be considered as one of the main building service systems for energy-saving, integrating energy-efficient and environmental-friendly technologies. In addition to relying on advanced or complex control strategies and variable drive technologies, some scholars are focusing on the daily physical process of handling hot fresh air. Evaporative cooling is one promising technology for achieving sustainable cooling (EC), which uses water evaporation to remove heat from the indoor environment. EC has several advantages compared with traditional MVC systems, including low energy consumption, low greenhouse gas emissions, and the absence of harmful refrigerants [7]. Direct evaporative cooling (DEC) is limitedly applied because the air cooling is obtained at the cost of humidity increase, while indirect evaporative cooling (IEC) can cool the fresh air without increasing the moisture content, which is more in line with occupant comfort requirements [8, 9]. The development of the IEC technology dates back to the early 20th century, with the first patent for this technology in 1906 [10, 11]. However, it was not until the 1980s that this technology gained popularity due to increasing concerns about energy conservation and sustainable cooling design in buildings. In the next section, the basic working principle of this sustainable passive cooling approach is introduced.

1.2 Introduction of indirect evaporative cooling

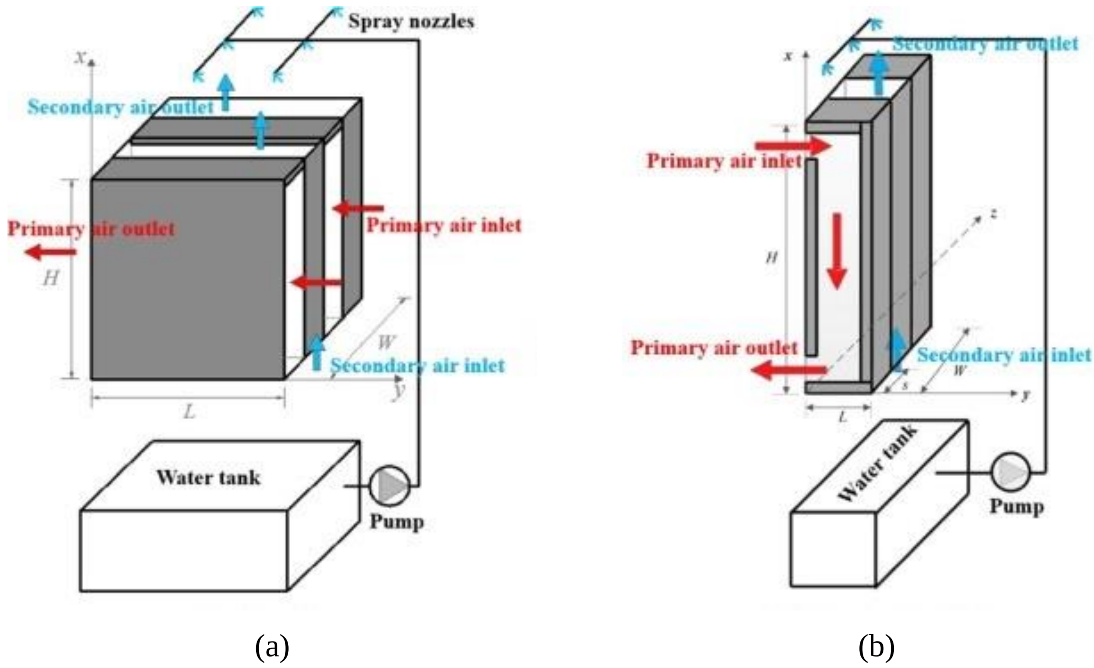

Fig. 1.2.1 The working principle and configuration of (a) cross-flow (b) counter-flow IEC system

Fig. 1.2.1 presents the working principle and basic components of the counter-flow and the cross-flow IEC system [12]. The system includes a pair of channels: the primary air channel and the secondary air channel, which can also be called dry channel and wet channel. The primary air channel serves as the supply air (fresh air), while the secondary air channel is the working air. A water tank, water pump, and several spraying nozzles consist of the water spraying system [13]. The water pump delivers the water from the bottom of the water reservoir to the top nozzles, which spray and moisturize the surfaces of the secondary air channel. The water membrane surface can be regarded as saturation. When the air passes over the water film surface in the wet channel, the evaporation process occurs because of the moisture content difference, which removes the latent heat at the same time. Hence, the plate can be chilled so as to cool the air in the dry channel through convective heat transfer. In recent years, IEC has been closely related to various fields. As a passive cooling (PC) technology, it could be employed for cooling production, energy recovery, and ventilation in buildings [14-16]. In addition to being utilized as the AC system in buildings, the integrated IEC system can be used for seawater desalination with proper modifications and combinations with other equipment [17, 18], and it has also been revealed to supply the cool air for the agricultural food storage and the battery thermal management issues [19, 20].

Initially, both primary and secondary air in the IEC unit are sourced from the outdoor environment, thereby making it a suitable option for hot-dry regions, and a promising alternative to traditional mechanical cooling systems [21]. However, the status of outdoor air usually fluctuates with time, and the cooling effect of the IEC is deficient when the wet-bulb temperature of secondary air is high. In addition, the IEC unit is generally placed vertically, and water cannot be well kept on the board due to the gravity, which requires continuous spraying to form the liquid film so as to maintain a stable cooling performance. The continuous spray of water pump consumes electric energy, and this has hindered the performance of the IEC system, limiting its widespread adoption in the HVAC field.

1.3 Organization of the thesis

This thesis presents a detailed study into a novel cross-flow plate-type indirect evaporative cooler with porous material integrated into the secondary air channel surface (PIEC), and elaborates the research processes and outputs. The detailed configurations of this thesis are illustrated as follows:

Chapter 2 provides a comprehensive review of the latest research progress in the field of indirect evaporative cooling (IEC) technology. The review is mainly conducted on different types of IECs and innovative embedded structures, common materials used for manufacturing IEC units, and the enhancement of the spraying system. Based on the review, the research gaps and objectives of this thesis are accordingly identified.

In Chapter 3, a PIEC prototype is designed and manufactured. The cooling performance of the PIEC system is investigated using a test rig established at the PolyU laboratory. The experimental procedures, test rig design and establishment, and manufacturing of the PIEC prototype are described in detail. The experiments of the PIEC system are evaluated under steady-state and dynamic-state conditions, and the results are analyzed and presented.

In Chapter 4, a three-dimensional (3-D) model is developed to predict the PIEC performance under consistent spraying and intermittent spraying modes using the computational fluid dynamics (CFD) approach. The model is validated by the experimental data obtained in Chapter 3. The temperature and humidity distribution in the PIEC are presented over time, and the influences of essential parameters on the performance are analyzed using this model. Based on the temperature rise threshold required to restart the water spraying in the secondary air channel, the temperature cycles are exhibited as well.

Chapter 5 proposes the regression model based on the response surface methodology (RSM) for a quick and straightforward prediction of the PIEC performance, and the empirical equations under the two spraying modes are accordingly formulated. Multi-optimizations are conducted for the adjustable parameters based on the desirability function approach.

In Chapter 6, the energy, exergy, and environmental (3E) comparisons for the PIEC system are conducted between traditional consistent spraying and the newly proposed periodic spraying modes. Eventually, Chapter 7 summarized the main findings obtained from this thesis, and the plans for future work are also presented.

Chapter 2 Literature review

This chapter provides a comprehensive literature review of recent research progress in the field of indirect evaporative cooling (IEC). The review is categorized into three main parts to provide a comprehensive understanding of the current state of the existing researches.

The first section concentrates on representative numerical and experimental studies that present the modeling progress and performance enhancement of IECs with different configurations. These studies encompass various types of IEC, such as counter-flow IECs, cross-flow IECs, novel IEC structures, and hybrid IEC systems. The second part provides an overview of the basic materials used for constructing the heat exchanger. The modifications of materials to improve the performance of IEC are presented as well. The third part of the review focuses on the importance of achieving good spraying ability in real-world situations. This section emphasizes the critical role of the affiliated spraying system in ensuring the effective operation of IEC systems. By exhibiting these categories, this chapter identifies the research gaps in the IEC field and sets the foundation for the proposed novel cross-flow plate-type indirect evaporative cooler with porous material integrated into the secondary air channel surface (PIEC) in this thesis.

This chapter is written based on a published paper of this thesis author. The paper is titled "*Research development of indirect evaporative cooling technology: An updated review*" in *Renewable and Sustainable Energy Reviews*.

2.1 Numerical and experimental studies of the existing IEC

2.1.1 Counter-flow IEC

The counter-flow IEC is one of the most studied configurations in the published research.

As shown in Fig. 2.1.1, the primary air and secondary air flow in opposite directions in a counter-flow IEC. However, with the increasing demand for cooling, the traditional counter-flow IEC requires updates. It is known that the cooling temperature of the primary air is limited by the wet-bulb temperature of the inlet secondary air. To achieve enhanced cooling performance, two approaches have been proposed to extract cooled air from the adjacent channel as secondary air, thereby obtaining a lower wet-bulb temperature (Fig. 2.1.1(b)-(c)), which are named Maisotsenko cycle (M-cycle) IEC and regenerative IEC (RIEC) [8, 22, 23]. In recent years, fruitful research output has been achieved on the three forms of counter-flow IEC.

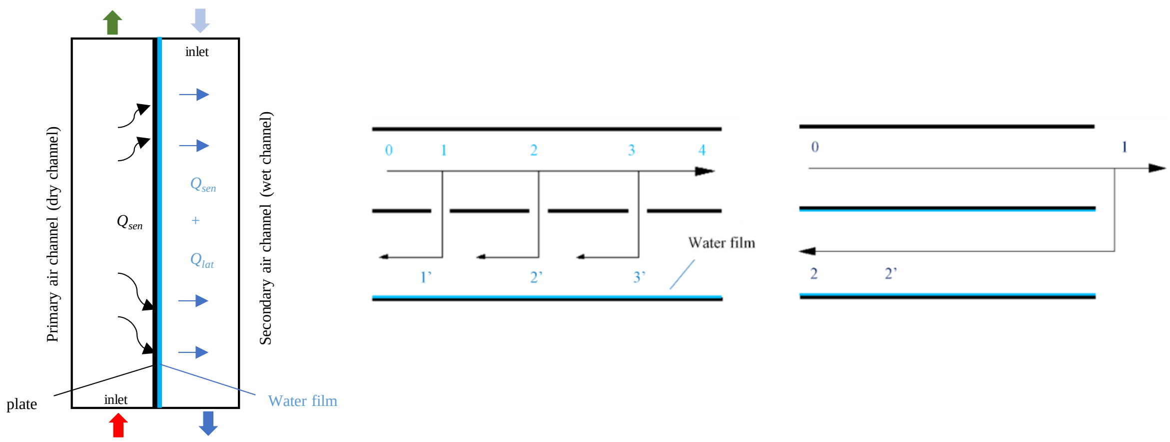

(a) (b) (c)

Fig. 2.1.1 Diagram of the counter-flow IEC

Riangvilaikul and Kumar developed a model for dew-point IEC that extracted a portion of primary air into the secondary air channel and investigated the effects of geometric factors and the working-to-intake air ratio, mainly considering the variation in the vertical direction [24]. Pandelidis et al. proposed a counter-flow IEC model based on the ε-NTU method and compared the IEC with conventional heat recovery equipment in temperate climate regions [25]. Lin et al. established a simulation model of counter-flow IEC considering the longitudinal heat conduction and the temperature gradient between the water membrane and channel sheet [26].

Chen et al. analyzed the effect of condensation in a simplified counter-flow IEC model and incorporated the model with TRNSYS to predict cooling capacity for its application in a wet market [27]. This study highlighted the importance of considering the condensation effect and showed that the simplified model can provide reasonable predictions of the cooling capacity of the system. Cui et al. discussed the precooling potential of the counter-flow IEC in tropical weather conditions using a two-dimensional (2-D) Computational Fluid Dynamics (CFD) approach [28]. Zhu et al. developed a three-dimensional (3-D) CFD model of counter-flow IEC that considered the temperature and humidity gradient in the channel gap direction (Fig. 2.1.2). The discrepancies between experimental tests and the present 3-D model were less than 3.77%, and the 3-D model increased the simulation accuracy by 5.46% compared to the traditional 2-D model [29]. Lin et al. established a transient dew point indirect evaporative cooler (DPIEC) model with validation from experiments, which studied the transient and step responses of the system. They reported that the settling time of the system was high sensitive to the inlet air status, ranging from 50 seconds to 300 seconds under their setting conditions [30]. Li et al. established three IEC numerical models with diverse airflow arrangements, and the exhaust air was recovered as the secondary air. They reported that irreversible primary air heat transfer and secondary air mass transfer accounted for more than 90% of the exergy loss [31]. Castillo-González et al. fabricated a novel IEC sheet by combining the polyvinyl alcohol with felt and polylactic acid with bronze. The former was expected to enhance the water absorption ability, and the latter improved the droplet drainage. The dew point efficiency and *COP* of this IEC system reached up to 0.9 and 22.7 in the experimental cases [32]. Kabeel et al. added baffles into the counter-flow IEC to promote heat transfer because they generated small internal vortex in the primary air channel, as presented in Fig. 2.1.3. Experimental results demonstrated that the wet-bulb effectiveness of the IEC with baffles was at least 33.3% higher than that of the one only with smooth surfaces. The primary air temperature drop also increased with the growing number of internal baffles [33].

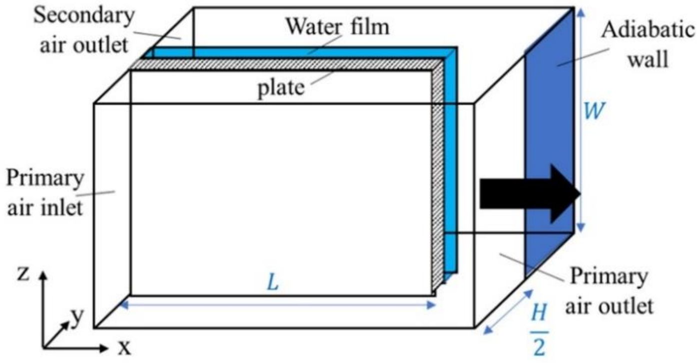

Fig. 2.1.2 The 3-D counter-flow IEC model

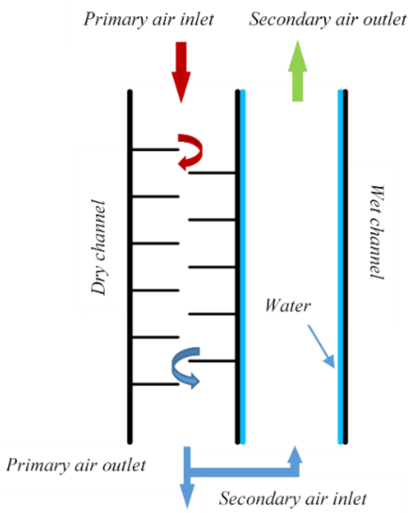

Fig. 2.1.3 IEC with innovative internal baffles in the primary air channel (the number of baffles: 11)

Furthermore, the various IEC researches have produced a large amount of fruitful data, which have been used to establish non-physical models for quick performance prediction. These valuable data have been used to establish non-physical models for quick performance prediction. Zhu et al. constructed a counter-flow IEC data-driven model based on an artificial neural network (ANN) approach. The performance of the IEC can be investigated and optimized effectively under different operating conditions. Results show that the optimal extraction air proportion, ranging from 0.3 to 0.36, reduced with the inlet air temperature and relative humidity [34]. Pakari and Ghani developed a regression model for a counter-flow DPIEC. The outlet air state was formulated by inlet operational parameters and geometric sizes. The obtained correlation equations for outlet air matched the numerical and experimental data with only 4% and 10% discrepancy, respectively [35]. According to Wan et al., correlations of heat and mass transfer coefficients and outlet temperature were developed for a counter-flow IEC [36]. The gap distance of channels was found to be most influential to the convective heat transfer coefficients of primary air and secondary air and the mass transfer coefficient in the wet channel. Re_p had the most significant impact on the primary outlet dimensionless temperature $\theta_{p,o}$ compared to other four indices.

In addition to being employed individually as a single cooling equipment, the counter-flow IEC has been combined with other AC devices as an integrated system to contribute the great cooling performance and energy saving. Nemati et al. proposed integrating the underground air tunnel with IEC [37]. In this system, the ambient air was extracted into the secondary channel and the earth-air heat exchanger. For the supply airstream, the surrounding soil absorbs heat from the buried pipes that carried the fresh outdoor air, and IEC is responsible for the further sensible cooling. This coupled system was proved not only to maintain desired indoor thermal comfort but also saved 62% and 45% energy and water consumption, respectively. Chen et al. developed a hybrid system that integrates a liquid desiccant dehumidifier (LDD) and a counter-flow regenerative indirect evaporative cooler (RIEC) [38]. This system expands the application region of the IEC from hot and arid areas to hot and humid climate conditions. The moist outdoor air is dehumidified by the strong solution film of lithium chloride (LiCl) desiccant, which is an isoenthalpy process. After passing through the LDD, the hot-dry air is delivered to the RIEC for sensible cooling. Wan et al. combined the counter-flow IEC with synthesized phase change material (PCM) to make full use of the IEC to achieve the high cooling efficiency and the latent heat thermal energy storage to shift the peak load simultaneously [39]. In this hybrid system, the temperature of the supplied chilled water can be raised, saving the energy consumed by the chiller.

2.1.2 Cross-flow IEC

The cross-flow IEC, as shown in Fig. 2.1.4, involves the primary air and secondary air flowing in separate channels, with the primary air flowing in the horizontal direction from left to right side and the secondary air flowing in the vertical from bottom to top side. Water is sprayed from the top side to the secondary air channel surface for generating the liquid membrane for evaporation. The cross-flow structure is more prevalent in practice compared with the counter-flow IEC due to its easier airflow arrangement and installation, and has been studied extensively.

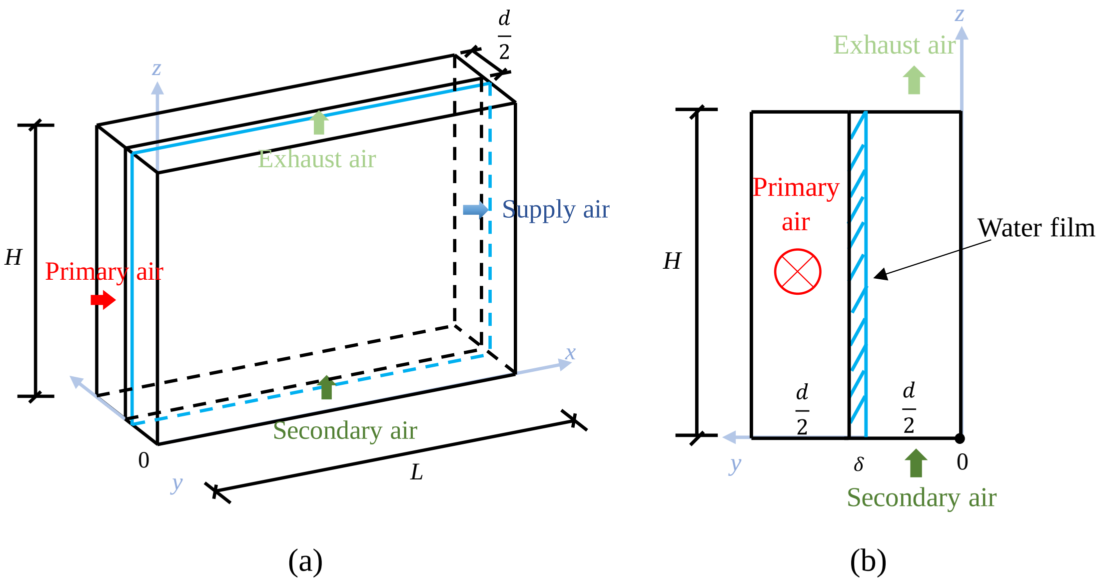

Fig. 2.1.4 Diagram of the cross-flow IEC (a) 3-D structure (b) Left side view of two adjacent half channels

An early study by Guo and Zhao numerically investigated the thermal performance of a cross-flow IEC, which preliminarily revealed the effect of various parameters such as velocities, channel height, and inlet air properties [40]. Zhan et al. established a mathematical model for a cross-flow Maisotsenko cycle (M-cycle) cooler and reported the impacts of inlet air properties and geometric parameters on the outlet supply air temperature. Results showed that the cooling effectiveness of this new type was 16.7% greater than the traditional IEC [41]. Pandelidis et al. also conducted numerical analysis on the M-cycle cross-flow IEC unit and obtained a similar conclusion that the improved cooling effectiveness was achieved by the M-cycle cross-flow IEC [42]. Shi et al. developed a 3-D cross-flow IEC model considering the humidity variation on the channel height direction, and the prediction accuracy was 5.8% higher than it of a 2-D model on average [43]. Min et al. evaluated the condensation state when the cross-flow IEC was applied in hot and moist areas, and a theoretical model was proposed to predict the development trend of condensation [44]. Guo et al. also developed a cross-flow IEC model and analyzed the effect of essential parameters on wet-bulb efficiency, condensation area ratio, dehumidification ratio, and heat transfer capacity [45]. Kousar et al. conducted experiments on the counter-flow and cross-flow IECs in three operating ranges, demonstrating that the cross-flow IEC system has better exergy efficiency and less CO_2 emission [46]. Zhang et al. analyzed the energy, exergy, economic, and environmental (4E) performance of a novel cross-flow IEC diffused with liquid desiccant in the supply air side (IECL). Results showed that IECL had better energy and exergy (2E) efficiencies than normal IEC because more water content can be removed from the air. The favorable profitability and environmental benefits of the IELC were also mentioned [47]. Furthermore, the innovative corrugated structure was imbedded into IEC to improve cooling efficiency. As depicted in Fig. 2.1.5, the embedded corrugated wick could noticeably increase the heat transfer area. They were made from cotton or paper so as to absorb more spraying water for evaporation in the secondary air channel [48]. Zhou et al. investigated the performance of two novel internal wicks, namely, the sinusoidal corrugated wick, and triangular corrugated wick in IECs, which were compared to the flat plate-type IEC using CFD simulations, which determined the first shape with optimal inclination angle of 45°[49].

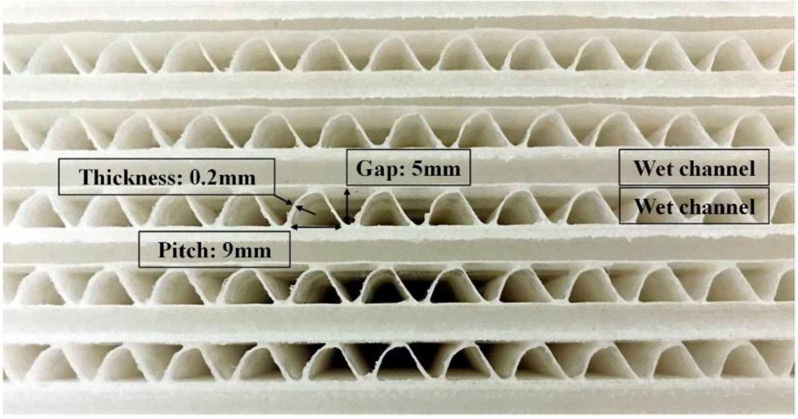

Fig. 2.1.5 IEC with the corrugated wicks in the wet channel

Regarding the non-physical cross-flow IEC model developed based on the fruitful data from numerical models and experiments, Kiran and Rajput developed the IEC effectiveness model using artificial neural networks (ANN), adaptive neuro-fuzzy inference system (ANFIS), and fuzzy inference system (FIS), and the ANN model achieved the best prediction among the three approaches [50]. Shi et al. proposed a data-driven IEC model based on ANN, but this model required a large amount of data to ensure the acceptable accuracy in the early stage, and the number of hidden layers can greatly influence the modeling establishment speed [51]. Min et al. proposed an empirical model to swiftly predict the cooling performance for the IEC with energy recovery, the empirical equations of wet-bulb efficiency and dehumidification rate (under condensation state) were accordingly given [52]. However, whether the condensation would happen needs to be judged by the decision tree before using the equations, which also cause extra calculation load.

The cross-flow IEC, in addition to its use as a standalone cooling equipment, has been combined with other air conditioning devices in various engineering projects to enhance cooling performance and achieve energy savings. Delfani et al. developed a model for IEC/PUA system and validated it through experiments. IEC would reduce 70% of the cooling load against 55% of the electricity saved for PUA [53]. Chen et al. simulated the IEC/AHU system under the climate in Hong Kong. The condensate produced by AHU was suggested to be collected and reused as the spraying water for IEC. The annual energy-saving of the IEC pre-cooling section was estimated to be 45% higher than the enthalpy-recovery rotating wheel system [14]. Min et al. carried out on-site measurements of IEC/AHU in a wet market and monitored the monthly cumulative cooling capacity for a whole year. The applicability in eight cities was discussed and predicted [54]. Cui et al. compared the performance of the IEC/AHU system in five selected regions with diverse weather characteristics, indicating that at least 35% of energy could be cut down owing to the installation of the IEC pre-cooling unit [55]. They also supplemented the research to explore the energy-saving potential of the IEC/VCRS system, which revealed that 47% of the cooling load was fulfilled by IEC at the cost of a little additional amount of fan power [28].

2.1.3 IEC in other configurations

2.1.3.1 Counter-cross flow IEC

The counter-cross-flow IEC usually consists of many thin plates in a hexagonal shape [18, 56]. Fig. 2.1.6(a) shows a counter-cross cooler with a regular hexagon heat transfer surface. The primary air and secondary air flow orthogonally at the entrance and the end of the channels but switch into a counter-flow pattern in the middle section. Fig. 2.1.6(b) is the real object made of aluminum foil. Theoretically, this counter-flow heat transfer area theoretically accounts for 58.6% while the remaining 41.4% area is in cross-flow heat exchange. Experiments were set up to test the cooling effect of this cooler under diverse operating conditions. The produced air temperature increased from 23.9 to 26.2℃ with the inlet air temperature raising from 29.5℃ to 35.5℃. The dew point effectiveness varied from 58.1% to 71.1%, and the highest COP could reach 13.8. Hence, this proposed cooler was qualified as a pre-cooling device for the residential AC system.

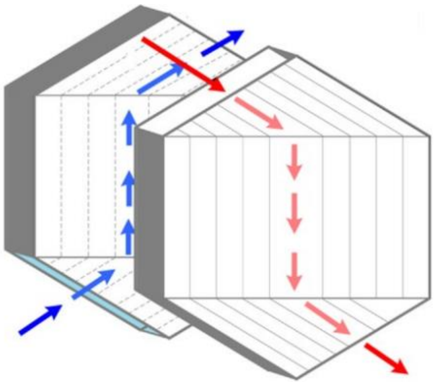

(a) (b)

Fig. 2.1.6 (a) 3-D diagram of the counter-cross-flow IEC (b) Real prototype of counter-cross-flow IEC

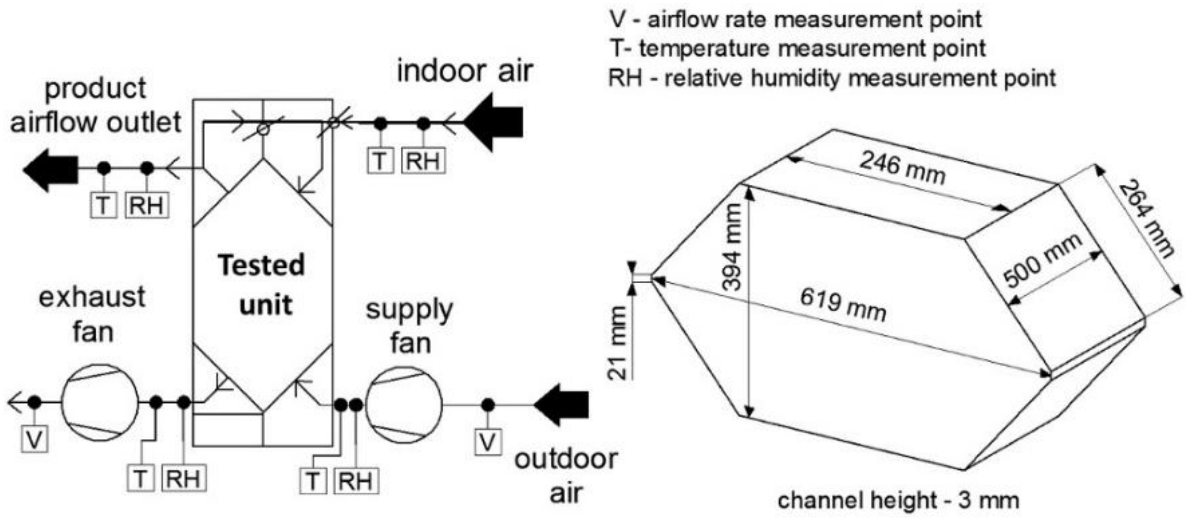

Fig. 2.1.7 Schematic diagrams of the hexagon DPIEC system [59]

Pandelidis et al. evaluated the application potential of the hexagon DPIEC system by employing the black-box model based on regression equations. The data for the black-box model originated from the test rig shown in Fig. 2.1.7. Results demonstrated that DPIEC could cover 95% of the total cooling load with only 65% of seasonal electricity, which was much more efficient than the energy recovery wheel in a hybrid system [57]. Pacak et al. further established a 3-D CFD model for this heat exchanger and estimated the system *COP* [58].

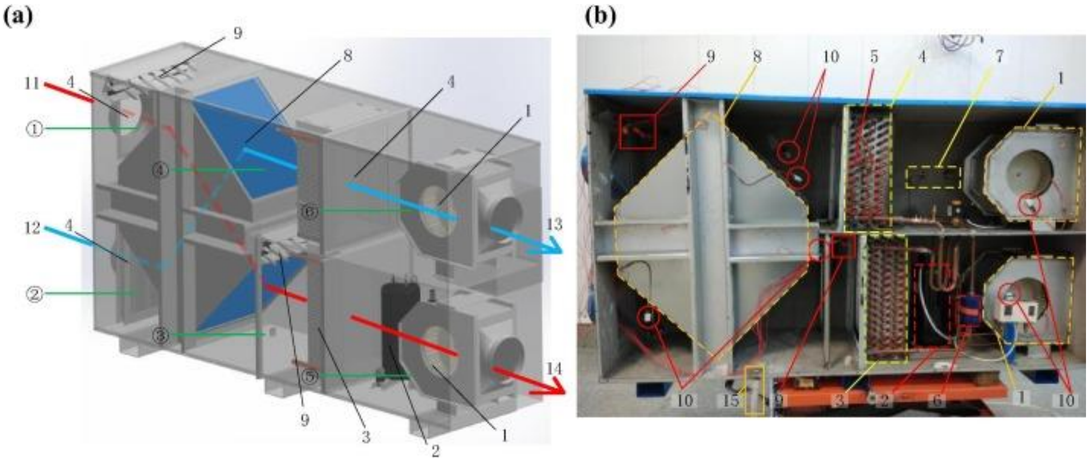

Fig. 2.1.8 Structure of hexagon DPIEC with heat pump unit (a) schematic diagram (b) inside view of the actual prototype

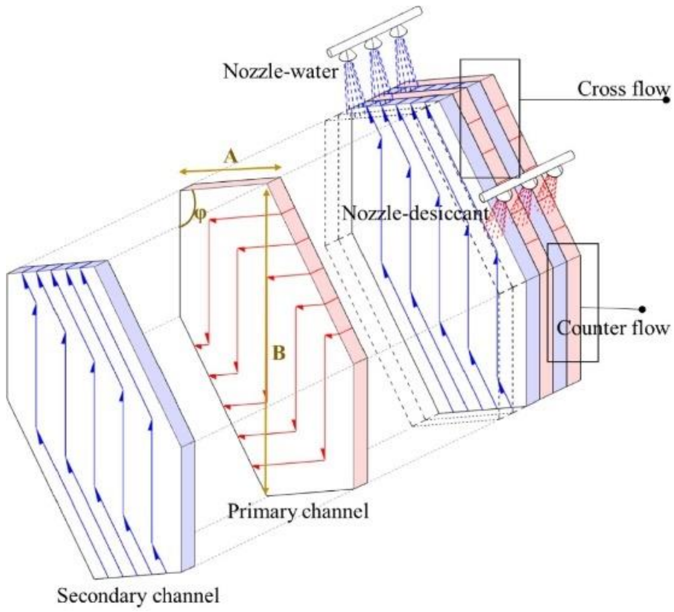

Fig. 2.1.9 Geometric model of the hexagonal PHE

Li et al. experimentally studied the coupled IEC/heat pump package with multiple modes [59]. As observed in Fig. 2.1.8, two sets of water spraying systems can operate individually with the variable climatic conditions. Four operation modes are available based on the on/off status of two water systems: Mode 1 (IEC + ECHP): Two water loops are running. In this scenario, the package can be regarded as an IEC followed by an ECHP. Mode 2 (IEC + HP): Only the water loop of the exhaust air channels of the heat exchanger is operating. The package unit consists of an IEC with a regular heat pump module. Mode 3 (SHE + ECHP): Only the condenser of the heat pump is under water spraying. The package operates as an air-to-air sensible heat exchanger enhanced by an evaporative condenser heat pump. Mode 4 (SHE + HP): Two water spraying systems are out of service. In such a case, the prototype could be regarded as the combination of an air-to-air sensible heat exchanger and a regular heat pump.

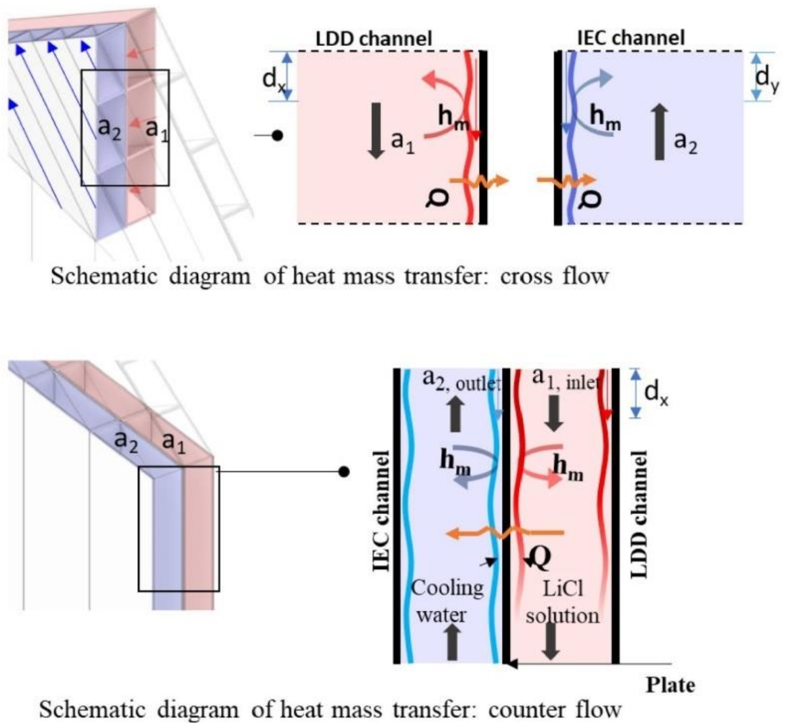

Fig. 2.1.10 Schematic diagram of the heat and mass transfer process in two adjacent channels

Zhang et al. proposed a hexagonal plate-type heat exchanger (PHE) with enhanced dehumidification performance [60]. As presented in Fig. 2.1.9, the fresh air channel and working air channel are sprayed with lithium chloride and water, respectively. The indirect evaporative cooling in this heat exchanger can not only precool the fresh air but also play a role in internal cooling during the dehumidification process. The dehumidification efficiency of a heat exchanger is primarily affected by its various design parameters. Among all the design parameters, the channel height is the most influential parameter on the dehumidification efficiency. It was suggested that the optimal channel height should be 0.004 m to achieve the desired dehumidification efficiency. Additionally, the operating parameters of the heat exchanger also play a crucial role in determining its dehumidification efficiency. Among the studied parameters, the air speed has the most significant impact on the dehumidification performance.

2.1.3.2 Tubular IEC

An early experimental study by Tulsidasani et al. assessed the impact of air velocities on COP for a tube-type IEC. The outlet temperature, static pressure, and energy consumption were examined [61]. Recently, a prototype of the ceramics tubular IEC was manufactured by Wang (Fig. 2.1.11) [62]. For this cooler, water is sprayed on the outer surface of the ceramic pipe to generate a water membrane. The fresh primary air flows inside the pipes horizontally, while the secondary air sweeps across the pipes from the vertical direction, accelerating the evaporation of the water film covering the outer surface of the pipe. It was observed from experiments that the tubular structure could provide more uniform water film distribution on the outer surface. The theoretical research was conducted to predict the thermal performance of the porous tubular IEC as well, which was validated by the data from experiments [63]. Additionally, Sun et al. optimized the wet-bulb efficiency of a tubular IEC based on a statistical approach named response surface methodology (RSM) considering the effects of six parameters: inlet air temperature, relative humidity, spray water flow rate, secondary-to-primary air ratio, primary air resistance, and secondary air resistance. In summary, this novel tubular IEC was expected to achieve a lower supply air temperature and promote efficient cooling [64].

The latest research from Gao et al. proposed an advanced tubular IEC. As shown in Fig. 2.1.12, water is sprayed from the small holes to the outer surface of the primary air pipe to generate the liquid membrane with the aid of gravity. The heat and mass transfer coefficients are 2.7 times enhanced compared with the normal plate-type cooler and reach 150 $W/(m^2 \cdot K)$

and 0.04 m/s, respectively [65]. However, the large volume of the device, to some extent, constrained its extensive application.

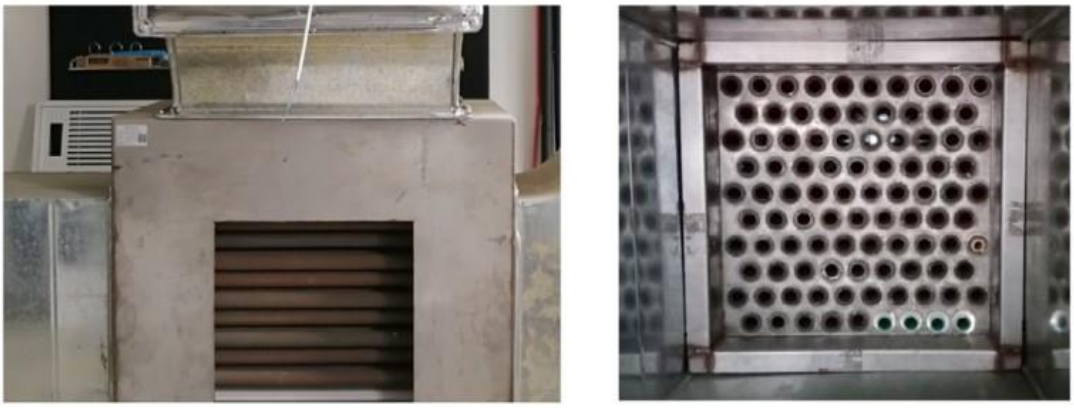

Fig. 2.1.11 A prototype of the tubular porous cooler

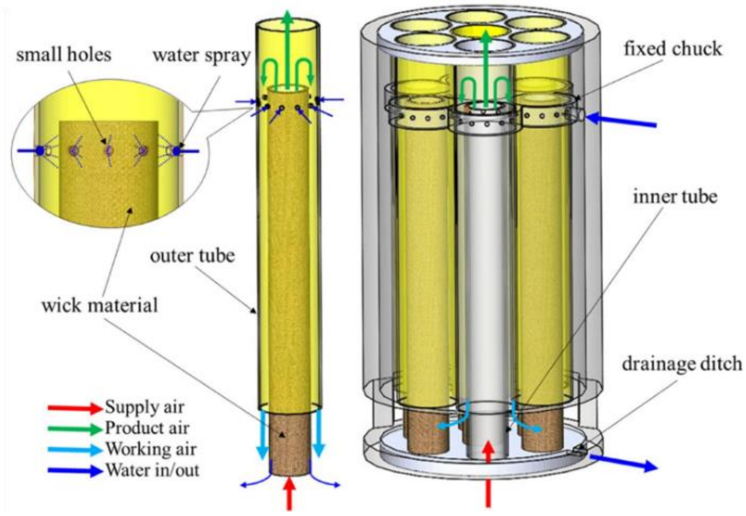

Fig. 2.1.12 Advanced tubular IEC [65]

2.1.3.3 Heat-pipe based IEC

Heat-pipe-based IEC has also attracted attention in the past few decades [66-68]. The heat pipe, with considerable thermal conductivity, has been incorporated into IEC for performance enhancement. Fig. 2.1.13 shows a gravity-assisted, heat-pipe-based IEC with staggered pipes. The section of the heat pipe in the dry channel serves as an evaporator to absorb heat from the primary air. The other side is equivalent to a condenser, attaching the spraying water to the outer surfaces to generate water films and remove heat through evaporation. After the fluid medium in the tube absorbs heat and evaporates into a gas state, the gas flows into the condenser due to the saturation pressure difference between the evaporator and condenser. Then, it recovers to the liquid state by releasing heat in the condenser and flows back to the evaporator because of gravity and capillary action for subsequent circulation. During this process, the heat is taken away by the evaporated water.

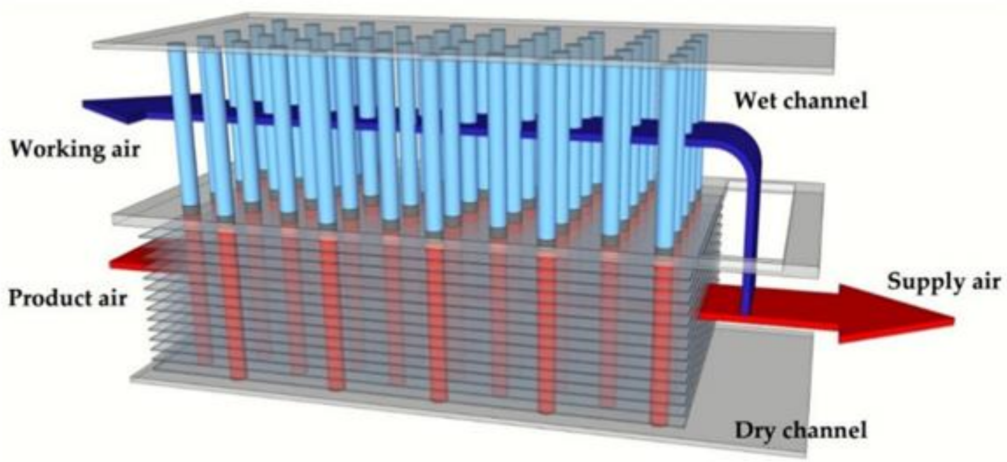

Fig. 2.1.13 Schematic diagram of heat-pipe based IEC

2.1.3.4 Rotary IEC

The Rotary Indirect Evaporative Cooler was recently proposed by Pandelidis, which functions by wetting the cooler portion that interacts with the secondary airstream in the working section [69]. As shown in Fig. 2.1.14, water is applied solely at the entrance to the working section of the heat exchanger, in relation to the rotary direction. The wetted filling in the working section evaporates upon contact with the entering secondary air (2i in Fig. 2.1.14), leading to a decrease in the temperature of the constituent plates. (2i in Fig. 2.1.14). As water is only sprayed at the beginning of the working section, the thickness of the water film covering the plates reduces as it evaporates while the filling moves through the working section. The dried and cooled filling moves into the product part following the rotary direction. The product airflow (which enters the product section at 1i and exits at 1o in Fig. 2.1.14) flows counter to the working airflow and cools without altering its humidity ratio by passing over the dry and cool filling in the product section.

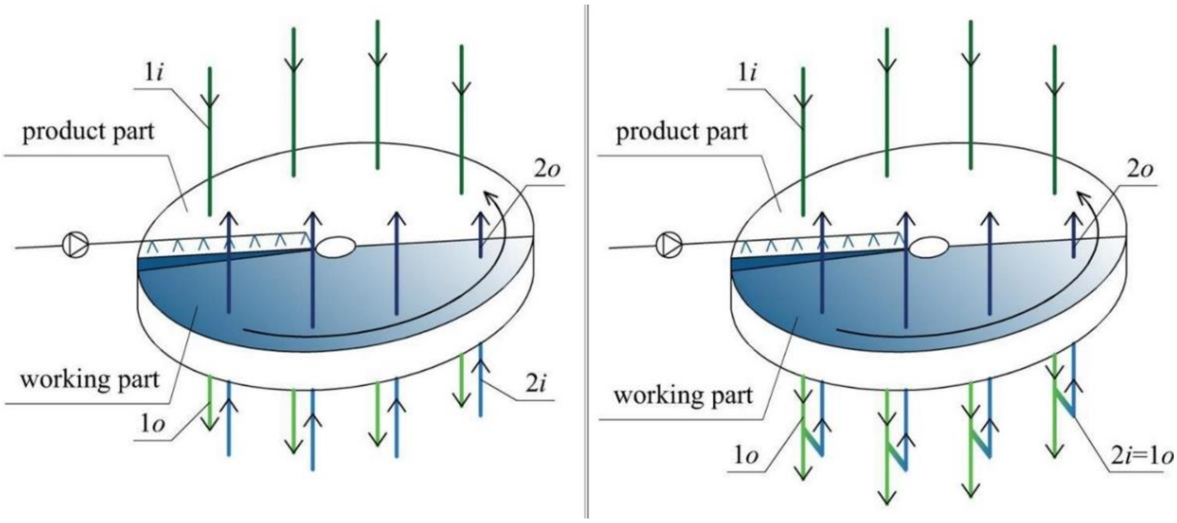

(a) (b)

Fig. 2.1.14 Schematic diagram of the rotary IEC

2.2 Material of the IECs

When selecting the material for manufacturing the IEC, good thermal conductivity, corrosion resistance, and durability are usually considered. In addition, poor water retention ability and low wettability have been realized as the barrier to reliable evaporation from the wet channel surface. As known from the IEC working principle, the heat is mainly taken away by evaporative latent heat. Suitable materials significantly strengthen the performance because they can keep water film evenly distributed for continuous and stable evaporation [70]. Generally, efforts made by the previous research can be assorted into two aspects. On the one hand, the heat transfer area can be enlarged to contact more spraying water. On the other hand, the hydrophilic coatings can be deposited on the secondary air channel surfaces, and the water membrane can be formed homogeneously. This section summarizes several materials adopted in recent studies.

2.2.1 Metal

If the material is unable to disperse water droplets into thin film on the surface, the evaporation rate may fluctuate largely. Thus, the material for IEC was expected to have both good thermal conductivity and surface wettability [71]. Many IEC plates were made of metal such as aluminum, copper, and their alloy. The summary of employed materials in existing studies is presented in Table 2.2.1. It can be noted that aluminum is dominant and widely applied due to its good thermal conductivity and hydrophilicity. Moreover, the slight thickness of aluminum plates can be neglected, and they can be considered to have the same temperature as the water film [72].

Table 2.2.1 Metal materials used in IEC studies

Research	Material	Type	Thickness(mm)
[73]	Aluminum	Cross-flow plate	0.14
[74]	Aluminum	Plate	0.25
[75]	Aluminum	Plate	0.14
[76]	Aluminum	Plate	0.5
[77]	Aluminum	Plate	3
[78]	Aluminum	Plate	0.4
[56]	Aluminum	Plate	0.1
[79]	Stainless steel	Plate	1.5

[80]	Aluminum	Plate	0.15
[81]	Aluminum alloy	Plate	0.15
[82]	Copper	Tube	10

2.2.2 Porous media

With the progress of manufacturing techniques and awareness of the heat transfer enhancement, porous media have been employed to enhance the heat exchange process since their many holes can bring a much larger contact area and disturb the boundary layer and flow status [83-85]. Porous ceramics are widely utilized due to their high porosity, good thermal conductivity, and corrosion-resistant ability [86]. High porosity brings larger specific surface areas as well as water storage capacity. The good water storage ability makes it possible for the spraying system to operate intermittently, reducing the energy consumption of pumps and the usage of water resources.

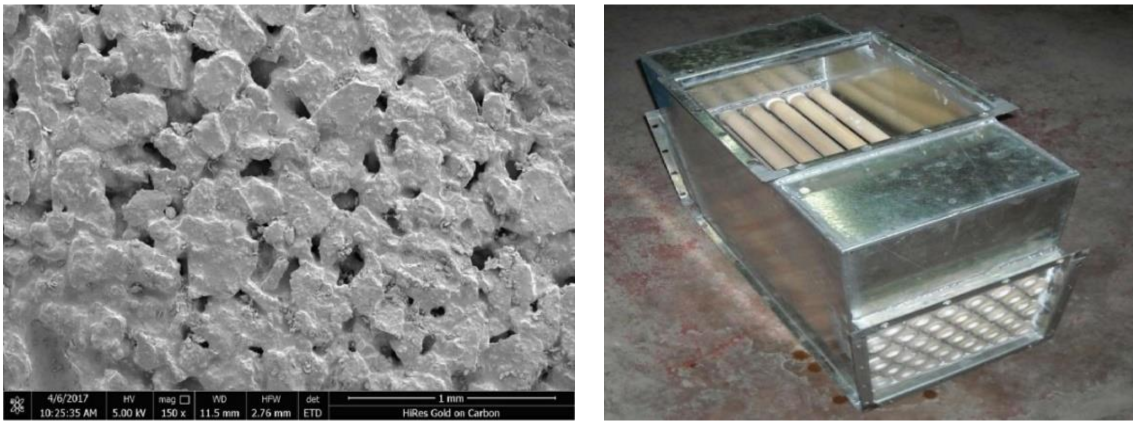

(a) (b)

Fig. 2.2.1 (a) Porous ceramic under the scanning electron microscope (b) Tubular porous ceramic IEC

Regarding the application of porous media in the IEC studies, Wang et al. conducted an experimental study on a tubular porous ceramic IEC (Fig. 2.2.1)[62]. A non-permeable membrane was coated on the surface towards the primary air to avoid water penetration. This ceramic IEC was compared with an aluminum IEC covered with textiles on the outer tube surface. Results demonstrated that the porous ceramic IEC could maintain the produced cooling capacity consistently for 100 minutes after 5 minutes of thoroughly wetting by spraying water. Therefore, an intermittent spray strategy could be achieved, and the energy cost of the water pump could be considerably saved. Sun et al. supplemented theoretical research on this porous tubular IEC by establishing a CFD model for it, and the length of the IEC and spacing distance among tubes are optimized [63].

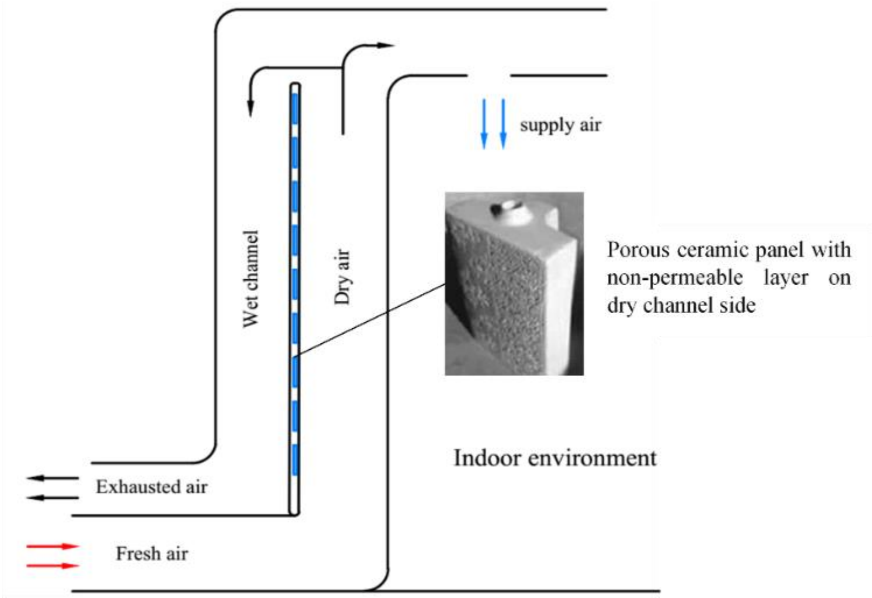

Fig. 2.2.2 Schematic diagram of a building integrated porous ceramic RIEC

2.2.3 Surface treatment

In addition to exploring the reliable material, the surface treatment also attracts research attention. The IEC channel surface can be treated to improve the cooling performance. The purposes of surface treatment in the primary air channel and secondary air channel are different. Good wettability and water retention ability are required in the wet channel surfaces for sufficient evaporation, while the condensed water is unexpected to stay on the surfaces of the primary air channel as the additional thermal resistance.

As known from the existing literature, an evenly distributed thin water film is usually assumed with a constant thickness in the wet channel surface. However, sometimes large water droplets cannot disperse into a thin water film due to surface tension and poor hydrophilicity of the surface material in the real situation. In order to improve the surface wettability, the plate surface towards the secondary air side can be further treated. Generally, two methods are now technically available in the industry and welcomed by researchers. One is to attach materials with strong water-absorbing characteristics, such as fiber and cotton. The other is to cover the hydrophilic chemical coating.

The heat and mass transfer on surfaces covered with fiber has captured interest in the past few decades [48, 76]. As for the IEC application, some fabrics (textiles) weaved from different fibers were attempted for their moisture-absorbing ability. Test results have revealed that the evaporation and diffusion abilities of fabrics on the wet channel surface were 77% to 93% and 298% to 396% higher than those of a smooth surface, respectively [71]. Although most of the fiber materials cannot be directly made as plates for coolers owing to their weak mechanical properties compared with metal and ceramic, they can be fabricated on the base plate surface to increase the heat and mass transfer area and absorb more water. Fiber materials are commonly available in daily life, and the price is affordable. Table 2.2.2 shows some combinations of the base plates and attached fiber materials in experimental studies. Duan et al. not only tested several sets of combinations, but also provided the bonding treatment ways, specifically hot-melt and adhesive methods [89]. The IEC attached absorbent materials on the secondary channel surfaces was proved to be more effective for evaporation. However, some drawbacks exist and become barriers to the broader application of fiber materials. Firstly, the wetted fiber surface is easy to introduce and breed bacterium and pollute the air and channels, making more troubles for hygiene treatment. Secondly, the life span of the existing water-absorbent fiber material is not long enough so that frequent replacement of the wick is needed, consequently increasing the maintenance requirement [16].

Table 2.2.2 Configuration of the base plate and covered material in experiments

Research	Base plate material	Coated material
[90]	Polystyrene	Nylon fiber
[89]	Wax	Kraft paper
[41]	Polyethylene	Fiber sheet
[24, 91]	polyurethane	Cotton sheet
[92]	Aluminum	Porous fiber
[76]	Aluminum	Felt
[93]	Aluminum	fabric
[33]	Aluminum	cotton

Surface coating technology has been employed to promote the formation of a water film without the risk of breeding bacteria. Lee et al. investigated the effect of porous coating on the aluminum surface of a RIEC [74]. Guilizzoni et al. studied two different coatings for IEC, namely, standard epoxy coating (STD) and hydrophilic lacquer (HPHI) [81]. An experimental study was conducted to test their contact angle and water retention ability of them. Photographs revealed that the HPHI led to a lower contact angle than STD, and consequently made a significant growth of the hydrophilicity in the wet channel, corresponding to 10% cooling performance improvement. Kashyap discussed the effects of four surface modifications on a regenerative IEC (RIEC), namely, flat surface, capsule embossing surface, finned surface, and corrugated surface [94]. Min et al. immersed the primary air channel using $(R_2SiO)_x$ aqueous solution to improve the hydrophobicity of the surface. The dehumidification is difficult to develop as condensation film so that can be drained in the form of water droplets. The energy saving rate through the hydrophobic coating was enhanced within the range of 8.5% to 17.2% [95]. The impact of using ternary composite nanofluids on the RIEC was also analyzed [96]. Tariq et al. examined four different evaporation mediums, namely water, CuO nanofluid, TiO_2 nanofluid, and Al_2O_3 nanofluid, in a M-cycle cross-flow IEC system. They suggested that the optimal medium for this system was the Al_2O_3–water nanofluid, with a recommended particle volume concentration of 1% and a particle size diameter of 20 nm [97]. Chen et al. investigated the influence of hydrophilic nano-cooling of TiO_2/SiO_2 on the secondary air channel surface for better wettability. Results showed that the nano-coating has a tiny effect on the thermal conductivity but significantly enhances the water diffusion [98].

Condensation occurs in the primary air channel surface when hot-humid outdoor air is used as the secondary air from the air-conditioned indoor space. Literature has illustrated that filmwise condensation (FWC) is more likely to be generated on hydrophilic surfaces, which leads to additional thermal resistance compared to hydrophobic surfaces [99, 100]. It has been reported that condensation on the surface tends to change from dropwise condensation (DWC) to FWC in the evolution process, generating the water film on the primary air channel and causing additional thermal resistance. This led to a 14.8% deterioration in the wet-bulb effectiveness of IEC [101]. Therefore, it is recommended to use a hydrophobic treatment on the primary passage surface, which can increase the contact angle between water droplets and the surface, thereby improving the droplet drainage ability. By improving droplet drainage, the hydrophobic treatment can reduce the likelihood of FWC occurring on the surface, leading to improved cooling performance. [44].

2.2.4 Other materials

In addition to different kinds of metal, metal alloy, porous ceramic, and fiber sheets, a variety of organic materials such as polystyrene [90], polycarbonate[102], polyurethane [24], polyethylene phthalate [103, 104], polyvinyl chloride (PVC) [105], cotton sheet [91], clay [106], and polyethylene terephthalate (PET)/cellulose [107] are also adopted to make the plate type or tubular type IECs. Although their thermal conductivity was lower than metal materials, their thermal resistance was small due to the thin thickness of the plate so as to satisfy the experimental requirements, which was neglected in the model development as well. However, the choice of material should be carefully considered based on its thermal properties, durability, and compatibility with the specific application.

2.3 Spraying system improvement

In the previous sections, the IEC has been reviewed from numerical and experimental studies on the traditional and novel configurations, and commonly-used materials and surface modifications, which almost focus on the heat exchanger itself. Many numerical studies assume an even and thorough water film coverage, while achieving this in experiments or engineering is challenging. In practice situations, the spraying system can significantly influence the wettability so as to determine the cooling performance of IEC [108, 109], and it should be designed carefully to minimize experimental errors by proper distribution arrangement. Therefore, the studies on the water spraying system optimization should also be reviewed as follows, which are usually concerned from the viewpoints of spraying position, spraying nozzle types, and spraying nozzle layout.

A theoretical study has been conducted by Lacour et al. using a 3-D model, which was created through CFD to calculate the temperature and humidity distribution during the process of spray water dispersion. The study discussed the spray radius, nozzle aperture, water and air velocities, and the optimal distance between the nozzle and the heat exchanger [110]. Similarly, Montazeri et al. conducted a simulation of the behavior of sprayed water in an evaporative cooling system and validated it successfully with a wind tunnel test within 10% discrepancy [111].

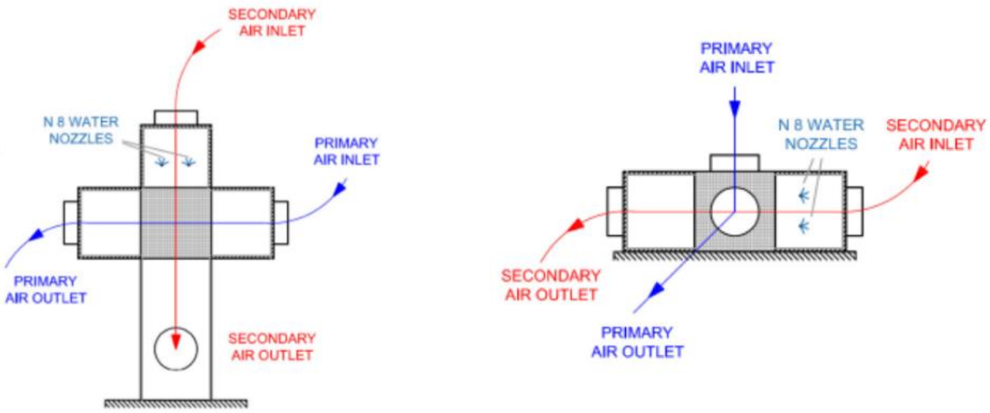

(a) (b)

Fig. 2.3.1 Spraying system configuration in (a) Top arrangement (b) Horizontal arrangement [108]

In addition to theoretical analysis, experiments were also conducted to optimize the system design. Ahmed et al. conducted several experiments under varied air velocities and temperatures, focusing on three spraying modes: external mode, internal mode, and mixed mode. The internal spraying strategy was ultimately identified as an effective approach to enhance the heat and mass exchange for the hexagonal plate cooler [105]. De Antonellis et al. analyzed the impact of water nozzle position and airflow directions on performance for a cross-flow IEC. Six configurations between the nozzles and the heat exchanger were evaluated, and top and horizontal spraying configurations were recommended for ideal water distribution, as depicted in Fig. 2.3.1 [108].

Sun et al. examined five types of spraying nozzles, namely, spiral, conical, square, sector, and target impact nozzles. They are installed on the top side of the water distribution grid (Fig. 2.3.2(c)). Both the target impact nozzle (Fig. 2.3.2(a)) and the spiral nozzle (Fig. 2.3.2(b)) had a good coverage ratio and uniformity. However, it was found that the target impact type consumed a large amount of water, which may not be suitable in regions lacking water resources. Therefore, the spiral type was finally recommended as the optimal choice [109].

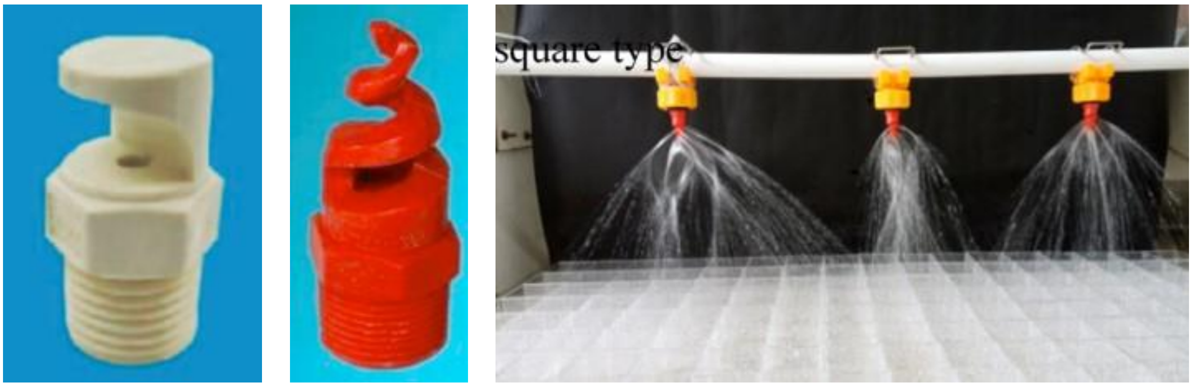

(a) (b) (c)

Fig. 2.3.2 Various types of nozzles (a) Target impact nozzle (b) Spiral nozzle (c) Spraying effect of the spiral nozzle

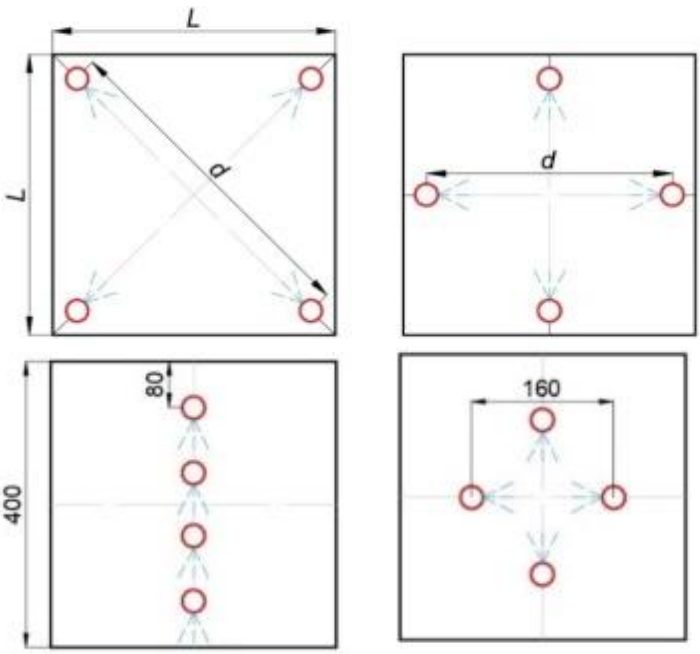

Fig. 2.3.3 Multiple spraying nozzle arrangements

Ma et al. proposed a numerical model to forecast the spray water density distribution of solid cone nozzles on the impact surface with uniformly divided square grids [112]. The actual water spray density calculated from this model can be employed for corrections of the wetting factor in the published numerical model. Fig. 2.3.3 shows multiple spraying nozzle arrangements. The optimal arrangement scheme was determined based on the uniformity coefficient and coverage ratio of the water spraying, with the nozzles placed above the heat exchanger at a distance of 160 mm on the centerline. This optimized nozzle arrangement scheme was demonstrated to greatly improve the cooling and dehumidification performance of IEC compared to the other original layouts of the nozzles.

2.4 Research gaps

The above comprehensive literature review has indicated that the IEC has been developed rapidly with the advantages of low energy consumption, low greenhouse gases emission, and absence of the harmful refrigerants. The traditional counter-flow IECs and cross-flow IECs have been comprehensively investigated in the past few decades. The theoretical studies of the normal IECs were carried out from many aspects such as various input parameters, creative shapes of the heat transfer sheet, different airflow arrangements, and innovative internal structures. The experiments of the fruitful IECs with difference configurations, materials, and optimization of the spraying directions and layouts were implemented as well. However, despite significant advancements in the field of IEC from various perspectives, several research gaps still exist, which can be summarized as follows:

1) From the perspective of the IEC type, to the best knowledge of the author, although the IEC has been developed in various configurations using different materials and embedded wicks as illustrated in section 2.1 and section 2.2, the cross-flow plate-type IEC with porous material on the secondary air channel surface (PIEC) was yet to be

proposed in the previous study. In addition, no commercial product or prototype has been manufactured and evaluated.

2) For the spraying system, as introduced in section 2.3, the published studies focus almost on the nozzle selections, design of the nozzle distributions, and spraying positions and angles, which always require consistent water spraying. In other words, the spraying strategy is unique and unalterable, and the water needs to be continuously supplied for evaporation when the IEC system is operating. The introduced porous structure can provide the space for water storage, enabling both traditional and periodic operation modes of the spraying system. However, the feasibility of switchable spraying modes and the cooling performance of PIEC under the steady and dynamic states was rarely investigated.

3) Regarding the modeling, studies on the development of 1-D and 2-D IEC models have been frequently found for cooling performance analysis and prediction. These models can show the temperature or moisture content gradients in the airflow direction, while the profiles of air temperature and humidity along the channel height direction are required to be simplified as constant. However, air properties are different at each point in the heat exchanger, which can only be comprehensively presented using a 3-D model. To date, the 3-D model of the novel PIEC was seldom established under different spraying conditions.

4) The developed 3-D model offers reliable accuracy in predicting the performance of the PIEC, which requires a high level of computing configurations and consumes significant computational resources, making it impractical for use in the real engineering applications. A more straightforward approach to forecasting the PIEC performance can facilitate the possible and convenient usage in reality. However, the

regression models of this newly proposed PIEC were lacking. The operating parameters need to be optimized in the reasonable ranges as well.

5) With the embedded porous media in the secondary air channel, the water system is anticipated to operate intermittently. Nonetheless, very little research evaluated and compared the energy, exergy, and environmental (3E) performance of the PIEC under the conventional consistent spraying and intermittent spraying conditions.

2.5 Research objectives

The research objectives can be proposed to bridge the research gaps identified in section 2.4. The research flow chart of the thesis is presented in Fig. 2.5.1 to show the process and connection among each component. The research objectives of this thesis are as follows:

1) To propose, design, and manufacture an innovative cross-flow plate-type IEC with porous material on the secondary air channel surface (PIEC).

2) To validate the feasibility of using the porous material to temporarily store the water for evaporation and maintain the cooling performance by experiments. The feasibility of the intermittent spraying mode is explored through experiments, which is the greatest distinctness between the newly proposed cross-flow PIEC and the traditional IEC. Additionally, the experiments can provide the data for the validation of the simulation model.

3) To establish a 3-D model for the PIEC and predict the cooling performance under sufficient spraying and intermittent spraying. This model is going to be verified by the data obtained from the experiments, which can forecast the distributions and variations of aimed parameters in a period of time. The influences of essential input factors on the PIEC performance can be revealed as well.

4) To develop regression models and conduct the optimization for the adjustable parameters. The obtained equations can significantly facilitate the calculation process and provide reliable predictions in common ranges of the PIEC input parameters.

5) To conduct the energy, exergy, and economic (3E) comparisons of the PIEC system between traditional consistent spraying and the novel periodic spraying. The advantages of the PIEC using the new spraying plans will be revealed from the three perspectives.

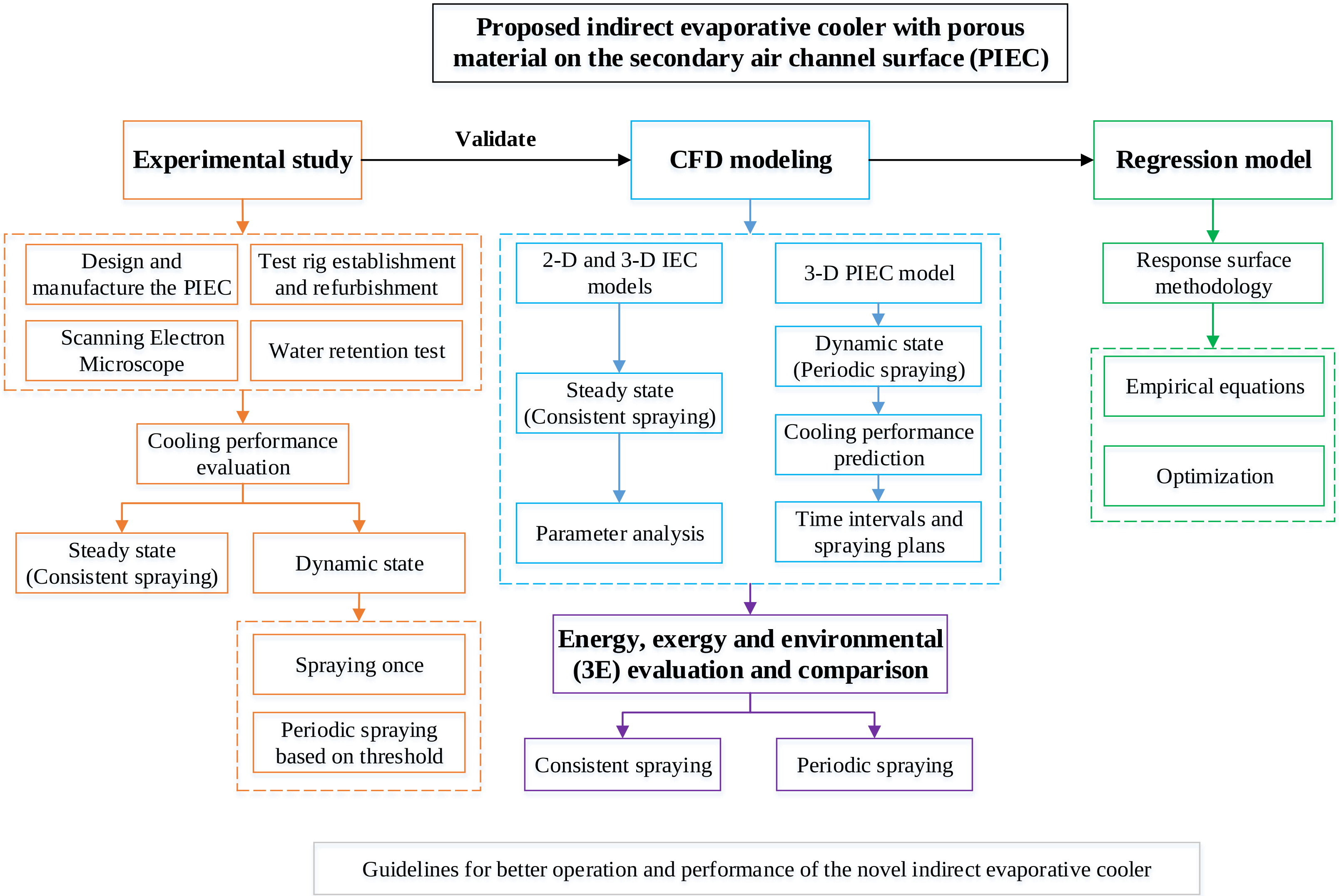

Fig. 2.5.1 Research flow chart of this thesis

Chapter 3 Experimental study on the performance of the PIEC prototype with dual spraying modes

Chapter 3 presents the experimental study on the performance of the novel indirect evaporative cooler with porous material (PIEC). The comprehensive experiments are conducted in a constructed test platform at the PolyU laboratory. This chapter is structured as follows: Firstly, the experimental system is established and described, including its configurations and the measurement devices used. Secondly, with awareness of the potential of porous media for water storage, the plate-type cross-flow PIEC is proposed. The design, manufacturing craft, water retention test, and comparison between the bare surface and porous surface of a PIEC prototype are illustrated. Then, the experimental procedures are illustrated in detail, and the factors that influence the cooling performance were investigated. Finally, the results of the experiments are analyzed.

The purposes of this experimental study can be summarized in the following perspectives. 1) Examining the water retention characteristic of the porous structure of the PIEC prototype; 2) Exploring the feasibility of using different spraying modes for cooling production; 3) Investigating the cooling performance under different spraying conditions; 4) Collecting the real data for the validation of the PIEC simulation model established in the next chapter.

This chapter is written based on a published paper of this thesis author. The paper is titled "*Performance evaluation of a novel plate-type porous indirect evaporative cooling system: An experimental study*" in *Journal of Building Engineering*.

3.1 Description of the PIEC system

3.1.1 Experimental setup

In order to evaluate the performance of this PIEC prototype, a test platform was first established in the underground laboratory of Block Z at The Hong Kong Polytechnic University. The schematic diagram of the platform is presented in Fig. 3.1.1(a), which contains a primary air loop, a secondary air loop, and a spraying water system. A fan delivered the primary air in the horizontal direction, while the secondary air, forced by another fan, passes through the PIEC in the vertical direction from the bottom to the top side, promoting evaporation and escaping from the top side. The air velocity of each fan was controlled by the control panel, ensuring stable and consistent airflow. To measure and record the performance of the PIEC, corresponding sensors were used to measure temperature, relative humidity (RH), airflow speed, and pressure drop, as shown in Table 3.1.1. The power consumption of the water pump and fans was recorded by power meters. To achieve the desired inlet air temperature, each air duct was matched with an electrical heater, which was monitored by a temperature sensor. The outer air ducts, water tank, and heat exchanger were insulated with sufficient thermal insulation.

Table 3.1.1 Specifications of measuring equipment

Parameter	Instrument	Range	Measuring accuracy
Dry-bulb temperature of air	Pt1000 Model: EE160	0-50℃	± 0.3℃
Relative humidity of air	Pt1000 Model: EE160	0-100%	± 2.5% RH
Air velocity	Hot film anemometer	0-20 m/s	± 1% FS

	Model: EE650		
Pressure drop	Air differential pressure transmitter Model: YX-FYXS-010G	0-200 Pa	0.2% FS
Power	Power meter Model: VICTOR-7800	0-20 A 0-12 kW	± 0.4% of reading
Data logger	GRAPHTEC GL800, 20 channels		

FS: Full scale

During the test period, it was important to identify steady state conditions in order to ensure accurate and reliable data collection. This was achieved by monitoring the fluctuations of outlet temperature and relative humidity (RH) and ensuring that they were within ±1% and ±5%, respectively, for at least 5 minutes, as implemented in the previous studies [44, 62]. All data were collected by the sensors, which were sent and recorded in a data logger every second. The data logger was connected to a laptop for monitoring. For the groups of steady tests, the average values of the obtained data were calculated and used for further analysis. This ensured that the data collected were representative of the steady-state conditions and reduced the impact of any transient fluctuations or noise on the analysis results. The real scene of the test rig is presented in Fig. 3.1.2.

Furthermore, as proposed in the recently published literature [12, 27, 104], using the cool exhaust air from indoor areas as the secondary air to obtain a lower product air temperature was applicable in this study. The test rig used in this study was established in a large underground area equipped with an air conditioning (AC) system, which was designed to maintain a reliable indoor thermal environment. As such, the secondary air used in the experiments was obtained from the air-conditioned space within the underground area. The temperature and relative humidity of the secondary air were measured using *T*/*RH* sensors and were found to be 23℃ and 70%, respectively, with tiny fluctuations of ±0.2℃ and ±1.5%, respectively.

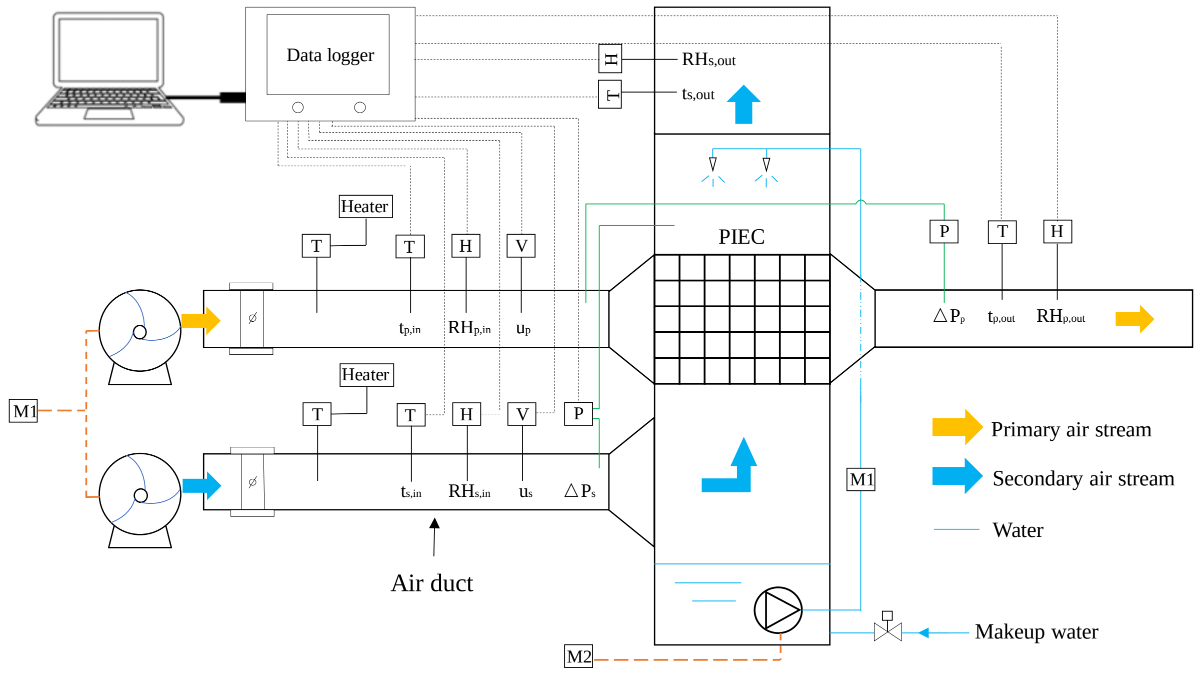

T/RH: Temperature and relative humidity transmitter (℃, %)
V: Air velocity transmitter (m/s)
M_1, M_2: Power meter (W)
P_1, P_2: Air differential pressure transmitter (Pa)

Fig. 3.1.1 Schematic diagram of the test rig

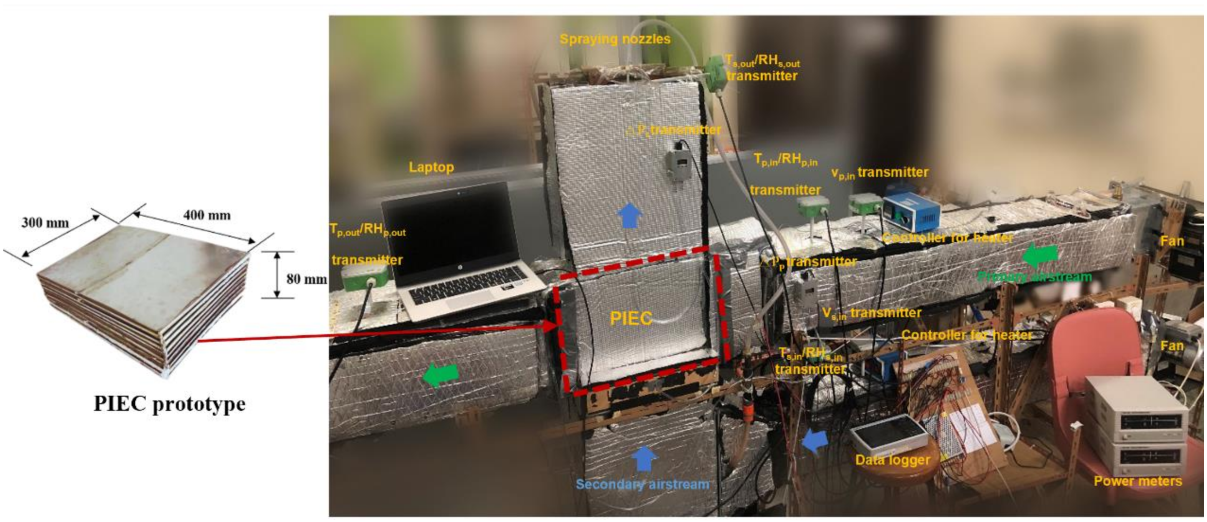

Fig. 3.1.2 Real picture of the test rig

(a) T/RH sensor

(b) Velocity sensor

(c) Pressure drop sensor

(d) Temperature controller

(e) Power meter

Fig. 3.1.3 Photo of measuring and control equipment in the test platform

3.1.2 Design and manufacturing of the PIEC prototype

Fig. 3.1.4 shows the layout of the PIEC prototype used in the experiments. In this design, fresh outdoor air enters the PIEC horizontally from the left entrance and exits on the right side, while the secondary air passes through the heat exchanger vertically from the bottom to the top. The hybrid heat transfer metal plate of the PIEC was made by sintering nickel (represented in yellow) on a smooth stainless-steel base plate (represented in gray). The use of sintered nickel in the hybrid heat transfer plate has two main advantages. Firstly, nickel is stable in common substances such as acids, alkalis, and salts, and is not easily corroded. compared to other metal materials, such as aluminum foil used in IECs [113]. Secondly, because of the sintering craft, the porous layer is more solid than other existing fabric water-absorbing materials, which is faded much slower when it suffers from the flushing water. In respect to the stainless steel, it is extensively utilized in various industries such as transportation, food, pharmaceuticals, cosmetics, chemicals, and machinery manufacturing owing to its outstanding corrosion resistance, oxidation resistance, weldability, mechanical strength, and relatively low cost [114]. Several types of stainless steel are available in the existing industry such as 304 and 316. In this thesis, the 304 stainless steel is used as the base plate. The physical properties of the two selected materials are listed in Table 3.1.2 [115, 116].

Table 3.1.2 Physical properties of materials for manufacturing the hybrid plate

Property	Unit	Material name	
		304 Stainless steel	Nickel
Density	g/cm^3	7.9	8.9
Melting point	°C	1450	1455
Thermal conductivity	W/(m·K)	16.2	88.5
Specific heat capacity	J/(kg·K)	490	452
Modulus of Elasticity	GPa	193	199.5

The main manufacture procedure of the hybrid heat transfer plate is described as follows. In the first place, the raw materials are stacked on the stainless-steel plate, which are put together into the furnace for sintering. Sintering is a manufacturing process that involves applying heat and/or pressure to a material to form a solid mass without melting it to a liquid state. This process results in the compaction and formation of the material into a dense, solid structure. Then, the plate is sintered in the protective atmosphere of high-purity hydrogen (purity ≥ 99.999%) at a temperature of 1250°C for a duration of 2 hours. Finally, the composite plate can be taken out after the furnace is cooled.

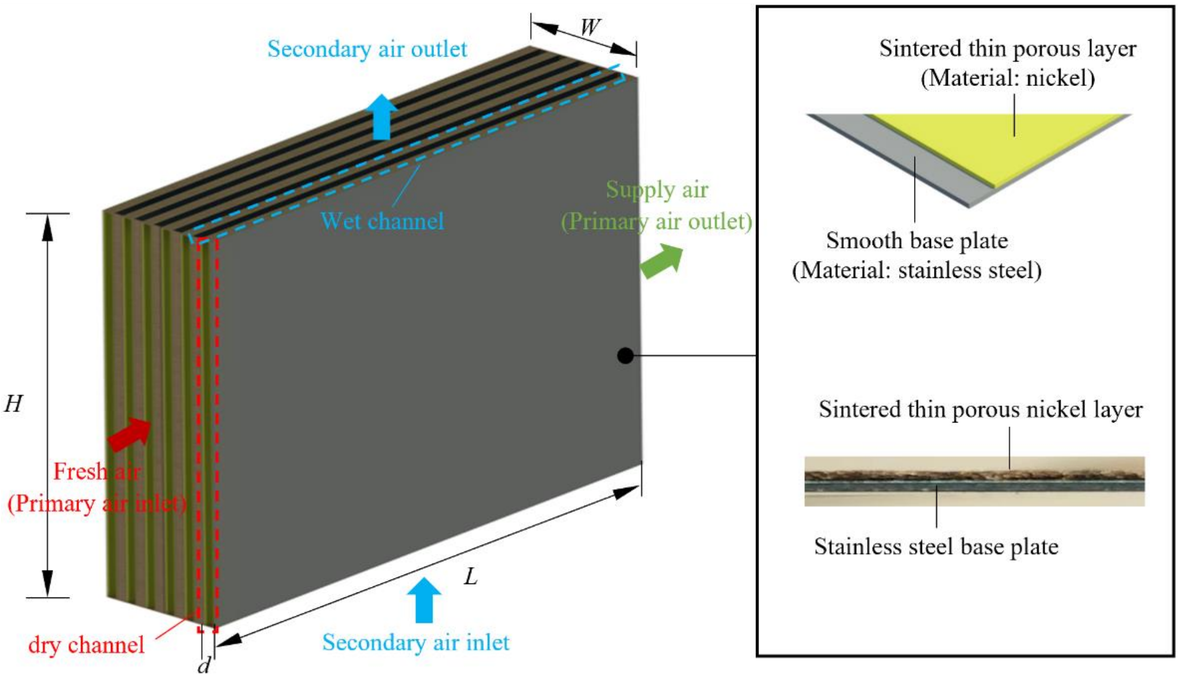

Fig. 3.1.4 Views of the cross-flow PIEC with the plate structure

For the hybrid plate, the upper porous nickel is to absorb and retain the water, while the below smooth metal plate can prevent water from seeping into the primary air channel. It needs to be emphasized that the plate with the porous media is only employed in the secondary air channel in this thesis. The stainless-steel surface towards the primary air channel has no special treatment. Scanning electron microscopy (SEM) [117], which uses a beam of highly energetic electrons to scan the surface of a sample and create high-resolution images of its topography and morphology, is employed to observe the micro-structure of the bare surface and porous zone. Fig. 3.1.5 displays the views of the smooth bare plate and the detailed structure of the sintered nickel porous layer captured by SEM. The specifications of the PIEC prototype manufactured for the experiments are listed in Table 3.1.3.

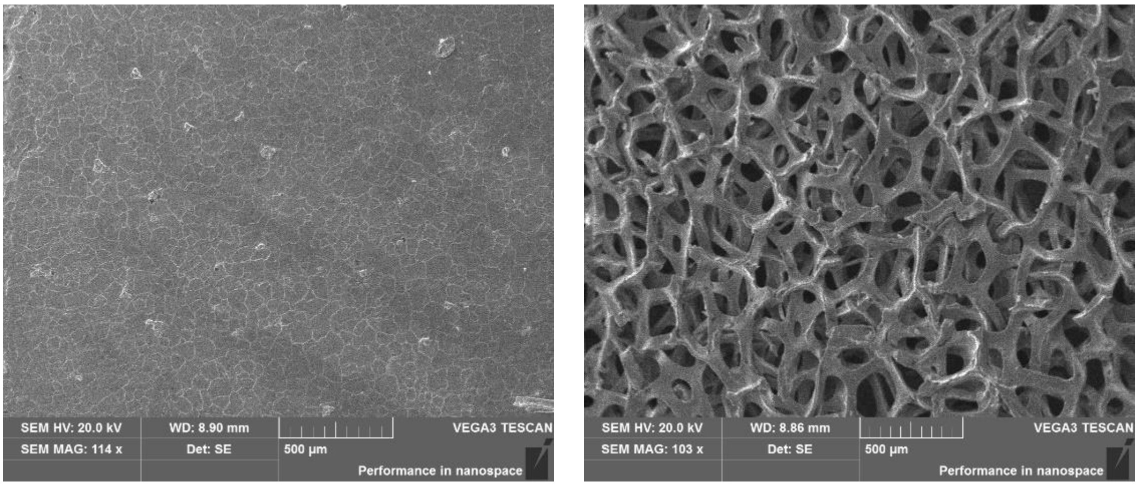

(a) (b)

Fig. 3.1.5 SEM pictures of (a) smooth surface of the base plate (b) sintered porous surface

Table 3.1.3 Basic specifications of the PIEC used in the experiment

Parameters	Specification/value
L (mm)	400
W (mm)	300
d (mm)	5
Number of channel pairs	8
Porosity (ε)	0.9
Pore diameter (um)	120-150
Thickness - base plate (mm)	0.5
Thickness -sintered porous layer (mm)	0.4

3.1.3 Water behavior on bare and porous surface

The hygroscopic property of the porous structure is expected to intensify the water storage capacity and improve the channel surface wettability compared with the smooth metal surface, which is an essential factor for effective cooling production. Therefore, the water retention tests that compare the characteristics of porous surfaces under spraying and non-spraying conditions were conducted. Comparison between the bare surface and porous surface is also carried out under spraying conditions. As shown in

Fig. 3.1.6, water was sprayed on half of the porous plate (the middle one), while the other half was kept dry (the right one) in the water retention test. The spraying duration lasted for 2 minutes, after which the plate stood vertically to the ground for 10 minutes. It could be observed that the sprayed water was absorbed in the tiny holes of the porous structure without forming big water droplets, as seen in the dark gray color on the middle of the plate. In contrast, for the right part in the figure, the porous surface was kept in dry conditions, thereby appearing lighter in color than the middle part. Additionally, the sintered nickel porous layer exhibited good sustainability, and the porous structure remained solid even though after repeated water retention tests. This indicates that the porous structure of the hybrid heat transfer metal plate of the PIEC has good water-absorbing ability under spraying conditions, which lays the foundation for cooling production without consistent water spraying. Nonetheless, for the left part, the water streamline can be easily noticed on the bare surface with large water droplets, and the distribution of water film is not uniform compared with the middle wetted porous surface.

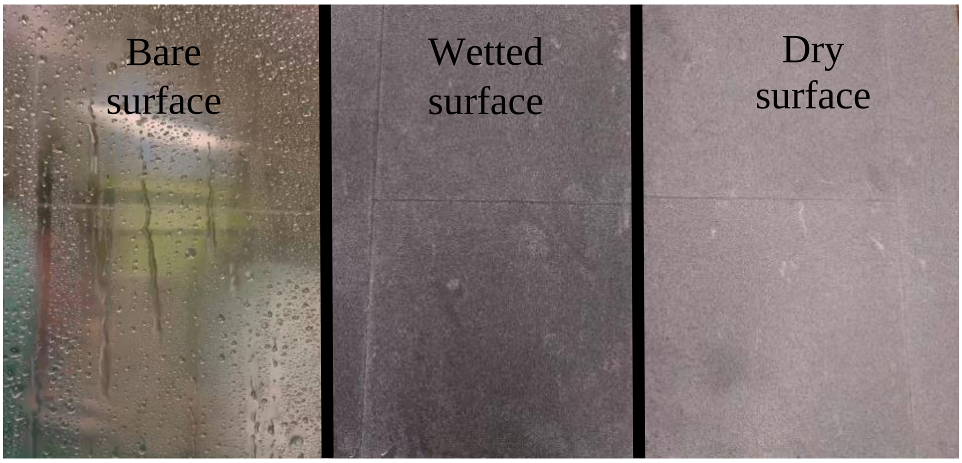

Fig. 3.1.6 Views of the bare surface and porous surface (left - bare surface; middle - porous surface in wet condition; right - porous surface in dry condition)

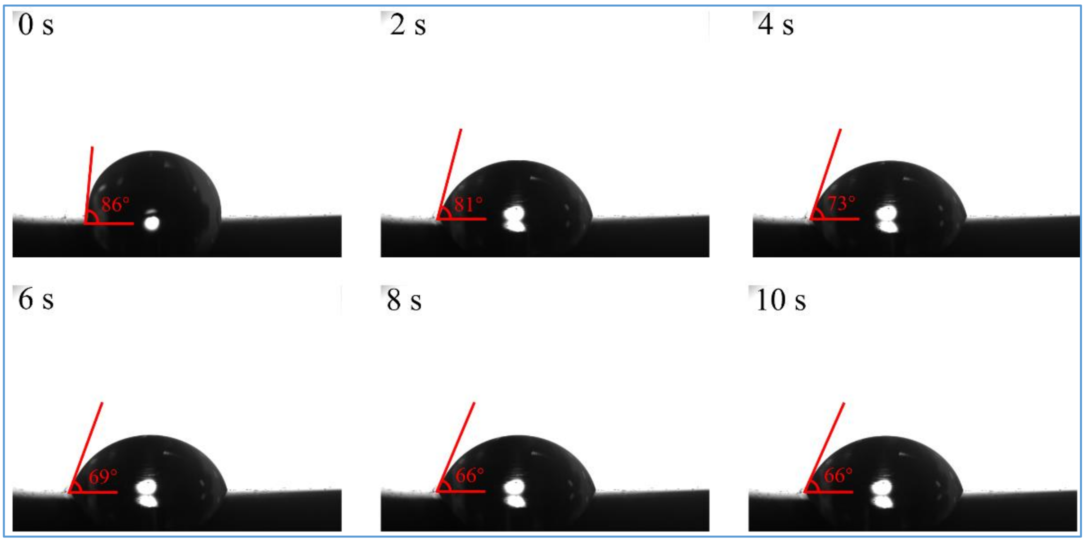

Fig. 3.1.7 The water droplet behavior on the stainless-steel bare surface

The behavior of water droplets on the bare surface and porous surface are captured as shown in Fig. 3.1.7 and Fig. 3.1.8. As shown in Fig. 3.1.7, the contact angle of water on a smooth stainless-steel surface is initially around 86°, which decreases to 66° within a span of 8 seconds. As known from the existing literature, contact angles greater than 90° signify hydrophobicity, whereas those below 90° represent hydrophilicity [118]. This evidence can confirm that stainless steel surfaces possess a certain degree of hydrophilicity. However, the hydrophilic effect of stainless steel is considerably inferior to that of porous media surfaces.

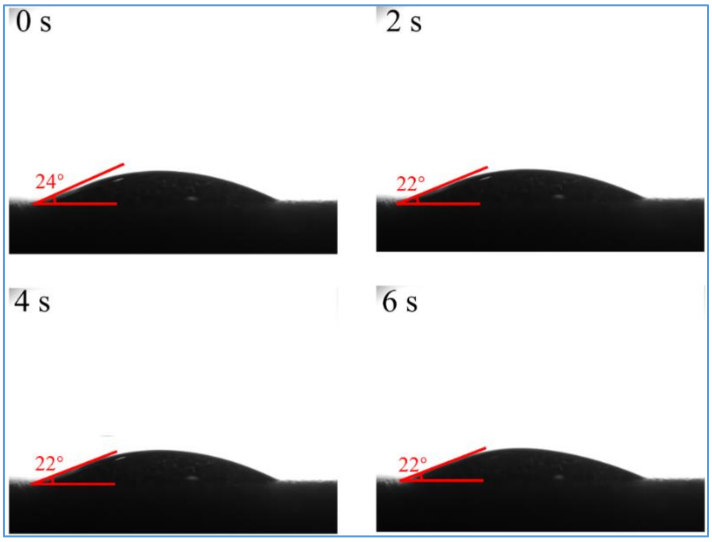

(a) Water fills the pores

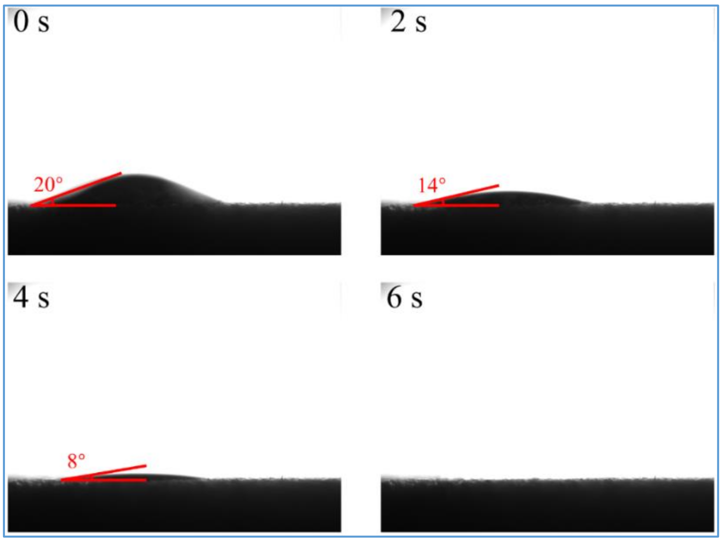

(b) Water does not fill the pores

Fig. 3.1.8 The water droplet behavior on the porous surface

The behavior of water on porous media surfaces can be categorized into two distinct cases. In the first case, when the pores are saturated with water, as illustrated in Fig. 3.1.8(a), the contact angle of water on the porous surface is 24°. Subsequently, it exhibits a slight decrease to 22° and remains constant thereafter. In the second case, when the pores are not entirely filled with water, as depicted in Fig. 3.1.8(b), the contact angle rapidly diminishes from 20° to 8° within the initial 4 seconds upon contact with surface. Concurrently, the height of water decreases significantly due to the availability of space within the porous region for water storage. By the sixth second, the water is entirely absorbed. Consequently, the contact angle of water on porous surfaces is substantially smaller than that on stainless steel surfaces, which indicates a higher degree of hydrophilicity in porous media surfaces.

3.1.4 Performance indicators and uncertainty analysis

The wet-bulb efficiency, pressure drop, cooling capacity, and *COP* are adopted to evaluate the performance of PIEC, which have been commonly used in the existing literature [52, 119]. The wet-bulb efficiency is defined as the ratio of the temperature difference between the inlet and outlet primary air to the temperature difference between the inlet primary air and the secondary air wet-bulb temperature. Cooling capacity is a measure of the ability of a cooling system to remove heat from a space or a process. The coefficient of performance (*COP*) is a measure of the efficiency of a heating or cooling system. In the heating system, it is defined as the ratio of the heat output of the system to the energy input. In the case of a cooling system, *COP* is defined as the ratio of the cooling capacity to the electrical power input. The corresponding equations of them are expressed from Eq. (1) to Eq. (3).

$$\eta_{wb} = \frac{t_{p,in} - t_{p,out}}{t_{s,in} - t_{wb,s,in}} \tag{1}$$

$$Q_c = m_p c_{pa} \left(t_{p,in} - t_{p,out} \right) \tag{2}$$

$$COP = \frac{Q_c}{W} \tag{3}$$

where η_{wb} is wet-bulb efficiency;

$t_{p,in}$ and $t_{p,out}$ are inlet and outlet temperature of primary air channel, °C;

$t_{s,in}$ and $t_{wb,s,in}$ are dry-bulb and wet-bulb secondary air inlet temperature, °C;

Q_c is cooling capacity, W;

m_p is the mass flow of primary air, kg/s;

c_{pa} is specific heat of air, J/(kg·°C);

W is power, W.

Different air velocities and the on/off mode of the spraying system can both influence the pressure drop, especially in the secondary air channel. The pressure drop is written by Eq. (4).

$$\triangle P = P_{in} - P_{out} \tag{4}$$

Uncertainty analysis is the process of quantifying and understanding the various sources of uncertainty in a given system or model. The goal of uncertainty analysis is to identify the sources of uncertainty in a system, quantify their impact, and propagate them through the system to estimate the overall uncertainty in the final result [120]. In this thesis, uncertainties of the data result from errors due to instruments during the experiment process, which are calculated by the propagation of error equations expressed as Eq. (5) and Eq. (6) [121, 122]. According to the initial uncertainty information of each measuring equipment listed in Table 3.1.1, uncertainties of wet-bulb efficiency, cooling capacity, and *COP* are worked out as 4.74%, 3.19%, and 8.34%, respectively.

$$U = f(X_1, X_2, \cdots, X_n) \tag{5}$$

$$\delta U = \sqrt{(\frac{\partial Y}{\partial X_1}\delta X_1)^2 + (\frac{\partial Y}{\partial X_2}\delta X_2)^2 + \cdots + (\frac{\partial Y}{\partial X_n}\delta X_n)^2} \tag{6}$$

where δU represents the overall uncertainty of the target indicator; X_1 to X_n are the influential factors.

3.2 Results and discussion

The results of experiments conducted on the PIEC prototype are presented from two perspectives: 1) the steady state and 2) the dynamic state. During the steady state, water spraying is continuous and stable from the beginning to the end of tests, while it is interrupted during the dynamic state. The performance of the PIEC prototype for cooling outdoor fresh air is evaluated, and the test ranges of different variables are listed in Table 3.2.1.

Before discussing the experimental results, the energy balance of the data should be checked. Therefore, the comparison was carried out between the enthalpy loss and enthalpy gain that occurred in adjacent primary air and secondary air channels. The energy equations for the air streams in two adjacent channels were written as Eq. (7) and Eq. (8).

$$Q_p = m_p c_{pa}\left(i_{p,in} - i_{p,out}\right) \tag{7}$$

$$Q_s = m_s c_{pa}\left(i_{s,out} - i_{s,in}\right) \tag{8}$$

where m_p is the mass flow of primary air, kg/s;

m_s is the mass flow of secondary air, kg/s;

c_{pa} is specific heat of air, J/(kg·°C);

$i_{p,in}$ and $i_{p,out}$ are the inlet and outlet enthalpy of primary air, kJ/kg;

$i_{s,out}$ and $i_{s,in}$ are the inlet and outlet enthalpy of secondary air, kJ/kg.

Table 3.2.1 Test conditions of the PIEC under steady state

Variables	$t_{p,in}$ (°C)	v_p (m/s)	v_s (m/s)	$t_{s,in}$ (°C)	RH_s (%)
$t_{p,in}$ (°C)	[26, 2, 32]	2.5	3	23	70
v_p (m/s)	32	[2, 0.5, 3.5]	3		
v_s (m/s)	32	2.5	[2, 0.5, 3.5]		

Note: [a, b, c]: a – Start value; b – Interval; c – End value.

The energy gain and energy loss of two adjacent channels in Fig. 3.2.1. It can be observed that the maximum discrepancy between the enthalpy loss and enthalpy gain was within ±20%, and most of the points fall within the 10% deviation line. This indicates that the data collected from the experiments were acceptable and could be used for further analysis.

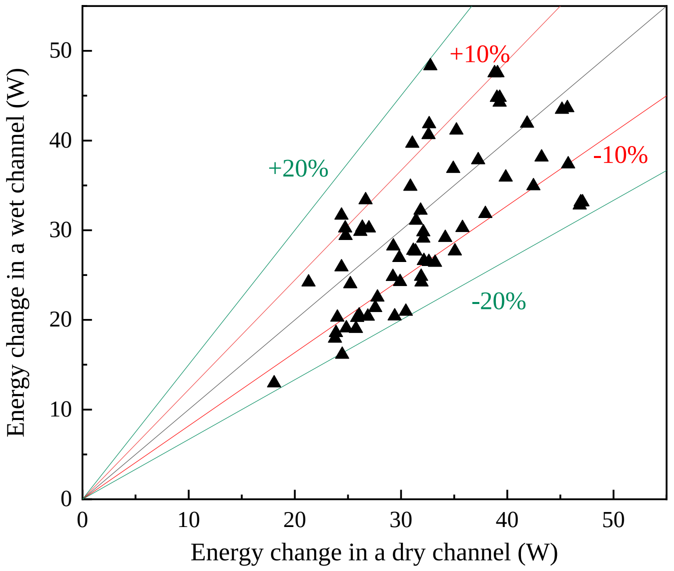

Fig. 3.2.1 Energy balance comparison of two adjacent channels

3.2.1 Steady state

To ensure the effective wettability of the channels in the PIEC prototype, the wet channel surfaces were moisturized for 5 minutes prior to starting each experiment. In the steady state, the water pump operated continuously at a constant speed with a power demand of 26 W during the test period. The effects of selected influential parameters on the wet-bulb efficiency, cooling capacity, and *COP* are accordingly illustrated as follows.

3.2.1.1 Effect of primary inlet air temperature

Fig. 3.2.2 illustrates the variations in wet-bulb efficiency, cooling capacity, and *COP* of the PIEC prototype as the primary air temperature increases within the test range. The rising inlet temperature corresponds to an improvement in these three performance indicators. It shows that as the primary air temperature increases, the corresponding improvement happens to these three performance indicators. Specifically, the wet-bulb efficiency was found to be positively related to the increasing temperature. It started at 0.57 and reached 0.61 with the inlet temperature increasing from 26℃ to 32℃. This indicates that the PIEC prototype is more effective when supplied with higher-temperature primary air. Regarding cooling capacity, the PIEC prototype was capable of producing up to 285 W of cooling when supplied with 32℃ hot fresh air. As the temperature of the primary air entering the PIEC increases, there is a corresponding increase in the cooling load that the system can handle. The *COP* value of the PIEC prototype was found to increase from 3.3 to 6.6 with higher temperatures, with the fan and pump operation status remaining constant. This indicates that the system becomes more energy-efficient as the temperature of the primary air increases.

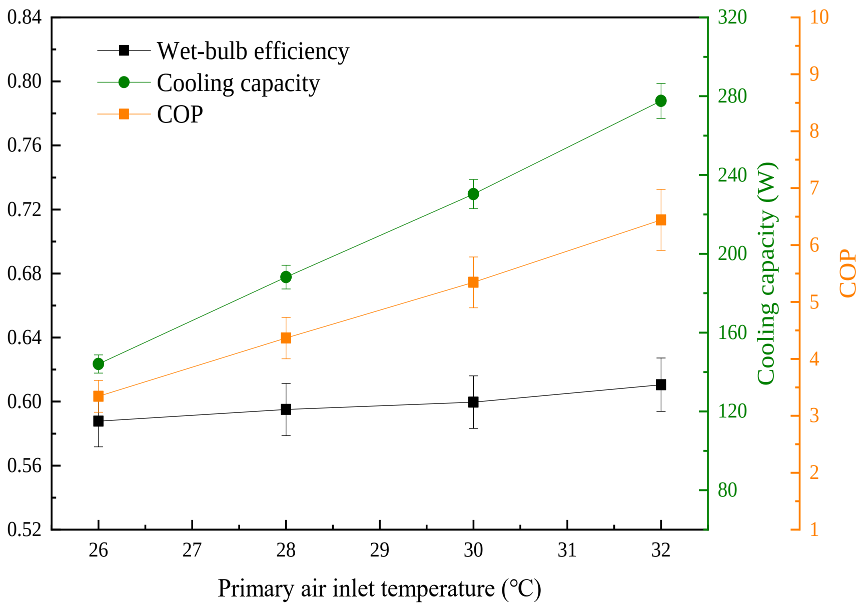

Fig. 3.2.2 Effect of primary air inlet temperature on wet-bulb efficiency, cooling capacity, and *COP*

3.2.1.2 Effect of primary air velocity

The pressure drop in the dry channel and the power variation caused by the primary air fan were evaluated and presented in Fig. 3.2.3(a). as the airflow volume input in the dry channels increased, there was a corresponding increase in power consumption and pressure drop. Specifically, the primary air fan power load increased from 3.5 W at 2 m/s channel air velocity to 9.1 W at 3.5 m/s, accompanied by a rise in pressure difference from 5.9 Pa to 20 Pa.

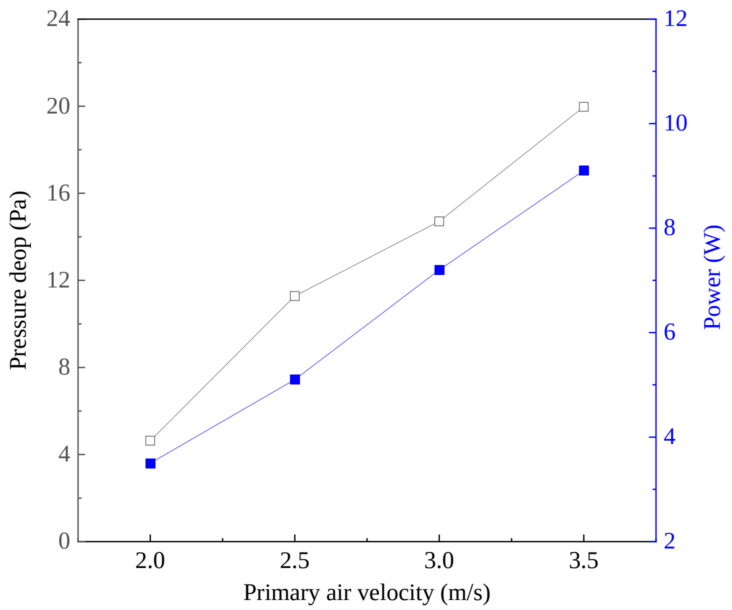

(a)

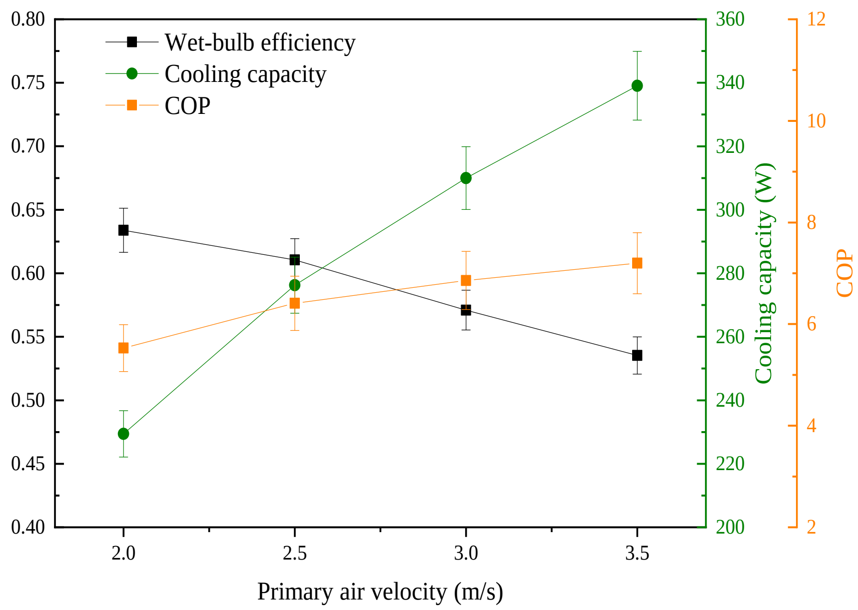

(b)

Fig. 3.2.3 (a) Pressure drop and power consumption with primary air velocity (b) Effect of primary air inlet temperature on wet-bulb efficiency, cooling capacity, and *COP*

The tendencies of the three performance indexes against the varied primary air velocity under steady state are shown in Fig. 3.2.3(b). It could be seen that the wet-bulb efficiency decreases with the growing with increasing primary air velocity, while the cooling capacity and *COP* are enhanced. Specifically, the wet-bulb efficiency of the PIEC declined rapidly from 0.66

to 0.53. The larger cooling capacity output could be attributed to higher air velocity ranging from 2 m/s to 3.5 m/s, which correspondingly expanded from 243.4 W to 345.8 W. Additionally, the system *COP* was noticeably enlarged from 5.9 to 7.3.

As the growing air velocity could negatively influence the wet-bulb efficiency but improve the cooling capacity and *COP*, the trade-off between the wet-bulb efficiency and *COP* needs to be taken into consideration. The single optimization can be generally categorized into two directions. On the one hand, if the purpose is to obtain a lower supply air temperature, the air velocity should be decreased, or the channel number can be increased in the design stage. On the other hand, if the goal is to achieve the higher *COP* for energy saving, the air velocity can be higher, given the circumstance that the requirement of outlet temperature is relatively loose. The detailed multi-objective optimizations would be illustrated in Chapter 5.

3.2.1.3 Effect of secondary air velocity

The impact of increasing the secondary air flowing speed on the performance of the PIEC prototype was evaluated, and the results are presented in Fig. 3.2.4. Enlarging the secondary air flowing speed leads to additional power load and pressure drop. The power consumption of the PIEC prototype increased from 7.2 W to 15.4 W with increasing secondary air velocity from 2 m/s to 3.5 m/s. Owing to the high airflow volume input, the significant growth of the pressure drop of the secondary air channel starts from 7.8 Pa under 2 m/s and reaches 34.3 Pa in the case of 3.5 m/s.

Concerning the effects on the three performance indicators, the higher secondary air velocity was found to enhance wet-bulb efficiency and cooling capacity since the heat transfer rate is positively related to velocity. As shown in Fig. 3.2.4(b), the wet-bulb efficiency of the PIEC prototype increased from 0.56 to 0.63 with the development of secondary airspeed from 2 m/s to 3.5 m/s. The cooling load removed from the dry channel increased by 29 W. However, the COP curve showed an opposite trend as it dropped from 6.8 to 6.3, indicating that more power needs to be input when the PIEC handles the same unit of heat.

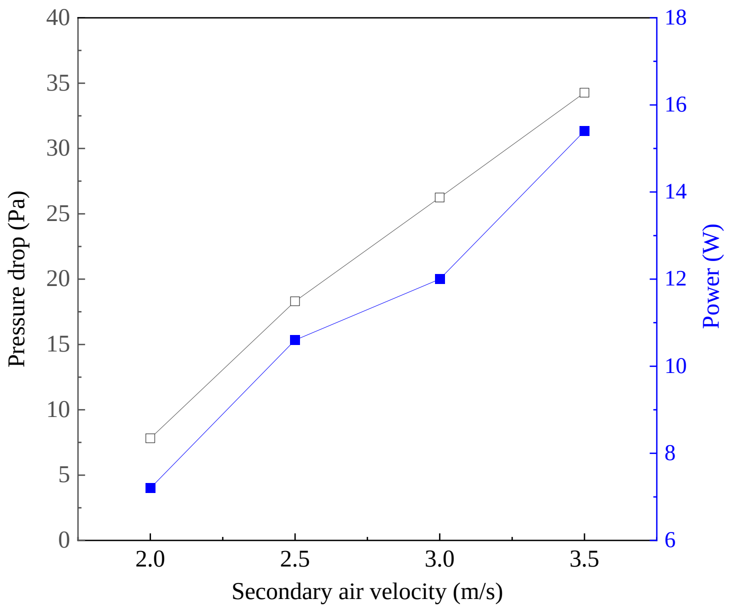

(a)

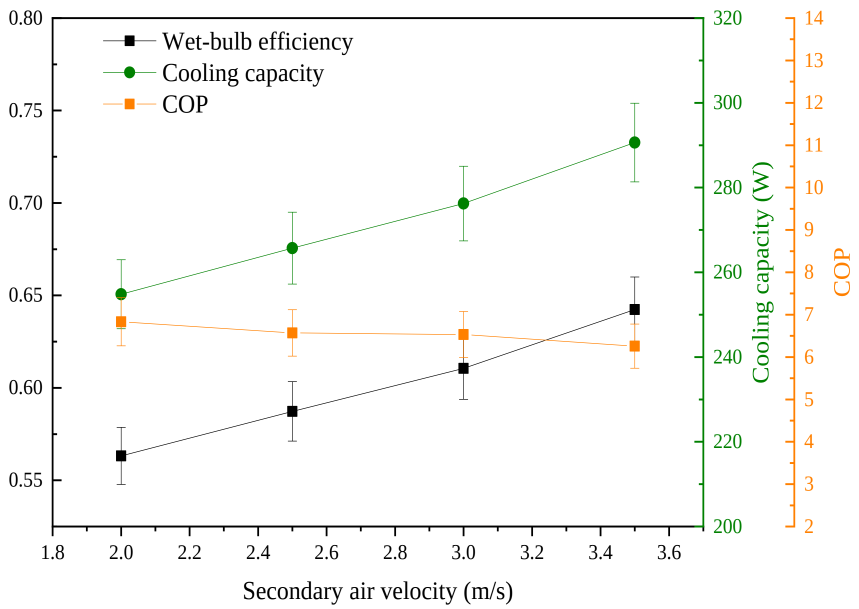

(b)

Fig. 3.2.4 (a) Pressure drop and power consumption (b) Effect of primary air inlet temperature on wet-bulb efficiency, cooling capacity, and *COP*

As with the results presented in section 3.2.1.2, the trade-off between wet-bulb efficiency and *COP* is a key consideration when increasing secondary air velocity. Blowing more air into the wet channel is a viable option when the priority is to achieve a lower outlet temperature. However, this comes at the cost of significantly higher power consumption, with only a marginal temperature drop of 0.8℃ achieved. Conversely, when the primary aim is to save energy, reducing the velocity of secondary air is recommended. This would require a trade-off between wet-bulb efficiency and cooling capacity with a corresponding increase in *COP*. Again, the multi-objective optimizations between the controllable parameters are carried out in Chapter 5.

3.2.2 Dynamic state

The water retention test has demonstrated that the porous material can provide the space to temporarily store the water. Owing to the water storage capability of the porous material in secondary channel surfaces, the water spraying system can be interrupted for a period of time, and the stored water in the porous zone supports the evaporation process so that the primary air outlet temperature of PIEC can be sustained for some time under this circumstance. In other words, the spraying system is expected to operate intermittently and replace the traditional consistent mode in the PIEC system. Experiments under dynamic state were therefore carried out to not only explore the feasibility of the novel spraying strategy but also investigate the cooling performance in this condition.

Generally, experiments were divided into two groups. The first set of experiments aimed to monitor the temperature variation process of the wetted PIEC system over a 3600-second period under non-spraying conditions. The results of this group provided valuable insights into the time-dependent cooling performance of the system and enabled the determination of temperature thresholds that would trigger the restoration of the water supply. The temperature thresholds obtained from the first set of experiments were then used in the second group of tests, which involved periodic spraying based on these thresholds. Each test case in the second group experiments received several temperature cycles, allowing for a more comprehensive analysis of the PIEC system's performance under dynamic conditions. The periodic spraying strategies were to maintain the outlet temperature of the PIEC system within a predetermined range.

During the preparation stage of the experiments, the PIEC prototype was sprayed by top nozzles for 5 minutes to ensure it was fully moist before each test. The water used for spraying was directly sourced from the domestic water system in the building, and the water flow rate and temperature were measured as 0.03 kg/s and 22℃, respectively. These values remained constant throughout the spraying period. Following the preparation stage, the fans were in operation. In the first group tests, the water system was fully stopped when it made the primary air outlet temperature to the minimum value as in the consistent spraying mode. In the second group tests, the water spraying resumed working for 2 minutes when the outlet temperatures reached threshold values. To enhance the cooling performance, the cool exhaust air from the indoor space was introduced as the secondary air, similar to the tests conducted under steady-state conditions. Table 3.2.2 lists the setting ranges and values of the essential parameters for the dynamic tests of PIEC.

Table 3.2.2 Test conditions for PIEC prototype under dynamic state

Variables	$t_{p,in}$ (℃)	v_p (m/s)	v_s (m/s)	t_s (℃)	RH_s (%)
$t_{p,in}$ (℃)	[26, 2, 32]	2.5	3		
v_p (m/s)	32	[2, 0.5, 3.5]	3	23	70
v_s (m/s)	32	2.5	[2, 0.5, 3.5]		

Note: Two test groups: I) No water respraying; II) 6000 s with intermittent water supply.

[a, b, c]: a–start value; b–interval; c–end value.

3.2.2.1 Effect of primary inlet air temperature

Fig. 3.2.5(a) presents the influence of different inlet temperatures on the supply air temperature of the PIEC when the spraying water is not provided all the time. Four different inlet air temperatures ranging from 26℃ to 32℃ were tested, and all scenarios exhibited a similar trend. After the secondary air fan started operating, the supply air temperature dropped sharply initially, and the rate of decrease gradually slowed down as the temperature approached the lowest value that the PIEC system could achieve. The coolest temperatures achieved were 22.1℃, 22.9℃, 23.5℃, and 24.1℃ for the four different inlet air temperatures tested. Following this, the temperature slightly increased for a duration as the limited water content present in the porous material was evaporated. Toward the end of the experiment, a faster temperature growth was observed as the water content was reduced. The supply air temperature ultimately ends up at 23.6℃, 24.6℃, 25.7℃, and 26.5℃ at 3600 seconds for the different inlet air temperatures tested.

The temperature growth observed at the end of the experiment highlights the importance of periodic spraying to maintain the acceptable cooling performance of the PIEC system over time. Since the outlet temperature of the PIEC would gradually increase, it is crucial to recover the water distributed to the secondary air channels at a certain temperature threshold to maintain the supply air temperature within a reasonable range. In this study, the threshold was determined as 0.5℃ above the lowest temperature because the fluctuation of 0.5℃ is not only acceptable in the AC system but also can prevent the water pump from being excessively repeated between on/off conditions. Following the rule, the water would be resprayed for 2 minutes (120 s) when the temperatures increased 0.5℃ from the lowest temperature every time. Fig. 3.2.5(b) shows the results of several cycles realized using the intermittent spraying plans over a period of 6000 seconds, and the time interval of the non-spraying period was identified. It can be noticed that the higher inlet air temperatures significantly reduced the entire cycle duration. The interval of the non-spraying period was 2105 seconds for an inlet air temperature of 26℃, while it was reduced to 1398 seconds for an inlet air temperature of 32℃. As a result, up to 94.6% of the pump operation time could be saved.

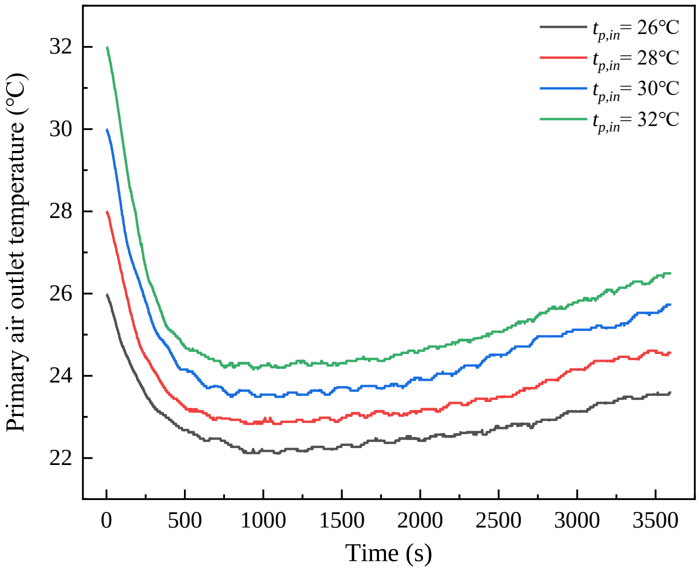

(a)

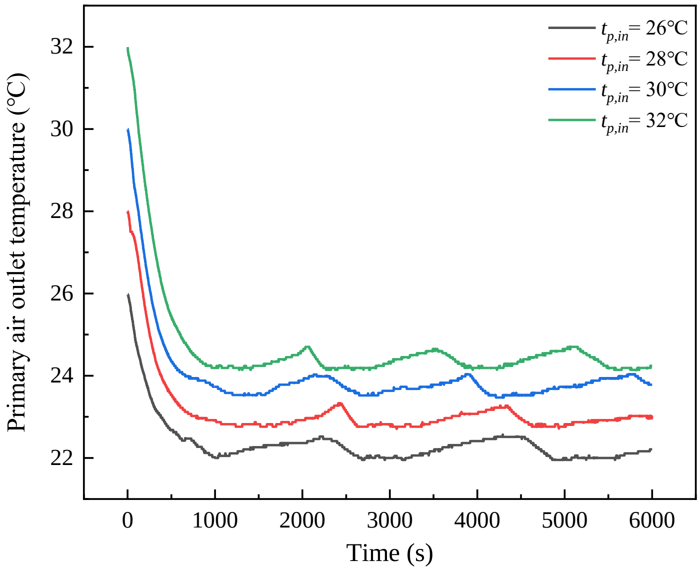

(b)

Fig. 3.2.5 (a) Effect of primary air inlet temperature on variations of supply air outlet temperature in 3600 s (b) Primary air outlet temperature variations with intermittent water spraying modes in 6000 s

3.2.2.2 Effect of primary air velocity

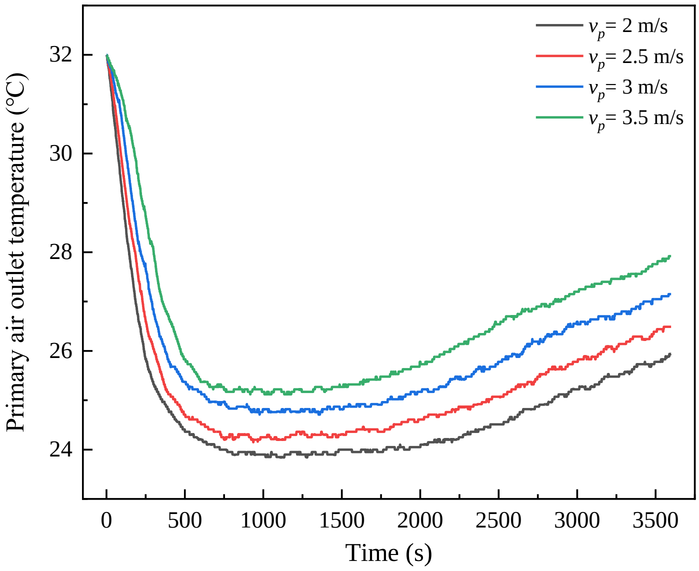

(a)

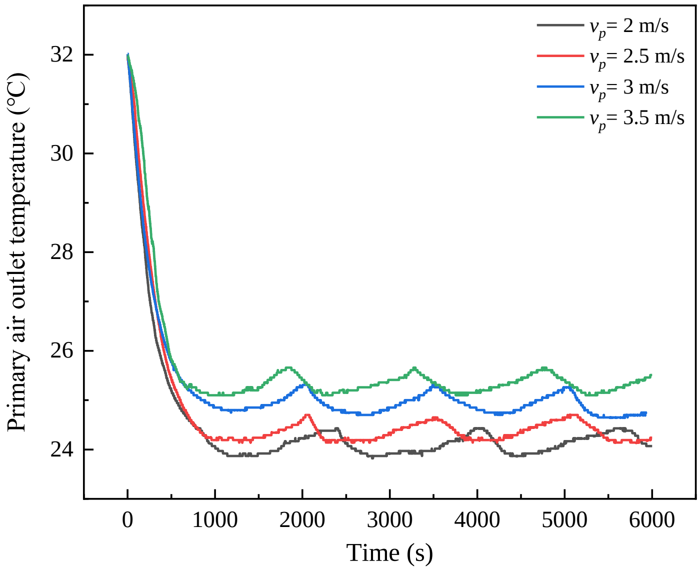

(b)

Fig. 3.2.6 (a) Effect of primary air velocity on variations of supply air outlet temperature (b) Primary air outlet temperature variations with intermittent water spraying modes in 6000 s

The tendencies of supply air outlet temperature with various primary air velocities are displayed in Fig. 3.2.6(a). It was seen that a higher primary air velocity resulted in a greater outlet temperature. Initially, the temperature sharply decreased, and the lowest temperatures achieved by the PIEC system increased from 23.8℃ to 25.1℃ with airspeeds ranging from 2 m/s to 3.5 m/s. Following this initial decrease, there was a period with a slight temperature improvement. However, without water replenishment to the secondary air porous layer, the supply air temperature continued to increase and ultimately reached 25.9℃, 26.5℃, 27.2℃, and 27.9℃ at 3600 seconds for the different primary air velocities tested.

Based on the threshold rules of 0.5℃ established in the study, the turning points that triggered the restarting of water spraying were determined to be around 24.3℃, 24.6℃, 25.2℃, and 25.6℃ for the increasing primary air velocities in the four scenarios tested. As a result of the repeated water spraying, the temperature fluctuation profiles and non-spraying durations were calculated. As presented in Fig. 3.2.6(b), the higher primary air velocities resulted in shorter total cycle spans and reduced intervals for the water system. The longest non-spraying period was observed to be 1461 seconds when the primary air velocity was 2 m/s, corresponding to a 92.4% reduction in working time. However, this duration was reduced to 1318 seconds for a primary air velocity of 3.5 m/s.

3.2.2.3 Effect of secondary air velocity

Fig. 3.2.7(a) illustrates the effect of secondary air velocity on the supply air temperature. The temperature decreased rapidly in all four cases once the secondary air fan was turned on. The rate of decrease gradually slowed down as the temperature approached the lowest value, which varied from 24.7℃ to 24℃ with increasing velocities from 2 m/s to 3.5 m/s. After 3600 seconds of testing, the final temperatures end up at 26.4℃, 26.6℃, 26.5℃, and 26.8℃ for the different secondary air velocities tested. Based on the minimum temperature obtained in Fig. 3.2.7(a), the thresholds that recover the water system operation were decided from 25.2℃ to 24.5℃ in these four cases. Based on these temperature thresholds, the on/off status of the water pump was switched, and the temperature profiles were investigated over a period of 6000 seconds, as shown in Fig. 3.2.7(b). The results demonstrated that higher secondary air velocities resulted in shorter cycle spans, leading to a reduced non-spraying period. The non-spraying period was reduced from 1646 seconds to 1362 seconds when the velocity was increased from 2 m/s to 3.5 m/s, corresponding to a 93.2% and 91.9% reduction in pump operation time, respectively.

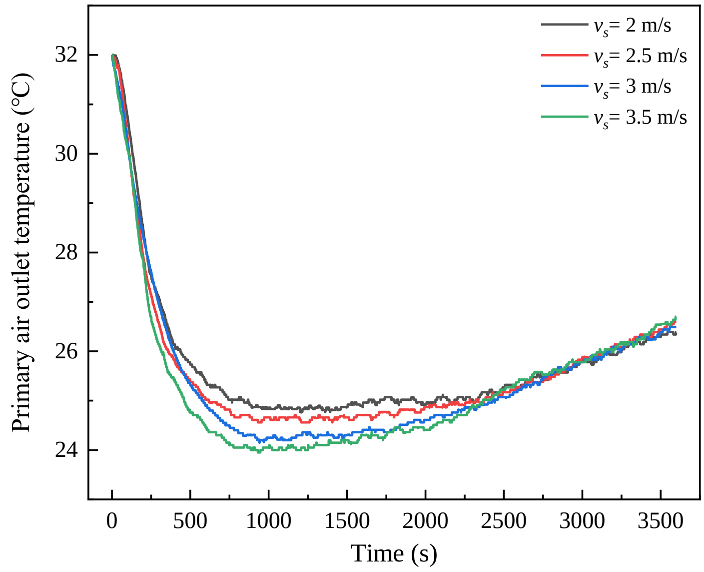

(a)

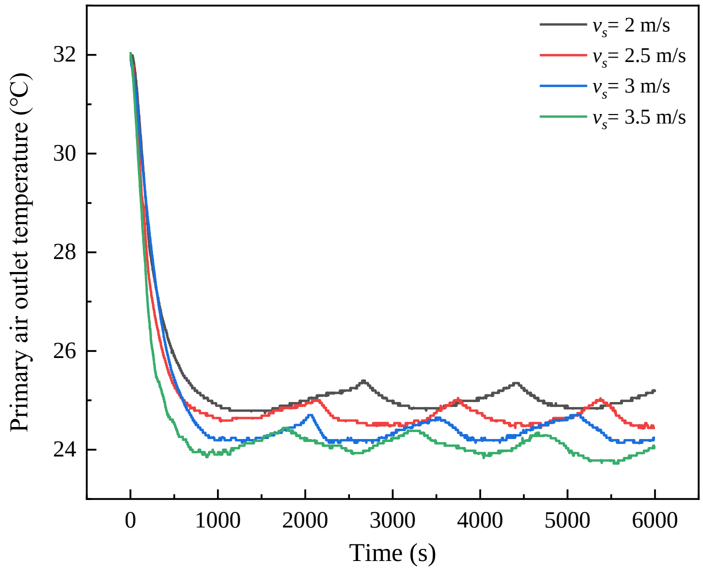

(b)

Fig. 3.2.7 (a) Effect of secondary air velocity on variations of primary air outlet temperature (b) Primary air outlet temperature variations with intermittent water spraying modes in 6000 s

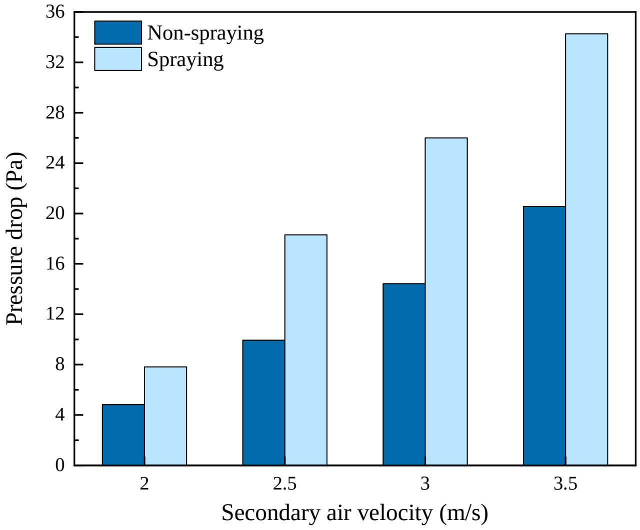

Fig. 3.2.8 Pressure drop comparison between spraying and non-spraying conditions

In addition, the average pressure drops under the non-spraying period were measured during the test span, which were compared with that in spraying mode under steady state. As seen from Fig. 3.2.8, the pressure drops under the spraying condition were all greater than those under the non-spraying condition, indicating that water spraying caused an additional pressure drop in the secondary air channel. Moreover, the pressure drop differences between the two modes increased from 3 Pa to 13.7 Pa with higher secondary air velocities.

3.3 Summary

This chapter presents an experimental investigation of the cooling potential of a plate-type indirect evaporative cooler with sintered thin porous layer (PIEC) on the secondary air channel surfaces. A PIEC prototype was proposed, designed, and manufactured for a series of group tests that were conducted on the established lab test rig with controllable air properties and water supply systems. The cool exhaust air from the indoor environment was utilized as the secondary air to strengthen the evaporative cooling effect. The purpose of the experiments is not only to investigate the water retention ability of the porous structure of the PIEC and explore the feasibility of using different spraying modes for the PIEC, but also to investigate the PIEC cooling performance under different spraying conditions and to collect the real data for the validation of the PIEC simulation model. The impacts of primary air inlet temperature, primary air velocity, and secondary air velocity on the performance of the PIEC system were examined in both steady and dynamic states. The main findings from this chapter are summarized as follows.

(1) The higher primary air inlet temperature and secondary air velocity, as well as lower primary air velocity, contributed to the greater wet-bulb efficiency, which was up to 0.642 for this PIEC prototype. In the tested steady state, the maximum cooling capacity and *COP* of this PIEC system were evaluated as 339.1 W and 7.2.

(2) The contact angle of water on porous surfaces is substantially smaller than that on stainless-steel surfaces, which indicates a higher degree of hydrophilicity in porous media surfaces.

(3) The porous structure on the PIEC hybrid heat transfer plate provided a water storage place, and the sintered porous layer on the wet channel surface showed reliable water retention ability so as to demonstrate the feasibility of the intermittent spraying strategy. Meanwhile, the pressure drop caused by secondary air channels under the non-spraying conditions was identified to be lower than that under the continuous spraying mode.

(4) A threshold temperature rise of 0.5°C above the lowest temperature was obtained from dynamic tests as the signal to restart the water pump. The cycle durations and intervals for non-spraying time were determined, with the longest interval being 2105 seconds, corresponding to a 94.6% reduction in pump operation time. By adopting the newly achieved intermittent spraying rather than the conventional consistent spraying, the *COP*s of the PIEC system were improved by 117.5% on average, with the most significant *COP* measured as 17.3.

Chapter 4 Modeling the PIEC with dual spraying modes

In this chapter, a three-dimensional (3-D) model was established for the proposed indirect evaporative cooler with porous material on the secondary air channel surface (PIEC) to predict the cooling performance under consistent and periodic spraying conditions. The model was validated by the experimental data collected from Chapter 3. The temperature and humidity distributions over time were presented based on this 3-D model, and the effects of essential parameters on the cooling performance were identified.

This chapter is written based on a published paper of this thesis author. The paper is titled "*Dynamic performance evaluation of porous indirect evaporative cooling system with intermittent spraying strategies*" in *Applied Energy*.

4.1 Model establishment

In this section, the plate-type cross-flow PIEC model was established to predict the cooling performance. As depicted in Fig. 4.1.1, the physical model consists of half of a primary air channel and half of a secondary air channel. The primary air flows in the horizontal direction from the left to the right side in one channel, and the secondary air passes the channel in the vertical direction from the bottom to the top side in the adjacent channel. Before the model establishment, some commonly-used assumptions related to the heat and mass transfer processes and porous medium of IEC are listed as follows [123-125].

- The water and air are considered to be steady and incompressible in two channels, and the air velocity field is assumed to be time-independence.
- Air and water vapor both follow the ideal gas law.
- The flow status in both the free zone and the porous zone is regarded as the laminar flow.
- There is no heat and mass transfer between the PIEC and its surrounding environment.

- The liquid water that leaves from the porous material is only in the form of vapor.
- The medium is continuous and homogeneous, and pores are evenly distributed in similar geometric sizes with no closed air cavity.
- No chemical reactions happen among the solid phase, liquid phase, and gas phase in the porous media.
- The total volume of the solid, liquid, and gas phases is constant. The water-absorbing, evaporation, and temperature fluctuation will not cause the shrink or expansion of the solid matrix.
- The convective heat transfer within the porous media and the effects of gravitation are both ignored.

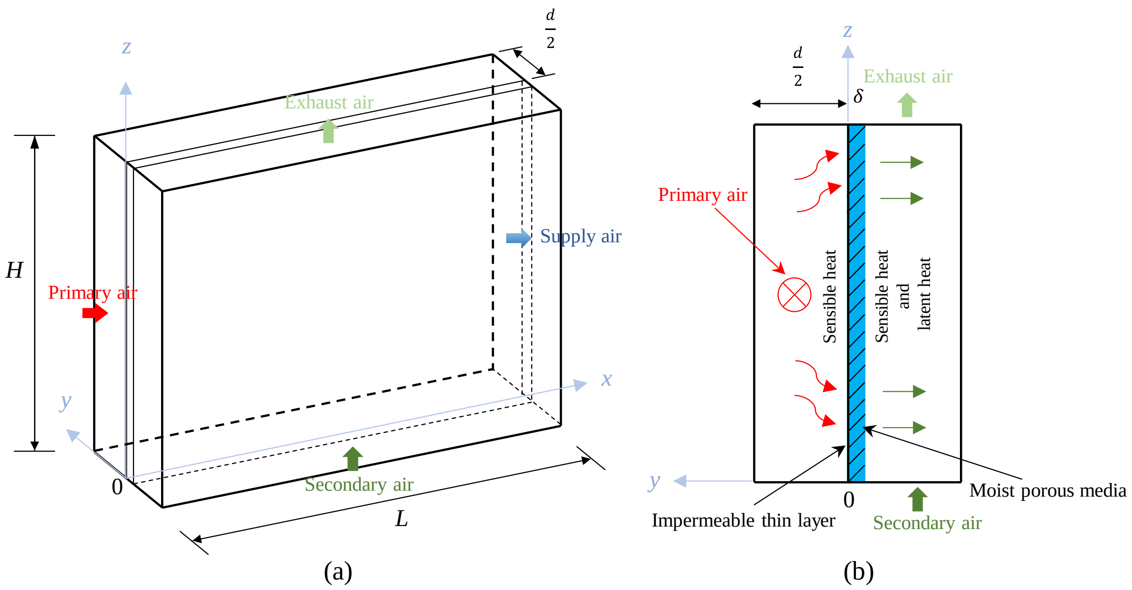

Fig. 4.1.1 (a) structure and (b) Left side view of the cross-flow PIEC with two adjacent half channels

4.1.1 Free zone

The physical model of IEC contains two free zones and a porous zone. Free zones are full of moist air, while the porous zone includes the moist air (gas phase) and the liquid water (liquid phase), and the porous skeleton (solid phase).

Regarding the free zone that includes primary air and secondary air, the continuity equation is written by Eq. (9).

$$\frac{\partial u_i}{\partial x} + \frac{\partial v_i}{\partial y} + \frac{\partial w_i}{\partial z} = 0 \tag{9}$$

where u, v and w are velocities in the x, y, z directions, m/s.

The momentum conservation equations can be expressed from Eq. (10) to Eq. (12).

$$\frac{\partial u_i}{\partial \tau} - \frac{1}{\rho}\frac{\partial P_i}{\partial x} + \frac{\mu}{\rho}\left(\frac{\partial^2 u_i}{\partial x^2} + \frac{\partial^2 u_i}{\partial y^2} + \frac{\partial^2 u_i}{\partial z^2}\right) - \left(u_i\frac{\partial u_i}{\partial x} + v_i\frac{\partial v_i}{\partial y} + w_i\frac{\partial w_i}{\partial z}\right) = 0 \tag{10}$$

$$\frac{\partial v_i}{\partial \tau} - \frac{1}{\rho}\frac{\partial P_i}{\partial y} + \frac{\mu}{\rho}\left(\frac{\partial^2 v_i}{\partial x^2} + \frac{\partial^2 v_i}{\partial y^2} + \frac{\partial^2 v_i}{\partial z^2}\right) - \left(u_i\frac{\partial u_i}{\partial x} + v_i\frac{\partial v_i}{\partial y} + w_i\frac{\partial w_i}{\partial z}\right) = 0 \tag{11}$$

$$\frac{\partial w_i}{\partial \tau} - \frac{1}{\rho}\frac{\partial P_i}{\partial z} + \frac{\mu}{\rho}\left(\frac{\partial^2 w_i}{\partial x^2} + \frac{\partial^2 w_i}{\partial y^2} + \frac{\partial^2 w_i}{\partial z^2}\right) - \left(u_i\frac{\partial u_i}{\partial x} + v_i\frac{\partial v_i}{\partial y} + w_i\frac{\partial w_i}{\partial z}\right) = 0 \tag{12}$$

$$i = p, s$$

where ρ is fluid density, kg/m^3;

P is fluid pressure, Pa;

μ is fluid viscosity, Pa·s;

τ is the time variable, s.

The energy equation is formulated by Eq. (13), and the species diffusion equation in the secondary air channel is written in Eq. (14).

$$\rho_g C_{pg}\left(\frac{\partial T_i}{\partial \tau} + u_i\frac{\partial T_i}{\partial x} + v_i\frac{\partial T_i}{\partial y} + w_i\frac{\partial T_i}{\partial z}\right) = k_g\left(\frac{\partial^2 T_i}{\partial x^2} + \frac{\partial^2 T_i}{\partial y^2} + \frac{\partial^2 T_i}{\partial z^2}\right) \tag{13}$$

$$i = p, s$$

where k_g is the thermal conductivity of the gas, W/(m·K);

T is temperature, K;

C_{pg} is the specific heat capacity of the gas at constant pressure, J/(kg·K).

$$\frac{\partial C_s}{\partial \tau} + u_s \frac{\partial C_s}{\partial x} + v_s \frac{\partial C_s}{\partial y} + w_s \frac{\partial C_s}{\partial z} = D_{va} \left(\frac{\partial^2 C_s}{\partial x^2} + \frac{\partial^2 C_s}{\partial y^2} + \frac{\partial^2 C_s}{\partial z^2} \right) \tag{14}$$

where D_{va} is diffusion coefficient of the substance, m²/s;

C_s is the concentration of the substance, mol/m³;

C_{pg} is the specific heat capacity of the gas at constant pressure, J/(kg·K).

The relationship between saturation pressure and temperature is given by Eq. (15) and Eq. (16) [12].

$$ln(P_{sat}) = \frac{e_1}{T_{sf}} + e_2 + e_3 T_{sf} + e_4 T_{sf}^2 + e_5 T_{sf}^3 + e_6 ln T_{sf} \tag{15}$$

$$C_{sat} = \frac{0.622 P_{sat}}{B - P_{sat}} \tag{16}$$

where e_1= -5800.2206, e_2= 1.3914993, e_3= -0.04860239, e_4= -4.1764769105×10^{-5}, e_5= -1.4452093×10^{-8}, e_6= 6.5459673;

P_{sat} is pressure of the saturated state, Pa;

B= 101325 Pa.

In Chapter 3, the experiments have demonstrated that the PIEC can provide cooling under different spraying modes, and the equations used for simulation correspondingly vary as well. In the case of consistent spraying, water is sufficient to ensure full evaporation, and the PIEC can be regarded as a typical IEC. Therefore, the time term in the above formula should be removed. While under the conditions of periodic spraying, evaporation mainly relies on the water retained during the spraying stage, making it a dynamic process that requires consideration of the limited water storage's effect on cooling performance. Therefore, it is necessary to develop a model of the porous area. In addition, the time term should be retained. The specific modeling of the porous area is described as follows:

4.1.2 Porous zone

The total volume of the porous zone consists of solid, liquid, and gas (Eq. (17)). The solid phase refers to the solid material that makes up the porous medium, which provides the structure and framework for the porous medium. The liquid phase refers to the fluid that fills the pores or voids in the porous medium, such as water in this thesis. The gas phase refers to the gas that fills the remaining space in the pores or voids. Porosity is a measure of the void space or empty spaces within a material, usually expressed as a percentage of the total volume of the material. In other words, it represents the amount of empty space in a material that can be occupied by a fluid or gas, which can be defined by Eq. (18).

$$\Delta V_s + \Delta V_l + \Delta V_g = \Delta V \tag{17}$$

$$\varepsilon = \frac{\Delta V_l + \Delta V_g}{\Delta V} \tag{18}$$

where ΔV_s, ΔV_l, ΔV_g are solid phase, liquid phase, and gas phase volume, m^3;

ΔV is total volume, m^3;

ε is porosity.

For the rigid skeleton such as the nickel used in the PIEC prototype, namely the solid phase, it is minimally influenced by the other two phases and other factors. While in the porous region, which is filled with liquid and gas, it is necessary to describe their states in the limited space. The water and gas saturation are two important properties that describe the distribution and amount of fluids within the porous material. Water saturation is the fraction of the pore space volume that is occupied by water, expressed as a percentage of the total pore space volume. In other words, it represents the amount of pore space in a material that is filled with water. Gas saturation, on the other hand, is the fraction of the pore space volume that is occupied by gas, expressed as a percentage of the total pore space volume. It represents the amount of pore space in a material that is filled with gas. The two saturations can be expressed by Eq. (19) and Eq. (20), which also follow the relationship of Eq. (21) [125, 126].

$$S_l = \frac{\Delta V_l}{\Delta V_l + \Delta V_g} = \frac{\Delta V_l}{\varepsilon \Delta V} \tag{19}$$

$$S_g = \frac{\Delta V_g}{\Delta V_l + \Delta V_g} = \frac{\Delta V_g}{\varepsilon \Delta V} \tag{20}$$

$$S_g + S_l = 1 \tag{21}$$

The mass concentrations of each component, namely, the liquid phase and the gas phase, are written from Eq. (22) to Eq. (24) [123].

$$c_l = \rho_l \varepsilon S_l \tag{22}$$

$$c_a = \rho_a \varepsilon S_g \tag{23}$$

$$c_v = \rho_v \varepsilon S_g \tag{24}$$

where c_l, c_a, c_v are the mass concentration of liquid, gas phase of dry air, and gas phase of water vapor, kg/m^3;

ρ_l, ρ_a, ρ_v are the liquid, air, and water vapor density, kg/m^3;

S_l, S_g are liquid and gas saturation.

The densities of air and water vapor follow the relationship as Eq. (25) and Eq. (26), and the moist air density and pressure can accordingly be formulated by Eq. (27) and Eq. (28).

$$\rho_a = \frac{P_a M_a}{RT} \tag{25}$$

$$\rho_v = \frac{P_v M_v}{RT} \tag{26}$$

$$\rho_g = \rho_a + \rho_v \tag{27}$$

$$P_g = P_a + P_v \tag{28}$$

where M_a and M_v are the molar mass of the air and water vapor, kg/mol;

R is the gas constant, J/(mol·K)

T is temperature, K.

Effective thermal conductivity refers to the overall thermal conductivity of a composite material, which takes into account the individual thermal conductivities of each component and their relative proportions or distribution [127]. In this thesis, the porous zone contains three phases (solid matrix, liquid, and gas). Therefore, the effective thermal conductivity and specific heat capacity need to be rewritten and expressed as Eq. (29) and Eq. (30).

$$k_{ef} = k_s(1-\varepsilon) + k_l S_l \varepsilon + k_g S_g \varepsilon \tag{29}$$

$$(\rho C_p)_{ef} = \rho_s C_{ps}(1-\varepsilon) + \rho_l C_{pl} S_l \varepsilon + \rho_g C_{pg} S_g \varepsilon \tag{30}$$

where k_s, k_l, k_g, are thermal conductivity of the solid phase, liquid phase, and gas phase, W/m·K;

C_{ps}, C_{pl}, C_{pg} are specific heat capacity of solid phase, liquid phase, and gas phase, J/(kg·K);

ε is porosity.

In the porous region, the permeability is an essential factor that describes how easily a fluid flows through a porous material [128]. Liquid and gas both have their own permeabilities. The liquid phase permeability depends on the absolute permeability and relative permeability (Eq. (31)). A similar formation is adaptable for gas permeability (Eq. (32)). The absolute permeability can be obtained by the Carman-Kozeny equation shown as Eq. (33), which depends on the porosity and pore diameter [129]. The relative permeabilities of the gas phase and liquid phase are formulated by Eq. (34)-(35) [130, 131].

$$\kappa_l = \kappa \kappa_{rl} \tag{31}$$

$$\kappa_g = \kappa \kappa_{rg} \tag{32}$$

$$\kappa = \frac{d_{por}^2}{180} \cdot \frac{\varepsilon^3}{(1-\varepsilon)^2} \tag{33}$$

where κ, κ_l and κ_g are absolute permeability, liquid phase permeability, and gas phase permeability, m^2;

κ_{rl} and κ_{rg} are relative permeabilities of liquid phase and gas phase.

d_{por} is the characteristic length of the pore space, measured in meters (m)

$$\kappa_{rg} = \begin{cases} 1 - 1.1S_l, & (S_l < \frac{1}{1.1}) \\ 0 \quad , & (S_l > \frac{1}{1.1}) \end{cases} \tag{34}$$

$$\kappa_{rg} = \begin{cases} \kappa_{rl} = \left(\frac{S_l - S_{ir}}{1 - S_{ir}}\right)^3, & (S_l > S_{ir}) \\ 0 \quad , & (S_l < S_{ir}) \end{cases} \tag{35}$$

where S_{ir} is irreducible liquid phase saturation.

As mentioned in assumptions in section 4.1, the liquid water leaves the porous media only in the form of vapor, taking away the latent heat simultaneously. In other words, the increased amount of water content in the secondary air equals the reduced liquid water content from the porous region. Furthermore, the porous structure could lead to capillary action, which is usually regarded as an extra diffusion item in the mass transfer process [123]. Considering the above physical behaviors, the mass transfer equations for water are written as Eq. (36) to Eq. (37). The water diffusion caused by capillary action is determined by the temperature and water vapor content, as expressed in Eq. (38).

$$\frac{\partial c_l}{\partial \tau} + \nabla \boldsymbol{n}_l = -m_{ev} \tag{36}$$

$$\boldsymbol{n}_l = (-\rho_l \frac{\kappa_l}{\mu_l} \nabla P_g)\rho_w - D_{cap} \nabla c_l \tag{37}$$

$$D_{cap} = 1 \times 10^{-6.88+8 \cdot M_{wb}} \tag{38}$$

where the moisture content of wet basis has the relationship as $M_{wb} = \frac{M_{db}}{1+M_{db}}$ and $M_{db} = \frac{\varepsilon S_l \rho_l}{(1-\varepsilon)\rho_s}$, according to the research by Kumar [132].

The mass transfer in the gas phase that includes the air and water vapor can be expressed from Eq. (39) to Eq. (42). It should be emphasized that the gas saturation and porosity influence the diffusivity of the moist air in the porous region, and the effective diffusivity needs to be modified using Eq. (43) [123].

$$\frac{\partial c_v}{\partial \tau} + \nabla \boldsymbol{n}_v = m_{ev} \tag{39}$$

$$\frac{\partial c_a}{\partial \tau} + \nabla \boldsymbol{n}_a = 0 \tag{40}$$

$$\boldsymbol{n}_v = (-\rho_v \frac{\kappa_g}{\mu_g} \nabla P_g) - \frac{{C_s}^2}{\rho_v} M_a M_v D_{ef} \nabla \left(\frac{P_v}{P_g}\right) \tag{41}$$

$$\boldsymbol{n}_a = (-\rho_a \frac{\kappa_g}{\mu_g} \nabla P_g) - \frac{{C_s}^2}{\rho_a} M_a M_v D_{ef} \nabla \left(\frac{P_a}{P_g}\right) \tag{42}$$

$$D_{ef} = D_{va}(S_g \varepsilon)^{\frac{4}{3}} \tag{43}$$

where $\boldsymbol{n}_l$, $\boldsymbol{n}_a$, $\boldsymbol{n}_v$ are mass flux of liquid water, air, and water vapor, kg/m^2;

P_g, P_a, P_v are pressure of gas phase, air, and water vapor, Pa;

ρ_l, ρ_a, ρ_v are the liquid, air, and water vapor density, kg/m^3;

M_a, M_v are molar weight of air and water vapor, kg/mol;

C_s is molar concentration of secondary air, mol/m^3;

D_{va} is diffusion coefficient of the substance, m^2/s;

S_g is saturation of gas phase;

ε is porosity.

When the air passes the secondary air channel and the water spraying is suspended, the process can be regarded as the convective drying for the porous media during the non-spraying period. The stored water evaporates from the porous zone in the form of water vapor, and the water evaporation can be calculated as shown in Eq. (44) [133]. The water activity is obtained from Eq. (45).

$$m_{ev} = K_{ev} \frac{M_v}{RT} (a_w P_{sat} - P_s) S_g \varepsilon \tag{44}$$

$$ln\,(a_w) = -0.0267 exp\,(S_l^{-1.656}) + 0.0107 exp\,(-1.287 S_l) S_l^{1.513}\, ln(P_{sat}) \tag{45}$$

where $\boldsymbol{n_l}$, $\boldsymbol{n_a}$, $\boldsymbol{n_v}$ are mass flux of liquid water, air, and water vapor, kg/m^2;

P_g, P_a, P_v are pressure of gas phase, air, and water vapor, Pa;

K_{ev} is evaporation rate constant;

M_a, M_v are molar weight of air and water vapor, kg/mol;

a_w is water activity;

S_l, S_g *are* saturation of liquid phase and gas phase;

ε is porosity.

Besides, the energy equations for energy balance of the channel and the porous media can be worked out as shown in Eq. (46) and Eq. (47).

$$\frac{\partial\left(\left(\rho c_p\right)_g T\right)}{\partial \tau} + \nabla\left(\left(\rho c_p\right)_g \boldsymbol{u}T\right) = \nabla k_{ef}(\nabla T) \tag{46}$$

$$\frac{\partial\left(\left(\rho c_p\right)_{ef} T\right)}{\partial \tau} + \nabla\left(\boldsymbol{n}_l C_{pl} T + \boldsymbol{n}_g C_{pg} T\right) = \nabla k_{ef}(\nabla T) - m_{ev} h_{fg} \tag{47}$$

where $\boldsymbol{n_l}$, $\boldsymbol{n_a}$, $\boldsymbol{n_v}$ are mass flux of liquid water, air, and water vapor, kg/m^2;

k_{ef} is effective thermal conductivity, W/m·K;

h_{fg} is latent heat of evaporation, J/kg;

m_{ev} is evaporation rate, kg/(m^3·s);

4.1.3 Boundary conditions

Referring to geometric sizes and surface positions, the boundary conditions of this PIEC model can be listed in Table 4.1.1.

Table 4.1.1 Summary of boundary conditions of the PIEC model

Range	Condition

$0 < \tau \leq 3600$	$x = 0; 0 \leq y \leq \frac{d}{2}; 0 \leq z \leq H$	$T_1 = T_{1,in}; C_1 = C_{1,in}; u_1 = u_{1,in}$
	$x = L; 0 \leq y \leq \frac{d}{2}; 0 \leq z \leq H$	$P_{1,out} = P_{1,amb}$
	$0 \leq x \leq L; y = \frac{d}{2}; 0 \leq z \leq H$	$\frac{\partial T_1}{\partial y} = 0; \frac{\partial c_1}{\partial y} = 0; \frac{\partial u_1}{\partial y} = 0; v_1 = w_1 = 0$
	$0 \leq x \leq L; -\frac{d}{2} - \delta \leq y \leq -\delta; z = 0$	$T_2 = T_{2,in}; C_2 = C_{2,in}; w_2 = w_{2,in}$
	$0 \leq x \leq L; -\frac{d}{2} - \delta \leq y \leq -\delta; z = H$	$P_{2,out} = P_{2,amb}$
	$0 \leq x \leq L; y = -\frac{d}{2} - \delta; 0 \leq z \leq H$	$\frac{\partial T_2}{\partial y} = 0; \frac{\partial c_2}{\partial y} = 0; \frac{\partial u_2}{\partial y} = 0; u_2 = v_2 = 0$
$\tau = 0$ (Initial value)	$0 \leq x \leq L; -\frac{d}{2} \leq y \leq \frac{d}{2}; 0 \leq z \leq H$	$T = T_{p,in};$
	$0 \leq x \leq L; 0 \leq y \leq \frac{d}{2}; -\frac{d}{2} \leq y \leq -\delta;$ $0 \leq z \leq H$	$C_p = C_{p,in}; u_p = u_{p,in};$ $C_s = C_{s,in}; w_s = w_{s,in}$
	$0 \leq x \leq L; -\delta \leq y \leq 0; 0 \leq z \leq H$	$-m_{ev} = 0$
	$0 \leq x \leq L; -\delta - \frac{d}{2} \leq y \leq -\delta; 0 \leq z \leq H$	$m_{ev} = 0$

4.1.4 Numerical solutions

In this thesis, the proposed PIEC model was constructed and simulated using the COMSOL Multiphysics software. The main procedures are illustrated as follows. In the first place, the physical PIEC model was established. Subsequently, the heat transfer module, laminar flow module, transport of diluted species module, and some self-defined equations were incorporated according to the aforementioned description. The brief illustration of the three modules is as follows [134]. The heat transfer module is used to describe the heat transfer process in the PIEC, including conductive and convective heat transfer. It provides a comprehensive set of options for modeling heat transfer among different components and materials. The module also involves features to simulate the internal heat sources, temperature-dependent material properties, and phase change. The Laminar Flow Module can be used to simulate the laminar flow of the fluid in the PIEC. The Transport of Diluted Species Module can be employed to model the transport of diluted species in the PIEC, especially in the secondary air channel and the moist porous material in this study. This module accounts for diffusion, convection, and phase change, and provides a set of tools for modeling mass transport, including the diffusion equation, advection-diffusion equation, and Nernst-Planck equation. The module also contains features for simulating chemical reactions, electrochemistry, and transport in porous media. The air velocities in the two channels are time-independent, which solely depend on the inlet setting conditions and are treated as steady status in the calculation process. Thirdly, the boundary conditions and initial values have been summarized in section 2.3 and adapted to the model. Fourthly, the Multifrontal Massively Parallel sparse direct Solver (MUMPS), a powerful built-in solver written in Fortran 90 language for solving large sparse linear systems using direct methods, was employed to calculate the aimed distributions for elements at each time. MUMPS uses a multifrontal method to factorize the matrix and solve the system of equations. This method works by partitioning the matrix into smaller submatrices and performing a factorization on each submatrix [135]. The resulting factorization is then combined to produce the final solution. The calculation results would be illustrated and discussed in section 4.2.

4.1.5 Grid independence monitoring

Grid independence monitoring is a crucial process used in simulations to ensure that the calculation results are not significantly influenced by the size or resolution of the computational grid used in the simulation. It involves running the simulation with different grid sizes or resolutions and comparing the results to determine whether they converge to a consistent solution as the grid is refined [136]. By doing so, the author can identify a reasonable grid unit number that can guarantee the accuracy of the outlet parameters while minimizing the computational load simultaneously. In this study, the dynamic temperature variations in 3600 s were examined by increasing the number of grid units from 1932 to 34570 based on the input parameters presented in Table 4.1.2. As shown in Fig. 4.1.2, the unit number was determined to be 16500 since the maximum difference of primary air outlet temperature was less than 0.3% throughout the simulation period. This indicates that the simulation results were not significantly affected by the grid size or resolution, and thus, the chosen grid unit number was appropriate for both ensuring the accuracy of the outlet parameters and reducing the calculation resource.

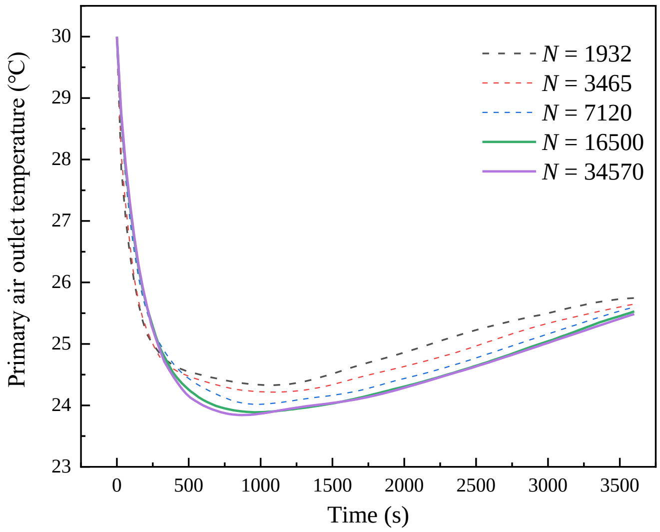

Fig. 4.1.2 Results of the grid independence monitoring

Table 4.1.2 The pre-set values for simulations

Parameter	Value	Parameter	Value

H (mm)	300	L (mm)	400
d (mm)	5	$t_{p,in}$ (°C)	32
d_{por} (um)	120	$RH_{p,in}$	40%
ε (1)	0.9	$t_{s,in}$ (°C) (3)	22.9
h_{fg} (J/kg)	2.5×10^6	$RH_{s,in}$ (3)	69%
D_{va} (m^2/s)	2.6×10^{-5}	v_p (m/s)	2.5
S_{ir} (2)	0.1	v_s (m/s)	3
Total time (s)	3600	Time interval (s)	1

Notes:

(1) The properties of the porous media used in the PIEC prototype were provided by a specialized manufacturer of porous materials.

(2) S_{ir} is the irreducible liquid phase saturation, representing the water trapped in the porous media that is unable to be evaporated. The typical value of S_{ir} is approximately 0.1, as commonly reported in the published literature [126].

(3) The cool indoor exhaust air is introduced to the secondary air channel so that the primary outlet air temperature can be furtherly reduced instead of using the hot outdoor fresh air [54].

4.1.6 Model validation

The dynamic simulation model was substantiated through experimental validation, which was conducted using a PIEC prototype on a well-established test rig in the laboratory. A concise overview of the essential content is provided herein, with the detailed methodology thoroughly elaborated in Chapter 3. As given in Fig. 4.1.3(a), a plate-type cross-flow PIEC prototype was meticulously designed and fabricated for this purpose. The porous nickel layer was sintered on a thin stainless-steel slice together to form a hybrid heat transfer plate. This manufacturing process was executed within a sintering furnace. The raw materials, comprising nickel foam and the stainless-steel plate, were subjected to a sintering temperature of 1250℃ for a duration of 2 hours, in a highly controlled environment featuring high-purity hydrogen (with a purity equal to or greater than 99.999%). The resultant sintered layer is capable of absorbing and retaining liquid water for evaporation, even under non-spraying conditions, and the stainless-steel plate is to avoid the water in the porous structure to contact the primary air channel environment. A small piece of plate surface with the porous nickel structure was captured under the scanning electron microscope (SEM) (Fig. 4.1.3(b)). These small pores are inter-connected so that the liquid water can penetrate, and no closed air chamber is observed.

The selection of nickel for making the porous layer of the hybrid plate is attributed to two primary factors. Firstly, nickel demonstrates superior anti-corrosion properties, particularly when compared to other metals, such as aluminum foil commonly utilized in IECs. Secondly, the sintered porous nickel exhibits commendable durability, which can ensure the porous structure remains intact and preserve its water-absorbing capabilities even after repeated water retention testing.

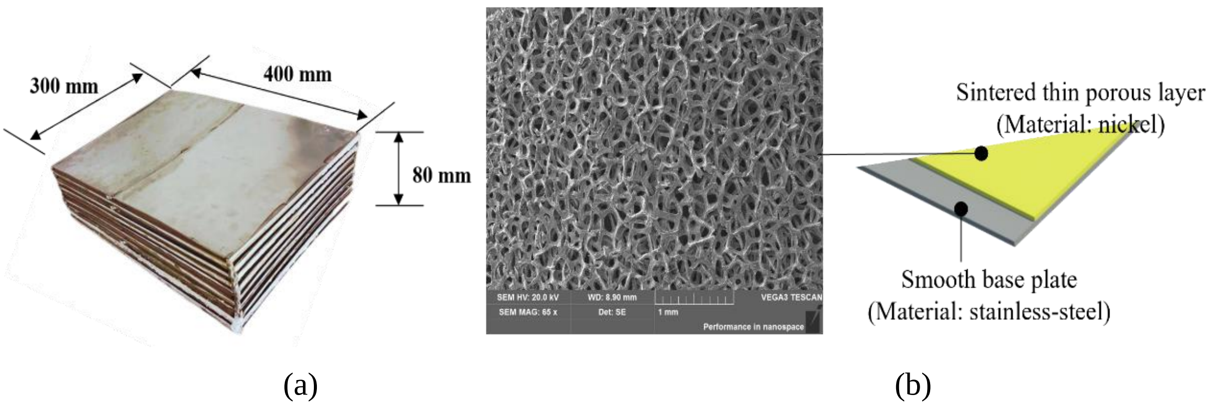

Fig. 4.1.3 (a) Overview of the PIEC prototype (b) Structure of the sintered porous plate and the real photo of the porous surface under SEM

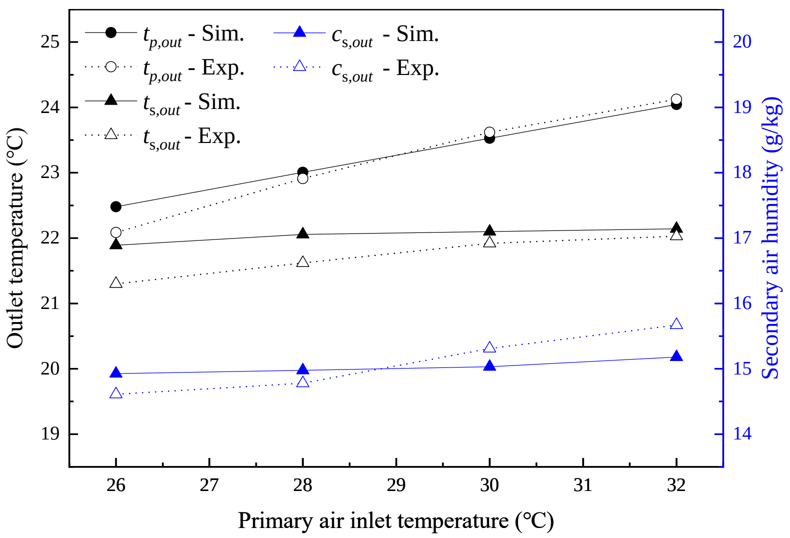

(a) Steady state

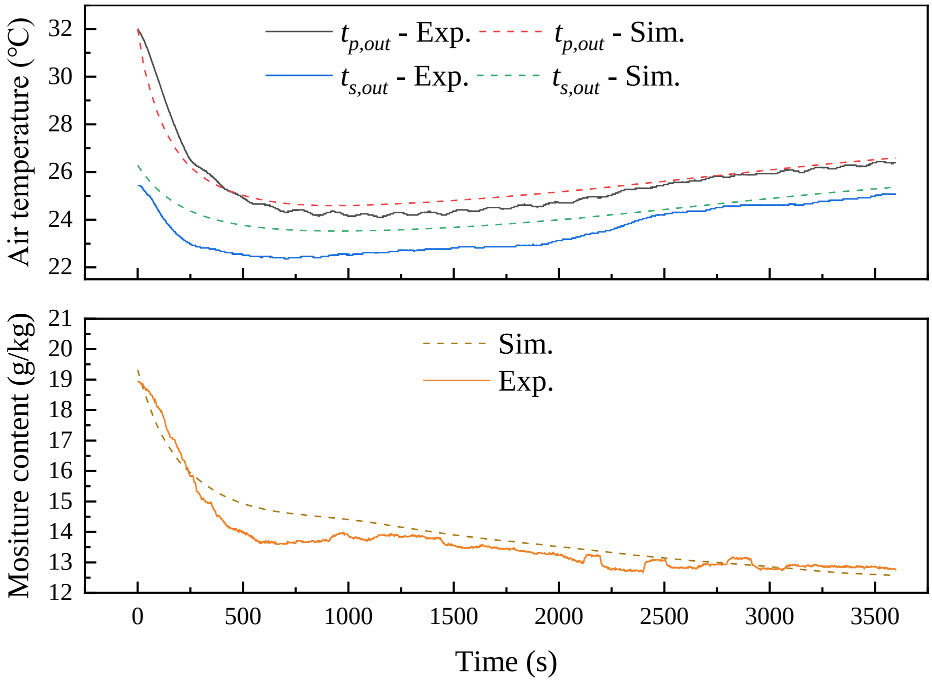

(b) Dynamic state

Fig. 4.1.4 Comparison between simulation results and experimental data

During the experiments, water is sprayed consistently under the steady mode. While the secondary air channels were moisturized sufficiently in advance under the dynamic conditions. Subsequently, the water system was deactivated, while the operation of the fans persisted. Dynamic temperature variations under non-spraying conditions were logged every second, which were recorded in a data logger for a total testing duration of 3600 seconds. Essential parameters for both simulations and experiments are concisely outlined in Table 4.1.2. As shown in Fig. 4.1.4, the simulation results and the data measured from the experiments were compared and examined in good agreement. Under the steady state, the root mean square errors (RMSEs) are 0.21℃, 0.38℃, and 0.34 g/kg for primary air outlet temperature, secondary air outlet temperature, and secondary air outlet humidity, respectively. Under the dynamic state, the RMSEs are 0.41℃, 0.55℃, and 0.39 g/kg, which are deemed acceptable for subsequent parametric analyses.

4.2 Results and discussions

Based on the proposed cross-flow PIEC model, the influences of essential parameters on the cooling performance are evaluated and illustrated in this section. The basic information is given in Table 4.1.2. The ranges of the temperature and velocity are within the normal range, as illustrated in published papers [12, 137].

Table 4.2.1 Summary of the ranges of aimed parameters

Parameter	Value	Parameter	Value
$t_{p,in}$ (℃)	[26, 2, 32]	d (mm)	[4, 1, 8]
v_p (m/s)	[2,0.5,3.5]	ε	[0.8, 0.05, 0.90]
v_s (m/s)	[2,0.5,3.5]		[0.90, 0.01, 0.95]

Notes:

(1) The temperature in K has been transferred in ℃.

(2) $t_{s,in}$= 23℃, $RH_{p,in}$= 30%, $RH_{s,in}$= 70%.

(3) Total simulation duration: 3600 s.

(4) [a, b, c]: starts from a and ends at b with c interval.

The studied porous-related parameter ranges are based on the actual manufacturing condition of the material. In order to make the porous zone have more space to store liquid water, the raw material of the porous layer is required with high porosity, which is usually more than 0.8 based on the existing manufacture craft with different pore diameters [138-140]. Thus, the ranges of input values for variables can be determined as listed in Table 4.2.1. Again, to enhance the air-cooling performance of the PIEC, the return air from the cool indoor area is taken as the secondary air [27, 104], as done in the experimental study.

4.2.1 Temperature and moisture content distributions

Before assessing the influences of such parameters, the temperature and humidity distributions on selected surfaces of two channels are presented in Fig. 4.2.1 and Fig. 4.2.2. The selected surface is parallel to the airflow direction, which can show the variation of the aimed parameters along the channel. Under the steady state, the temperature of the primary air gradually decreases in the flow direction, with a lower temperature near the wall surface, while the humidity remains constant. The temperature of the secondary air initially decreases and subsequently increases in the flow direction, with the humidity continuously increasing. The observed variations in the primary and secondary air within the channel are consistent with previous research findings [12, 40].

Under the dynamic state condition, the air status is given when the PIEC system operates at 1200 s, 2400 s, and 3600 s based on the input conditions in Table 4.1.2. The PIEC is assumed to be wetted so that the minimum temperature can be obtained. In the secondary air channel, the air enters from the bottom and exits at the top side. The flowing air promotes evaporation and takes away the latent heat. It can be observed that the exhaust air temperature increases, but the humidity becomes lower, indicating the lack of water for evaporation and lower latent heat removal. Specifically, the outlet temperature and moisture content are 23.2℃ and 0.0145 kg/kg at 1200 s, while the values become 26.1℃ and 0.0127 kg/kg on average at 3600 s.

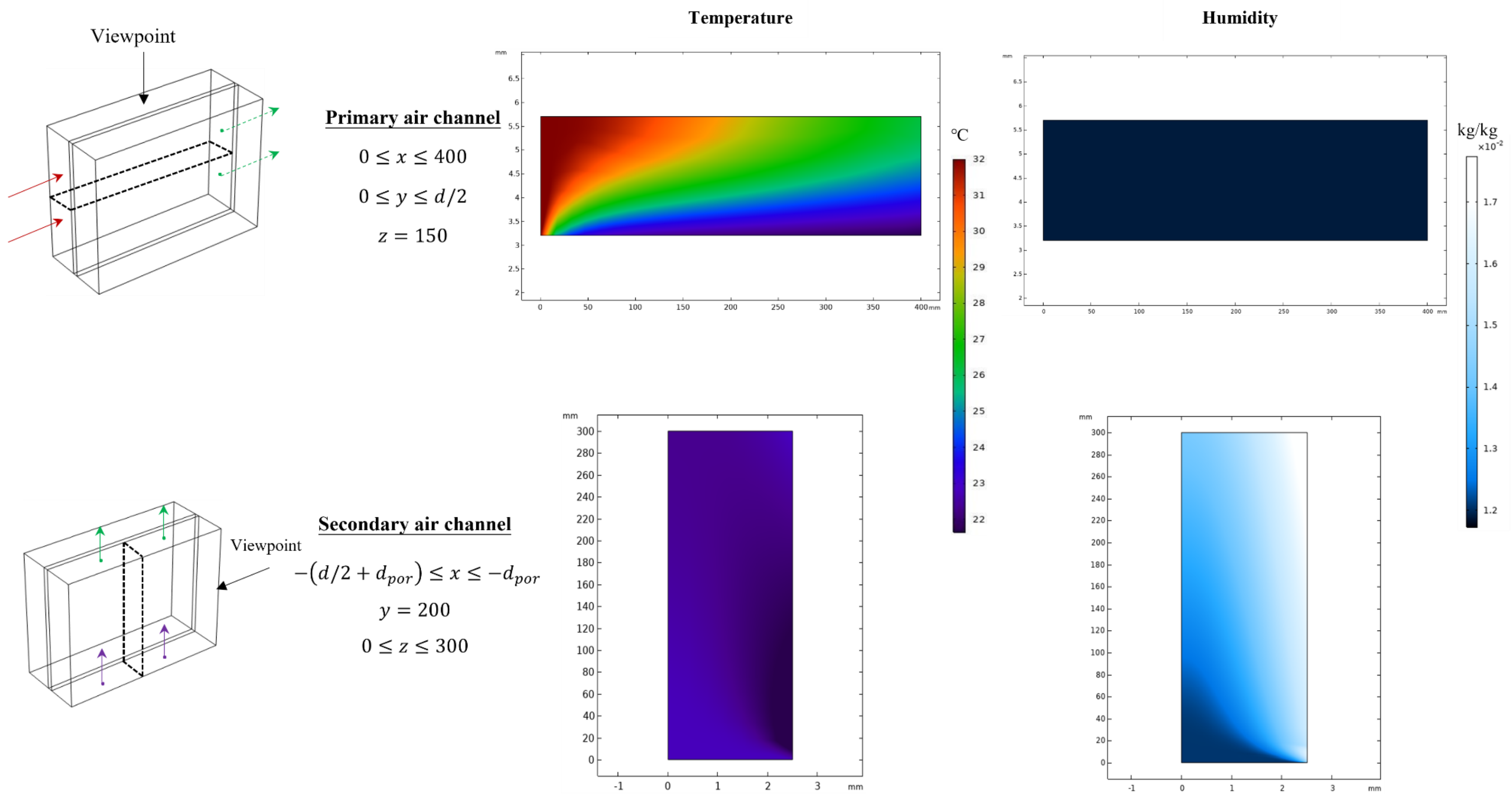

Fig. 4.2.1 Temperature and Temperature and humidity distributions on the selected section under steady state

(Note: The unit of humidity in the secondary air channel is transferred to kg/kg)

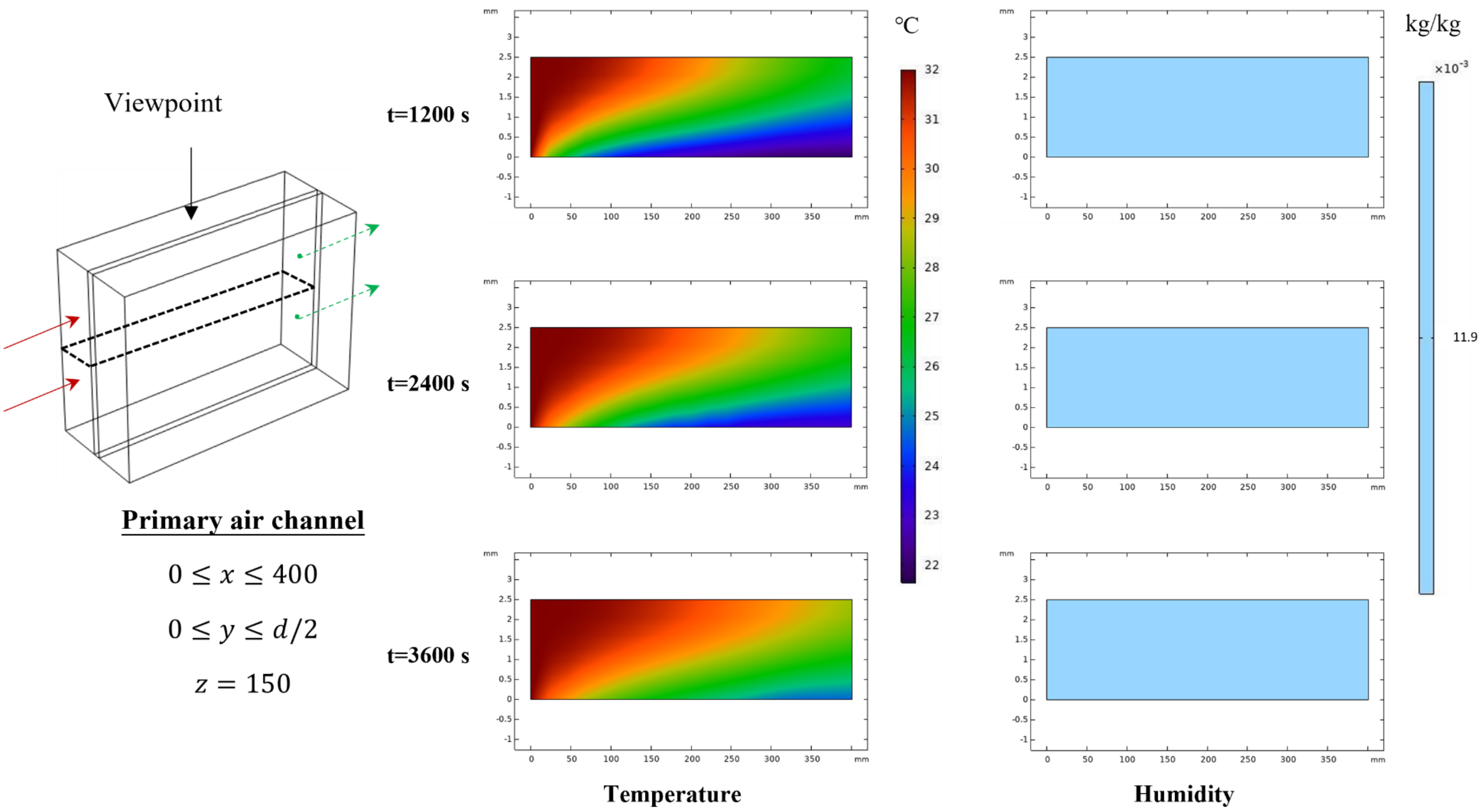

(a) Primary air channel

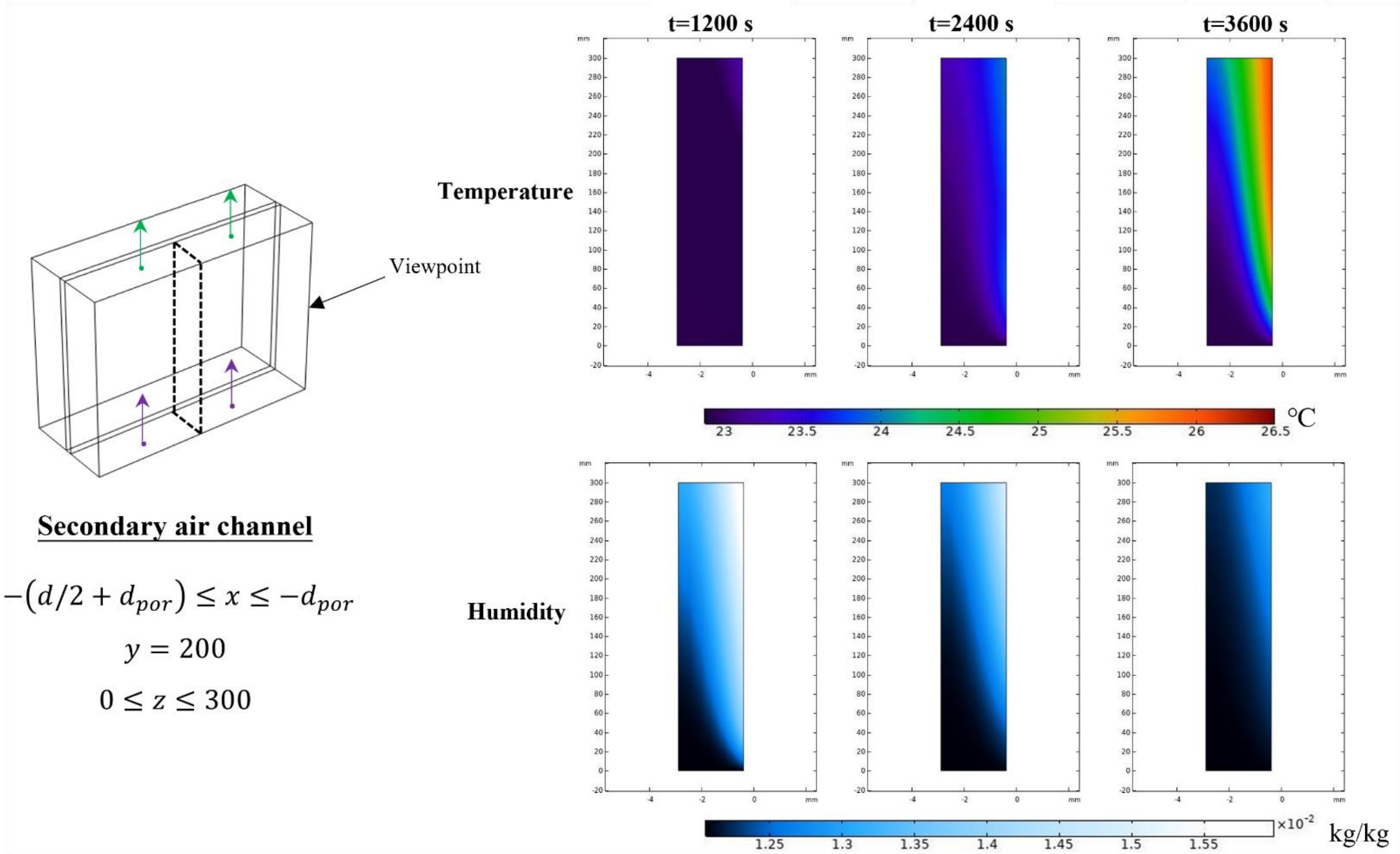

(b) Secondary air channel

Fig. 4.2.2 Temperature and humidity distributions on the selected section at 1200 s, 2400 s, and 3600 s

(Note: The unit of humidity in the secondary air channel is transferred to kg/kg)

In the primary air channel, the airstream enters through the left entrance and exits from the right side, resulting in a temperature drop as the air flows through. The gradual decrease in water content in the porous layer of the secondary air channel surface consequently leads to a reduction in its cooling capacity, which ultimately results in a temperature rise in the primary air channel. As seen from Fig. 4.2.2(a), the outlet temperature of the primary air channel rises from 24.6℃ at 1200 s to 26.5℃ at 3600 s. The moisture content value remains constant at .0119 kg/kg throughout the simulation period because the PIEC primarily deals with sensible cooling, and the mass gradient only occurs in its adjacent channel.

4.2.2 Parametric analysis

4.2.2.1 Effect of primary air temperature

Fig. 4.2.3(a) presents the temperature variation profile of the PIEC system when the inlet air temperature ranges from 26℃ to 32℃ during the 3600 s simulation period. The maximum and final wet-bulb efficiencies are also calculated and shown in Fig. 4.2.3(b). During the simulation duration, the PIEC is fully wetted to reach the lowest temperature that can be obtained, but no respraying is provided. It can be seen that the outlet temperature of the system goes through three distinct stages/phases. In the first stage/phase 1, the outlet temperature rapidly decreases while the slope becomes slower as it approaches the lowest temperature that the PIEC can achieve. Once the lowest temperature is reached, stage 1/phase 1 ends, and stage 2/phase 2 starts. In stage 2, the temperature curve remains flat and stable for a while before slightly increasing when the water content is unable to maintain the current dynamic equilibrium. Following this, the temperature grows more rapidly towards the end, which is considered as stage 3/phase 3. Additionally, the growing temperature leads to the growing slope of curves in stage 2 and stage 3.

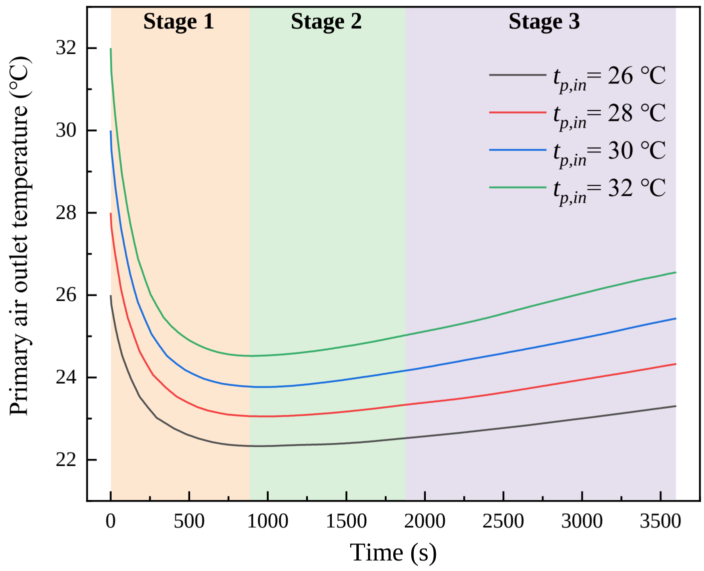

(a) Primary air outlet temperatures

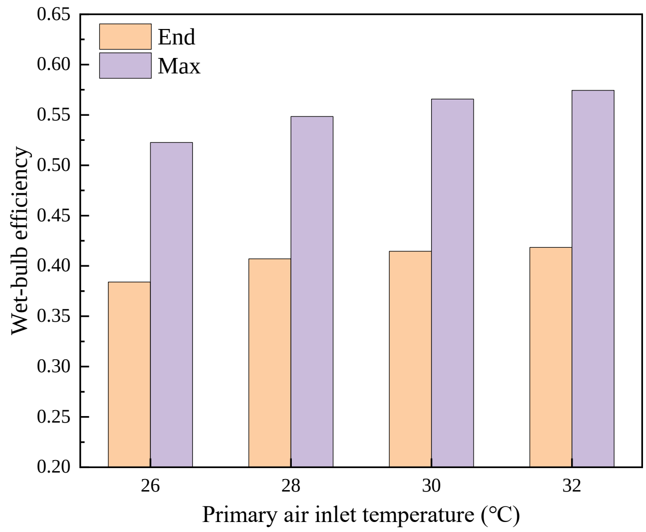

(b) Wet-bulb efficiency

Fig. 4.2.3 (a) Variations of primary air outlet temperatures in 3600 s (b) Maximum and final wet-bulb efficiencies of primary air (The colorful shading in Fig. 4.2.3(a) indicates the stage boundaries when $t_{p,in}$= 32°C.)

Under the steady state, the primary air outlet temperature remains at the lowest temperature, which is the temperature at the end of the first stage in the cases without respraying, and the wet-bulb efficiency stays the same in every case. As shown in Fig. 4.2.3, the wet-bulb efficiency of PIEC increases from 0.52 to 0.57 as the temperature rises from 26℃ to 32℃. Under the dynamic state, the temperature variation process of the 32℃ scenario is presented as an example to illustrate this trend. As shown by the dark green line, the primary air temperature experiences a significant drop within the first 500 s and stops decreasing until it reaches 24.5℃ at 885 s (in the orange shading), corresponding to a wet-bulb efficiency of 0.57, indicating the start of stage 2. Stage 2 lasts from 885 s to 1875 s, during which the temperature grows by 0.5℃ (in the light green shading), while the remaining section in purple represents stage 3. The supply air ultimately reaches 26.6℃, and the wet-bulb efficiency drops from 0.57 to 0.42. The distinct stages/phases observed in the temperature profile highlight the importance of respraying water in the porous layer of the secondary air channel surface to ensure the optimal performance of PIEC. Therefore, the temperature threshold should be set in the simulation to refill the water content in the porous media to maintain the acceptable cooling performance as in chapter 3, which is presented in section 4.2.3.

4.2.2.2 Effect of primary air velocity

The influence of primary air velocity on the dynamic temperature variation process of supply air is depicted in Fig. 4.2.4(a). The whole process can also be divided into three stages. During the first stage, the outlet temperature noticeably decreases but the slope generally becomes flat when before reaching the lowest temperature. Once getting the lowest temperature, stage 1 ends, and stage 2 begins. In the second, the temperature curve stays flat and stable for a while, and then starts to increase when the water content is insufficient to maintain the current cooling capacity. Afterward, the temperature grows with a steeper slope until the end, which is the third stage.

Under the steady state, the primary air outlet temperature stays stable at the lowest temperature, and the wet-bulb efficiency keeps constant in each case. In Fig. 4.2.4, it can be noticed the growing primary air velocity leads to the reduction of wet bulb efficiency, which significantly decreases from 0.63 to 0.48 as the velocity rises from 2 m/s to 3.5 m/s. Under the dynamic state, the temperature variation process of the 3.5 m/s scenario is taken for description. The outlet temperature initially decreases rapidly and then drops gradually to its minimum value within the first 950 s, which marks the completion of stage 1 (in orange). At the same time, phase 2 begins as the temperature remains stable and then gradually increases by 0.5℃ until 1925 s (in light green). The remaining time until the end of the simulation can be identified as stage 3 (in purple). It is noticed that the slower air velocity is beneficial to achieve a greater wet-bulb efficiency, which is consistent with the trend under traditional spraying. As presented in Fig. 4.2.4(b), the highest efficiency of 0.63 is observed in the 2 m/s scenario, while it rapidly decreases to 0.48 when the air velocity is increased to 3.5 m/s. With the limited water content absorbed by the porous media, the final temperatures in the four cases are recorded as 25.8℃, 26.5℃, 27.1℃, and 27.6℃, corresponding to a reduced efficiency of 0.47, 0.42, 0.37, and 0.34. Although the higher primary air velocities can increase the convective heat transfer coefficient, they also result in a larger volume of air being processed, which leads to higher outlet temperatures.

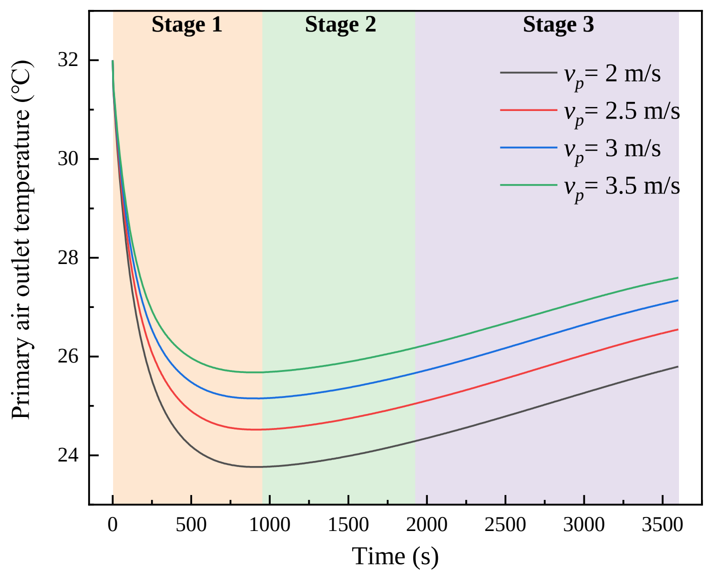

(a) Primary air outlet temperatures

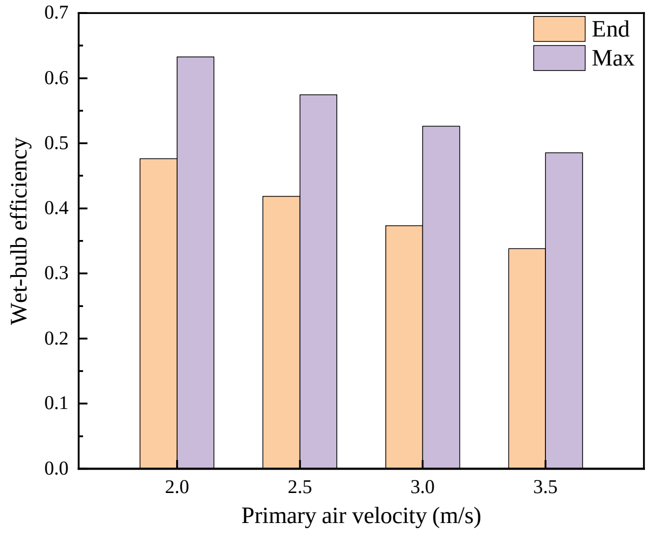

(b) Wet-bulb efficiency

Fig. 4.2.4 (a) Variations of primary air outlet temperatures in 3600 s (b) Maximum and final wet-bulb efficiencies of primary air (The colorful shading in Fig. 4.2.4(a) indicates the stage boundaries when v_p=3.5 m/s.)

4.2.2.3 Effect of secondary air velocity

Fig. 4.2.5 exhibits the variation in outlet temperature within a 3600-second period for different secondary air velocities. During the simulation duration, the PIEC is fully wetted to reach the lowest temperature that can be obtained, but no respraying is provided. The entire timeframe can be segmented into three distinct stages, with the process in each stage resembling that described in the previous section. As illustrated by the case of v_s= 3.5 m/s in Fig. 4.2.5(a), the first stage involves a rapid decrease in air temperature from 32°C to 24.4°C, spanning from 0 seconds to 830 seconds and indicated by the orange shading. Due to the retention of liquid water within the porous structure, a stable temperature period is achieved during phase 2, denoted by the light green shading and occurring between 830 seconds and 1895 seconds. Subsequently, the temperature continues to rise until the conclusion of the experiment, which is indicated by stage 3, shown in purple.

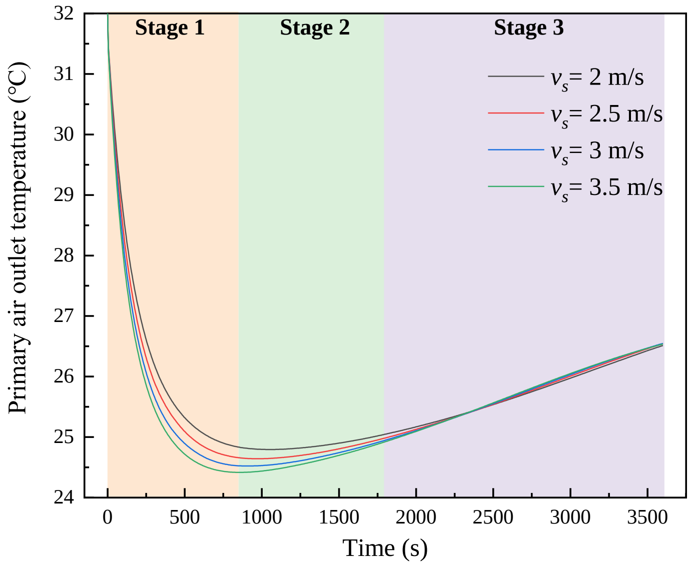

(a) Primary air outlet temperature

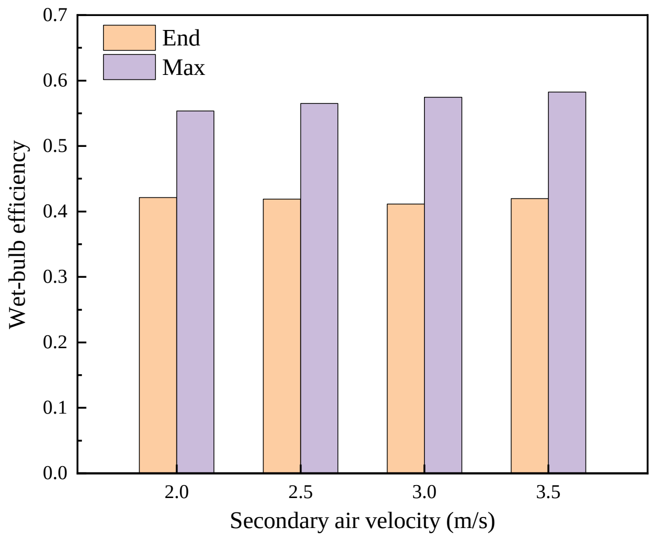

(b) Wet-bulb efficiency

Fig. 4.2.5 (a) Variations of primary air outlet temperature in 3600 s (b) Maximum and final wet-bulb efficiency of primary air (The colorful shading in Fig. 4.2.5(a) indicates the stage boundary of the example when v_s=3.5 m/s.)

4.2.2.4 Effect of channel gap distance

The impact of the channel gap distance on the dynamic outlet supply air temperature profile is illustrated in Fig. 4.2.6(a). The whole process can be categorized into three stages as well. When the channel height is 4 mm, the first stage (in orange) encompasses the entire temperature drop period, which lasts from 0 s to 880 s. Once the lowest temperature of 23℃ is reached, the first stage ends, and the second stage begins, lasting until 1780 s (in light green). This is followed by an increase in outlet air temperature until the end of the simulation, which is recognized as the final stage (in purple). Additionally, it can be noticed that the curve slope is steeper after the second stage when the channel height is narrow, indicating that the faster temperature growth due to the lack of water.

Under the steady state, the wet-bulb efficiency keeps constant in each case. The observed increase in wet-bulb efficiency suggests that the PIEC performance can be enhanced by reducing channel height. As seen in Fig. 4.2.6(b), the highest efficiencies are achieved at the beginning of the second stage, with values of 0.69 and 0.37 observed for the cases with channel heights of 4 mm and 8 mm. However, under the dynamic state, the temperature changes due to the limited water in the porous zone, final efficiencies of the PIEC drop to 0.51 and 0.28, respectively. Overall, a narrower channel contains less air volume, and the narrower channel results in a higher Reynolds number compared to the high channel with the same channel air velocity, which leads to a larger Nusselt number and therefore better heat transfer performance.

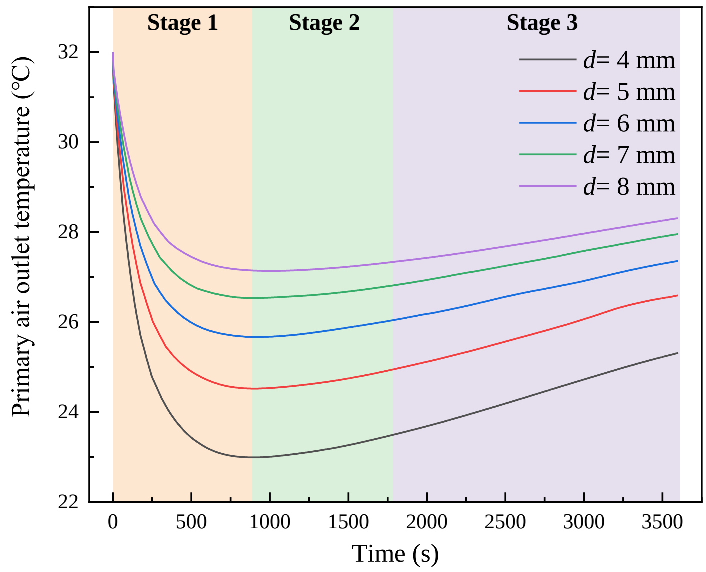

(a) Primary air outlet temperature

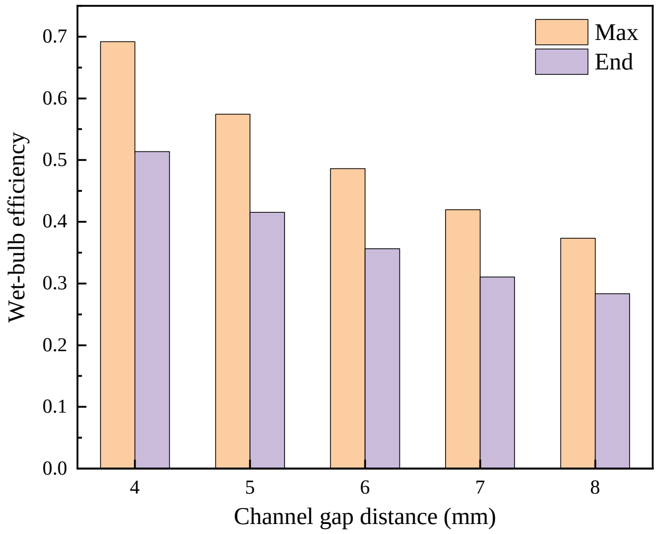

(b) Wet-bulb efficiency

Fig. 4.2.6 (a) Variations of primary air outlet temperatures in 3600 s (b) Maximum and final wet-bulb efficiencies of primary air (The colorful shading in Fig. 4.2.6(a) indicates the stage boundary of the example when *d*=4 mm.)

4.2.2.5 Effect of porosity

Fig. 4.2.7(a) exhibits the dynamic primary air outlet temperature variation of the PIEC for different porosity values over the 3600 s simulation period. As the porosity value is 0.95, the temperature starts to decrease from 32℃ within the first 1370 s, marking as the first stage (in the orange area). Once the air reaches the minimum temperature of 24.3℃ in this scenario, the second stage begins and lasts until 2220 s (in the light green area), followed by the rest of 1360 s in purple, classified as the third stage.

Under the steady state, due to the fact that water can sustain sufficient evaporation, the porous medium affects only the heat conduction process under steady-state conditions. Furthermore, owing to the small thickness of the composite heat exchange plate, the impact of heat conduction is negligible. Consequently, the variation in porosity can be disregarded for wet bulb efficiency. Under the dynamic state, it can be realized that the higher porosity leads to better wet-bulb efficiency. However, as the porosity value exceeds 0.9, the effect on the efficiency becomes less pronounced. Fig. 4.2.7(b) illustrates the trend of wet-bulb efficiency, with the maximum values increasing noticeably from 0.49 to 0.58 at the end of the first stage when the porosity is increased from 0.8 to 0.9. However, when the porosity continues increasing to 0.95, the improvement in efficiency is only slight, with the maximum efficiency increasing from 0.58 to 0.59. The reduction in temperature becomes less significant at around 24.3°C, which represents the lowest achievable temperature under the given operating condition. It should also be noted that the higher porosity case takes longer to reach the lowest temperature than the lower porosity case when the inlet temperature decreases. This can be attributed to the fact that the initial condition assumes a single air inlet temperature for the entire PIEC, and the higher water content in the high porosity case possesses more thermal energy that requires a longer time to cool down. In summary, a higher porosity can enhance the evaporation rate, as evidenced by Eq. (44), leading to a gradual reduction of outlet temperature and an increase of wet-bulb efficiency as porosity increases. Therefore, the high porosity is recommended in the PIEC because of the larger water storage volume and enhanced evaporation process.

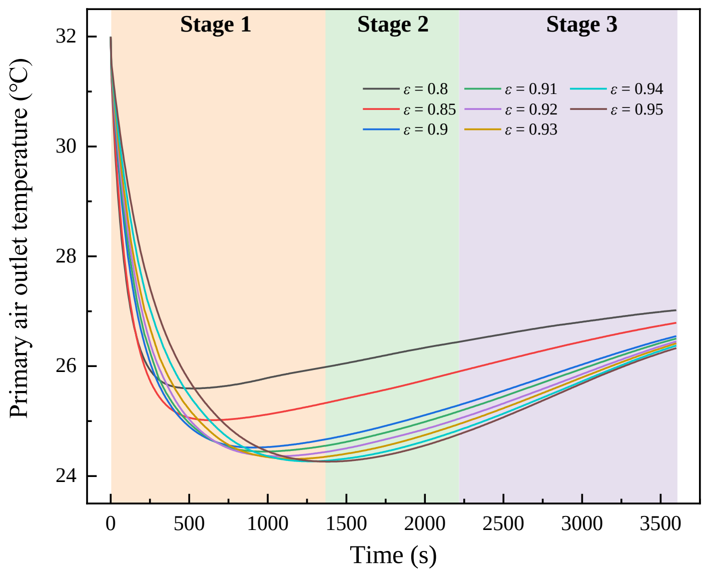

(a) Primary air outlet temperature

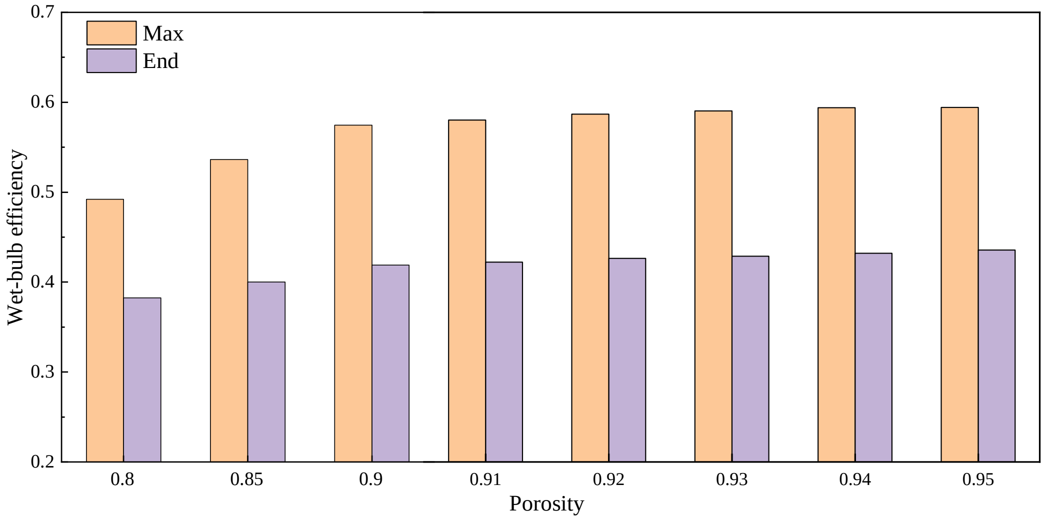

(b) Wet-bulb efficiency

Fig. 4.2.7 (a) Variations of primary air outlet temperature in 3600 s (b) Maximum and final wet-bulb efficiency of primary air (The colorful shading in Fig. 4.2.7(a) indicates the stage boundary of the example when ε =0.95.)

4.2.3 Temperature variations in several cycles

As validated from the experimental studies in Chapter 3, the porous layer on the secondary channel that can store liquid water, allowing this novel air conditioning device to continue cooling the air for a period of time even when the spraying water system is not operating. From the previous sections, it has been known that the primary air outlet temperature of the wetted PIEC increases slowly after reaching the lowest temperature when the water system is out of operation. This feature enables the intermittent spraying plan to replace the traditional consistent spraying scheme that is always required in the normal IEC, improving the overall *COP* and reducing the water consumption of the system. A temperature fluctuation of 0.5℃ is chosen as the threshold to work out the duration of the cycle and non-spraying interval in different cases. In other words, if the temperature variation exceeds 0.5℃, the water spraying should be conducted again to replenish the water in the secondary channel porous layer for 120 s. Again, there are mainly two reasons for using 0.5℃ as the temperature rise threshold. Firstly, the threshold of 0.5℃ is selected as an acceptable temperature fluctuation range for an AC system. Secondly, it can avoid frequent switching of the water system between the on/off status. The spraying time of 120 s is determined from repeated lab tests, which is sufficient to remoisturize the porous zone in secondary air channels of the PIEC.

Table 4.2.2 Specifications and studied parameters of PIEC

Variables	$t_{p,in}$ (℃)	v_p (m/s)	v_s (m/s)	$t_{s,in}$ (℃)	$RH_{p,in}$ (%)	$RH_{s,in}$ (%)
$t_{p,in}$ (℃)	[26, 2, 32]	2.5	3	23	30	70
v_p (m/s)	32	[2, 0.5, 3.5]	3			
v_s (m/s)	32	2.5	[2, 0.5, 3.5]			
PIEC specifications: H=300 mm; L=400 mm; d=5 mm; ε=0.9; d_{por} =120 um						

Using the rule of 0.5℃ temperature rise, the operation strategy for the intermittent spraying plan can be determined for each case. Table 4.2.2 lists the studied air property ranges and specifications of the PIEC. The dynamic variations of primary air outlet temperature with different primary air inlet temperatures and channel velocities in periodic spraying modes in 6000-second simulation duration are depicted in Fig. 4.2.8(a)-(c). It is observed that higher inlet air temperatures and larger channel air velocities lead to more cycles and shorter intervals for non-spraying spans. The reasons are disclosed as follows. A higher primary air inlet temperature can result in elevated water temperatures within the porous medium, thereby enlarging the difference between secondary air and saturated air at the surface of the moist porous medium. The faster primary air velocity can not only intensify convection but also improve the average temperature within the channel as compared to low air velocities cases. This also leads to an expanded gradient between secondary air and saturated air at the surface of the moist porous medium. While enhancing the secondary air velocity directly can accelerate the convective heat and mass transfer, which thereby expedites the evaporation process.

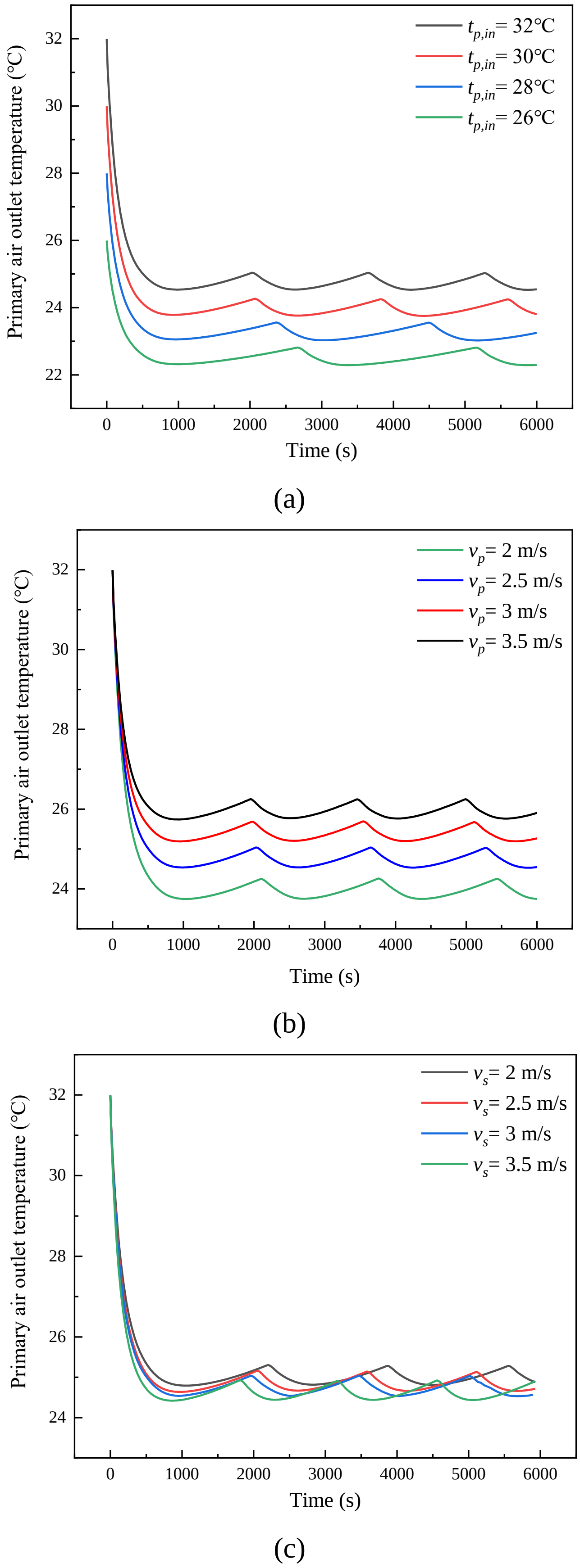

Fig. 4.2.8 Effects of (a) Primary air inlet temperature (b) Primary air velocity and (c) Secondary air velocity on the temperature variation cycles with intermittent spraying

Specifically, the non-spraying duration substantially decreases from 2410 s to 1490 s with an increase in primary air inlet temperature from 26℃ to 32℃. In terms of the intervals with varied primary air velocity, it is identified as 1530 s given a 2 m/s airflow after the moisturizing process. Nonetheless, the time needs to be significantly shortened to 1390 s if the velocity is accelerated to 3.5 m/s. Regarding the durations with different secondary air velocities, a time break of 1510 s can be employed for the spraying water system when the airspeed is 2 m/s, while it needs to be reduced to 1270 s if given a 3.5 m/s airflow. Overall, the intermittent spraying plan can significantly reduce the operation time of the spraying water system at the cost of tiny temperature fluctuations, which offers an effective alternative to the traditional consistent spraying scheme.

4.3 Summary

This chapter describes a novel cross-flow indirect evaporative cooler with porous media on the secondary channel surface (PIEC) with different spraying modes. The primary objective is to dynamically predict the cooling performance of the proposed PIEC. To achieve this, a three-dimensional (3-D) PIEC model is established, and its validity is confirmed through experimental results obtained from a prototype. Owing to the water storage capability of the porous structure, the PIEC system can cool air and maintain a stable temperature drop during a period even when the water system is paused, thus proving the feasibility of the intermittent spraying strategy. Fresh outdoor air is introduced to the primary air channels while cold indoor air is directed to the secondary air channels for enhanced cooling. The effects of essential parameters on the performance of PIEC are analyzed, and comparisons between the conventional and intermittent spraying modes are conducted. The main conclusions can be drawn as follows:

1) The dynamic variation process can be categorized into three stages, and the maximum

wet-bulb efficiency happens at the end of stage 1. The better wet-bulb efficiency results from the higher primary inlet air temperature, greater secondary air velocity, and less primary air velocity. Narrowing down channel height and using the material with larger porosity are also conducive to improving the wet-bulb efficiency.

2) Considering the PIEC specifications, the periodic spraying strategies are determined based on the duration of a cycle with fluctuations within 0.5℃. A 120-second spraying period is conducted at the beginning of each cycle to replenish liquid water, while the remaining time serves as an interval for the non-spraying period. Within the studied ranges, higher primary inlet air temperature and faster velocities in the two channels significantly reduce the interval.

3) The longest and shortest non-spraying intervals are found to be 2410 seconds and 1270 seconds, respectively. These values correspond to 95.2% and 91.4% reduction in water pump working time compared to the conventional continuous water spraying mode. With little temperature fluctuations, the intermittent spraying plan offers an efficient and effective alternative to the traditional consistent spraying.

Chapter 5 Regression models and optimization of the PIEC

The 3-D CFD model developed in the previous chapter offers reliable accuracy in predicting the performance of the indirect evaporative cooler with porous material on the secondary air channel surface (PIEC) system. However, the established model requires a high level of computing configurations and consumes significant computational resources, making it impractical for use in the real engineering applications. Therefore, it is necessary to develop a more straightforward approach to forecasting the PIEC performance can facilitate the possible and convenient usage in reality.

In this chapter, the regression models based on response surface methodology (RSM) are proposed, using data obtained from the previous chapters to provide a simplified method for forecasting system performance. The regression models were developed for this novel heat exchanger under the consistent spraying and periodic spraying mode. The analysis of variance (ANOVA) was carried out to investigate the impact of individual and interactive terms on the response variables - primary air temperature drop, wet-bulb efficiency, and coefficient of performance (*COP*) - under the two spraying conditions. Furthermore, the multi-objective optimizations of the operating parameters of the PIEC system were conducted using the desirability function approach. This approach considers multiple objectives simultaneously, aiming to maximize the primary air temperature drop, wet-bulb efficiency, and *COP* of the PIEC system under the two spraying conditions. The optimal design parameters for the system were identified through this optimization approach.

This chapter is written based on an ongoing manuscript of this thesis author. The paper is titled “*Performance prediction and optimization of cross-flow indirect evaporative cooler by regression model based on response surface methodology*”, which has been submitted to *Energy*.

5.1 Response surface methodology

Response surface methodology (RSM) is a statistical technique used to model and analyze the relationship among multiple variables and a response of interest, which is commonly used in experimental design and optimization. In the RSM, a mathematical function or surface is constructed to represent the relationship between the input factors and the response variable. This surface is used to predict the response variable for any combination of input variables within the range of the data used to construct the surface. Through the implementation of systematically designed experiments and analysis of data, the RSM seeks to relate a response to the levels of several input parameters that influence it. The data of response variables can be obtained from the physical experiments and validated simulation models [141]. RSM uses multiple quadratic terms to fit the functional relationship between factors and the response in many events. The form can be expressed by Eq. (48).

$$y = b_0 + \sum_{a=1}^{n} \beta_a f_a + \sum_{a=1}^{n} \sum_{a<b}^{n} \beta_{ab} f_a f_b + \sum_{a=1}^{n} \beta_{aa} f_a^2 + c_0 \tag{48}$$

where: y is aimed response;

f_a, f_b are input parameters;

N is the number of parameters (5 in this thesis);

b_0 is intercept coefficient;

β_a, β_{ab}, and β_{aa} are coefficients of the linear, interactive, and quadratic item;

c_0 is experiment errors [64].

The main procedures of RSM for this research are summarized as follows:

1) Planning the Experiment: Determine the factors that influence the response and define their range. Select an experimental design suitable (e.g., Central Composite Design, Box-Behnken Design, or Fractional Factorial Design) to explore the relationships between input factors and output response with a limited number of experiments.

2) Conducting the Experiment: Perform the experiment as per the designed plan, where each run is conducted with different combinations of input factors, and the results of the responses are recorded.

3) Developing the Model: Fit the mathematical model to the experimental data using multiple regression or other approaches. The model represents the relationship between factors and responses in the form of a polynomial equation.

4) Model Evaluation: Examine the quality of the fitted model by analyzing the residuals, testing assumptions (e.g., normality, homoscedasticity), and calculating goodness-of-fit measures (e.g., R-squared, adjusted R-squared).

5) Optimization and Analysis: Use the model to identify the optimal factors' settings that maximize or minimize the response, depending on the aimed objectives. The sensitivity analysis can be conducted to understand the relative importance of each factor and their interactions. The effect of single and interactive terms on the response can be analyzed as well.

5.2 Model development

In accordance with the procedures of RSM procedures, the input factors and output responses should be determined. In this study, five factors, namely primary air inlet temperature ($t_{p,in}$), primary air velocity (v_p), secondary air temperature ($t_{s,in}$), secondary air relative humidity ($RH_{s,in}$), and secondary air velocity (v_s) are the input factors. The output responses under both two spraying conditions are wet-bulb efficiency (η_{wb}), outlet temperature ($t_{p,o}$), and *COP*.

After choosing the factors and responses, the Box-Behnken Design (BBD) is employed to design the experiments, which is based on the 2-level factorial designs improved with center and axial points for fitting quadratic models [64]. In this approach, a matrix is constructed with a combination of low, high, and center points for each factor. The center points are included to estimate the error and check the adequacy of the model. The BBD matrix is designed such that each factor is varied at three levels: low, middle, and high. The low and high levels are chosen based on the range of values that the factor can take, while the middle level is typically the average of the low and high levels. The parameters in the three levels of this thesis are listed in Table 5.2.1.

Table 5.2.1 The parameters, ranges, and corresponding levels in the BBD

Name	Unit	Type	Low	Medium	High
primary air inlet temperature ($t_{p,in}$)	℃	Numeric	24	28	32
primary air velocity (v_p)	m/s	Numeric	1.5	2.5	3.5
secondary air temperature ($t_{s,in}$)	℃	Numeric	24	25	26
secondary air relative humidity ($RH_{s,in}$)	%	Numeric	0.4	0.5	0.6
secondary air velocity (v_s)	m/s	Numeric	0.5	1	1.5

The BBD matrix is constructed using a set of mathematical equations that determine the allocation of experimental runs to each factor level. The number of runs required for the BBD matrix is determined by the number of factors, and the resulting design is typically a balanced and orthogonal set of events. The complete BBD matrix can be found in Appendix 1. The responses are calculated based on the validated simulation model in Chapter 4. Then, the analysis of variance (ANOVA) is carried out for the model of the selected responses. ANOVA is a statistical method used to test the null hypothesis that there is no difference in means between two or more groups, which calculates the variability within each group and the variability between the groups to determine whether the differences observed are due to chance or to actual differences in the population means. The significance is evaluated by comparing the p-value with an upper bound of 0.05. The factor that has a p-value lower than 0.05 is regarded as significance, while the items with p-values higher than 0.05 are considered insignificant [35].

5.3 Results and discussion

5.3.1 Regression analysis

The 43 events in the BBD matrix are calculated based on the established 3-D PIEC model. Then, the ANOVA is conducted for the three responses under consistent and periodic spraying modes. The quality and significance of the response variables were evaluated using several statistical metrics, including the p-value, coefficient of determination (R^2), adjusted R^2, predicted R^2, and adequate precision. The p-value measures the significance of the regression coefficients. A p-value less than 0.05 indicates that the coefficient is significant at a 95% confidence level [142]. The R^2, measures the proportion of the variance in the response variable that is explained by the regression model. The R^2 value of 1 indicates a perfect fit of the model to the data [143]. The adjusted R^2 is a modified format of R^2 that accounts for the number of variables in the model. It penalizes the inclusion of additional variables that do not substantially improve the fit of the model [144]. The predicted R^2 measures the proportion of variance in the response variable that is predicted by the model. It is used to evaluate the model's ability to predict the response variable for new observations [144]. The adequate precision measures the signal-to-noise ratio of the model. It compares the range of the predicted response values to the average prediction error [145]. An adequate precision value greater than 4 indicates that the model is suitable to predict the response variable.

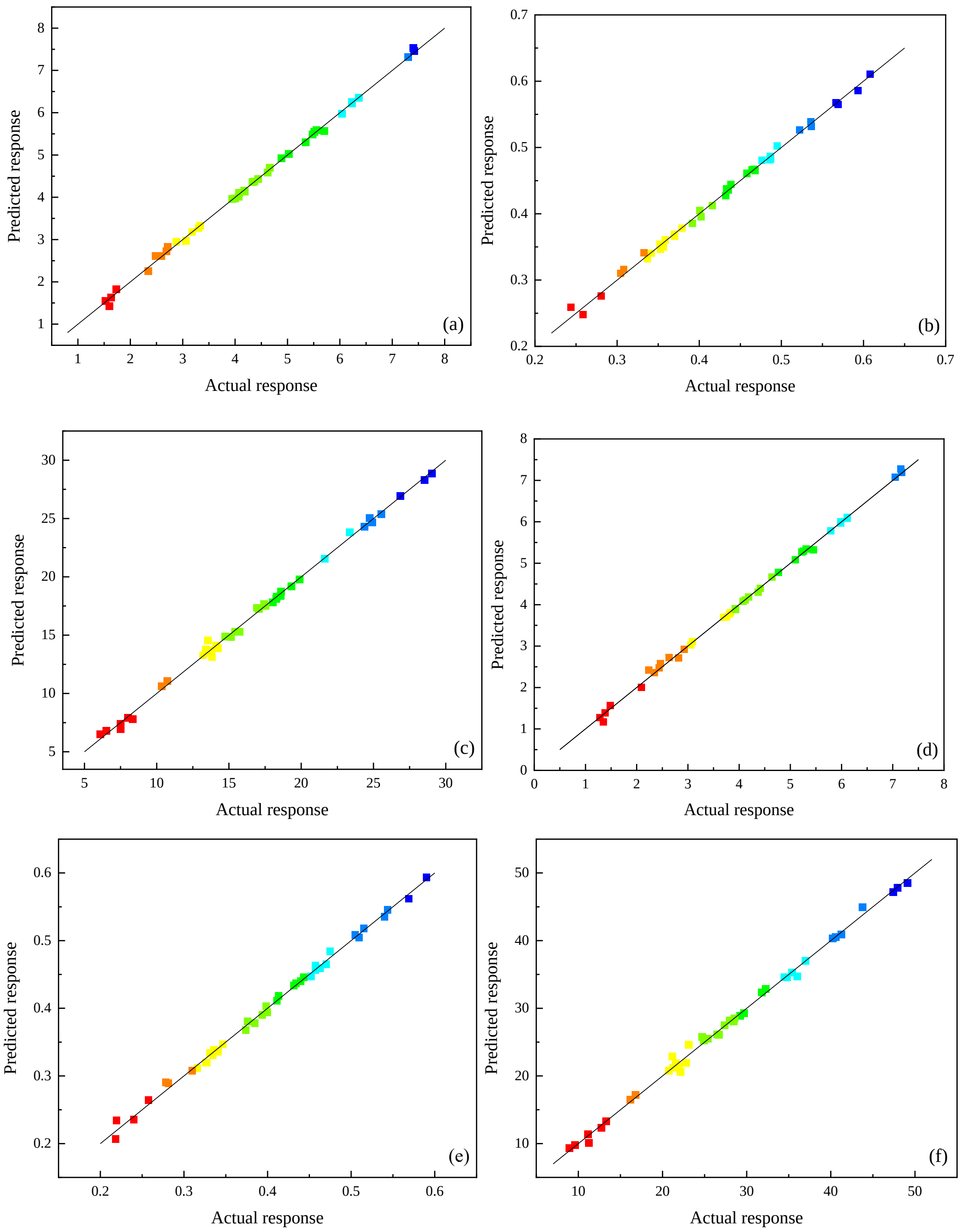

Fig. 5.3.1 Comparison between the predicted results and the actual values of (a) $\Delta t_{p,con}$ (b) $\eta_{wb,con}$ (c) COP_{con} (d) $\Delta t_{p,int}$ (e) $\eta_{wb,int}$ (f) COP_{int}

As shown in Table 5.3.1, all responses in the quadratic form are significant as their p-value are tiny and lower than 0.05. The values of R^2 are greatly close to 1, which means that the quality of fitting is satisfactory. The comparisons between the actual and predicted responses are shown in Fig. 5.3.1, and the plotted points locate around the line segment with a slope of 1, echoing the results of R^2. Besides, the adequate precision and the difference between the adjusted R^2 and predicted R^2 were assessed. The adequate precisions were all substantially larger than 4, indicating that the model is reliable for predicting the response. The difference between the adjusted R^2 and predicted R^2 for each response is much less than 0.2, which meets the modeling requirements and indicates that the model is well-suited to predicting the responses [146].

Table 5.3.1 Fit statistics results of the selected responses

Response	Source	p-value	R^2	Adj.R^2	Pred.R^2	Adj.R^2 - Pred.R^2	Adequate precision
$\Delta t_{p,con}$	Quadratic	<0.0001	0.9986	0.9980	0.9955	0.0025	171.63
$\eta_{wb,\ con}$	Quadratic	<0.0001	0.9965	0.9937	0.9859	0.0078	78.88
COP_{con}	Quadratic	<0.0001	0.9982	0.9968	0.9928	0.004	102.17
$\Delta t_{p,int}$	Quadratic	<0.0001	0.9980	0.9964	0.9919	0.0045	97.39
η_{wb_int}	Quadratic	<0.0001	0.9962	0.9932	0.9849	0.0083	77.43
COP_{int}	Quadratic	<0.0001	0.9962	0.9932	0.9846	0.0086	69.56

The results of the five output responses are reported from the perspectives of the regression model, perturbation plot, and the response surface. The regression model is obtained after conducting the ANOVA, and the effect of a single input factor on the tendency and sensitivity can be summarized from the perturbation plot. Then, the response surface is presented to reveal the influence of the interactive factors that can be artificially influenced, namely primary air velocity, secondary air velocity, and secondary air inlet temperature for this thesis. Thus, there are three pairs of interactive terms for the three factors (v_p-v_s, v_p-$t_{s,in}$, v_s-$t_{s,in}$). Akaike's Information Criterion (AIC), which can seek for the model that can interpret data but the least number of free parameters, is employed for model correction. Therefore, the unqualified pairs need to be removed. This chapter only discusses the interactive factor pairs that meet the criterion. Besides, if the p-value of a term is greater than 0.05, this term is excluded as well. Because the PIEC can operate under consistent and periodic spraying conditions, the regression models of primary air temperature drop, wet-bulb efficiency, and *COP* are obtained for the two spraying modes, while the regression model only exists in the periodic spraying mode.

5.3.2 Response of primary air temperature drop

The results of ANOVA for the response of primary air temperature drop under two spraying modes are presented in Table 5.3.2 and Table 5.3.3, which contains the five input factors, their interactive and square terms. Under the consistent spraying mode, as listed in Table 5.3.2, the total sum of squares is 124.93, with 124.75 of it explained by the model. The lack of fit part has a contribution of 0.1797, with 27 degrees of freedom, while the pure error part has a contribution of 0.0000, with 5 degrees of freedom. The lack of fit part and pure error part have small contributions to the total sum of squares, indicating a good fit of the model to the data. Regarding the source, all the linear terms, five out of ten interactive terms, and three out of five square terms pass the AIC. However, the t_p^2 still needs to be removed from the regression model because its p-value is greater than 0.05. Therefore, the regression model of the primary air temperature drop can be written as Eq. (49) when the PIEC operates under the consistent spraying mode.

Under the periodic spraying conditions, as listed in Table 5.3.3, all related terms are also examined based on the same criteria. Five linear terms, five interactive terms, and two square terms are qualified as they meet the AIC and p-value requirements. Therefore, the regression model of the response is formulated by Eq. (50).

$$\Delta t_{p,con} = 7.02122 + 0.75523t_{p,in} - 1.94372v_p - 0.765062t_{s,in} - 6.93711RH_{s,in} + 0.845788v_s - 0.121298t_{p,in}v_p + 0.138158t_{p,in}v_s + 0.112169v_pt_{s,in} + 1.18086v_pRH_{s,in} - 1.97477RH_{s,in}v_s + 0.191412v_p^2 - 1.17165v_s \quad (49)$$

$$\Delta t_{p,int} = 6.77122 + 0.75523t_{p,in} - 1.94372v_p - 0.765062t_{s,in} + -6.93711RH_{s,in} + 0.845788v_s - 0.121298t_{p,in}v_p + 0.138158t_{p,in}v_s + 0.112169v_pt_{s,in} + 1.18086v_pRH_{s,in} - 1.97477RH_{s,in}v_s + 0.191412v_p^2 - 1.17165v_s^2 \quad (50)$$

Table 5.3.2 ANOVA for the response of primary air temperature drop (consistent spraying mode)

Source	Sum of Squares	df	Mean Square	F-value	p-value	
Model	124.75	13	9.60	1709.29	< 0.0001	++
A - $t_{p,in}$	89.16	1	89.16	15880.90	< 0.0001	++
B - v_p	15.63	1	15.63	2783.83	< 0.0001	++
C - $t_{s,in}$	3.76	1	3.76	669.38	< 0.0001	++
D - $RH_{s,in}$	5.68	1	5.68	1012.26	< 0.0001	++
E - v_s	7.66	1	7.66	1363.79	< 0.0001	++
AB	0.9416	1	0.9416	167.73	< 0.0001	++
AE	0.3054	1	0.3054	54.40	< 0.0001	++
BC	0.0503	1	0.0503	8.96	0.0053	+
BD	0.0558	1	0.0558	9.94	0.0035	+

DE	0.0390	1	0.0390	6.95	0.0128	+
A^2	0.0212	1	0.0212	3.77	0.0609	-
B^2	0.3936	1	0.3936	70.12	< 0.0001	++
E^2	0.8013	1	0.8013	142.72	< 0.0001	++
Residual	0.1797	32	0.0056			
Lack of Fit	0.1797	27	0.0067			
Pure Error	0.0000	5	0.0000			
Cor Total	124.93	45				

Note: ++ means extremely significant (p-value<0.001); + means significant (0.001<p-value<0.05) and - means insignificant (p-value>0.05)

Table 5.3.3 ANOVA for the response of primary air temperature drop (periodic spraying mode)

Source	**Sum of Squares**	**df**	**Mean Square**	**F-value**	**p-value**	
Model	124.73	12	10.39	1707.92	< 0.0001	++
A - $t_{p,in}$	89.16	1	89.16	14650.03	< 0.0001	++
B - v_p	15.63	1	15.63	2568.06	< 0.0001	++
C - $t_{s,in}$	3.76	1	3.76	617.50	< 0.0001	++
D - $RH_{s,in}$	5.68	1	5.68	933.80	< 0.0001	++
E - v_s	7.66	1	7.66	1258.08	< 0.0001	++
AB	0.9416	1	0.9416	154.73	< 0.0001	++
AE	0.3054	1	0.3054	50.18	< 0.0001	++
BC	0.0503	1	0.0503	8.27	0.0070	+
BD	0.0558	1	0.0558	9.17	0.0048	+

DE	0.0390	1	0.0390	6.41	0.0163	+
B^2	0.3737	1	0.3737	61.41	< 0.0001	++
E^2	0.8751	1	0.8751	143.80	< 0.0001	++
Residual	0.2008	33	0.0061			
Lack of Fit	0.2008	28	0.0072			
Pure Error	0.0000	5	0.0000			
Cor Total	124.93	45				

Note: ++ means extremely significant (p-value<0.001); + means significant (0.001<p-value<0.05) and - means insignificant (p-value>0.05)

The perturbation plot can reflect the influence of the input factors on the tendency and sensitivity of the response. The positive gradient of a curve means that the value of an output response grows with the increasing input factor, while the negative gradient indicates that the higher value of a factor leads to a reduction of the response. In addition, the response is more sensitive to a factor when the curve gradient is steep. For the response of primary air temperature drop, it can be noticed from Fig. 5.3.2 that the primary air inlet temperature ($t_{p,in}$) is more sensitive than the other four factors in the two spraying modes. In addition, only the slopes of the black and purple curves are positive, which means that the increasing primary air inlet temperature ($t_{p,in}$) and secondary air velocity (v_s) can reduce the response value. Among the three curves with negative slopes, the primary air velocity (v_p) is more sensitive than the secondary air inlet temperature ($t_{s,in}$) and relative humidity ($RH_{s,in}$).

Regarding the response surfaces and contours of the primary air temperature drop, there is only one interactive term ($v_p t_{s,in}$) of the adjustable factors that need to be presented after passing the AIC and the p-value checking. As shown in Fig. 5.3.3, the lower primary air velocity (v_p) and secondary air inlet temperature ($t_{s,in}$) contribute to the larger primary air temperature drop, and the trend is consistent with the previous discussions. The greatest primary air temperature drops are observed as 5.99℃ and 6.23℃ when the primary air velocity (v_p) and secondary air inlet temperature (t_s) are 1.5 m/s and 24℃, respectively, in both two spraying modes.

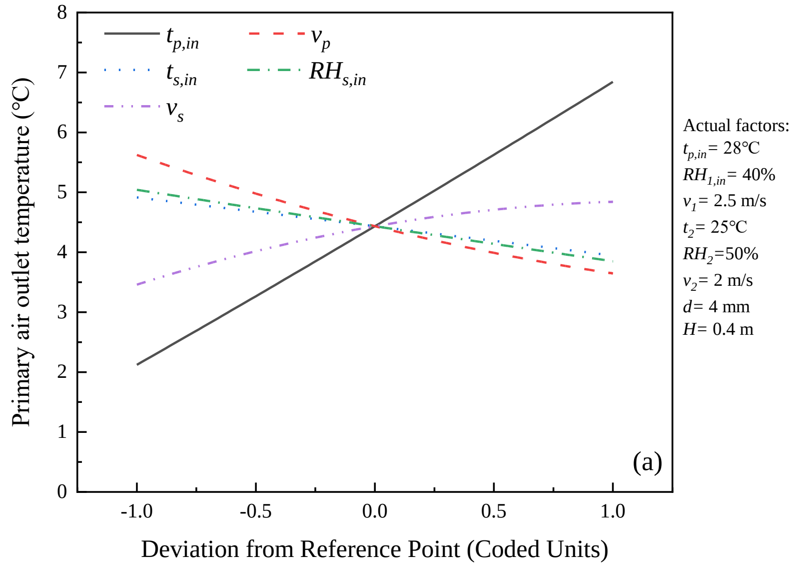

(a) consistent spraying mode

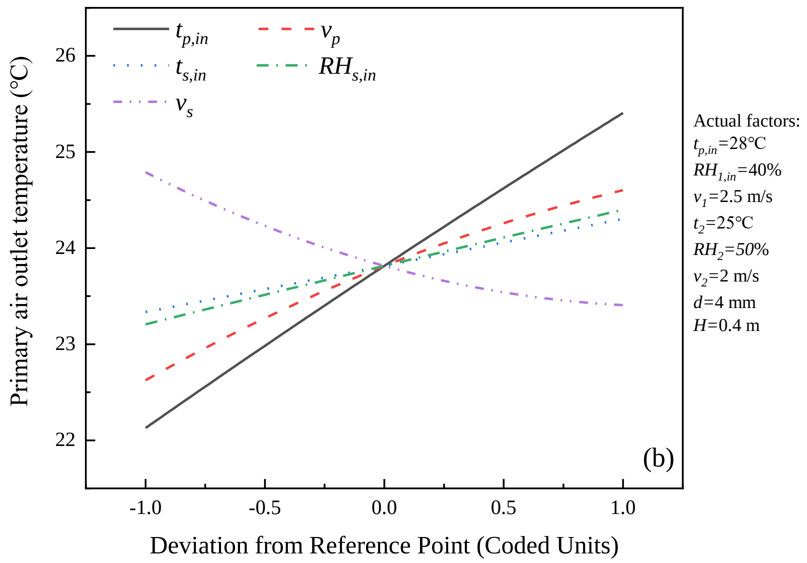

(b) periodic spraying mode

Fig. 5.3.2 Perturbation plot of primary air temperature drop

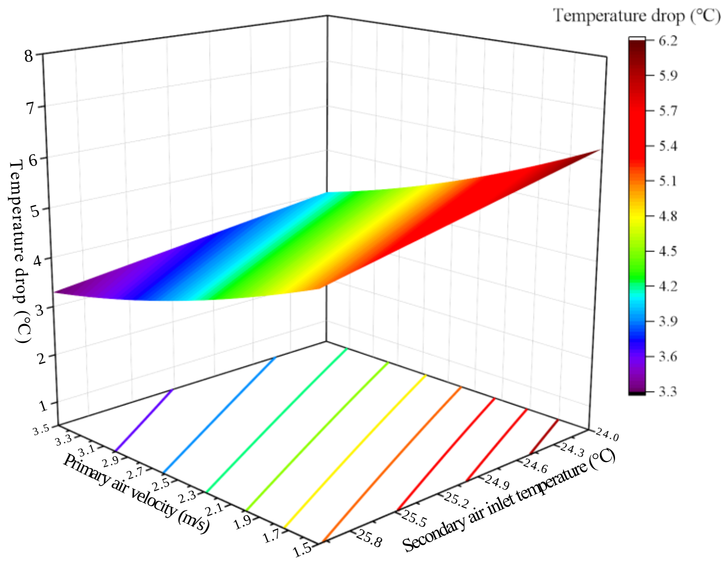

(a) Consistent spraying mode

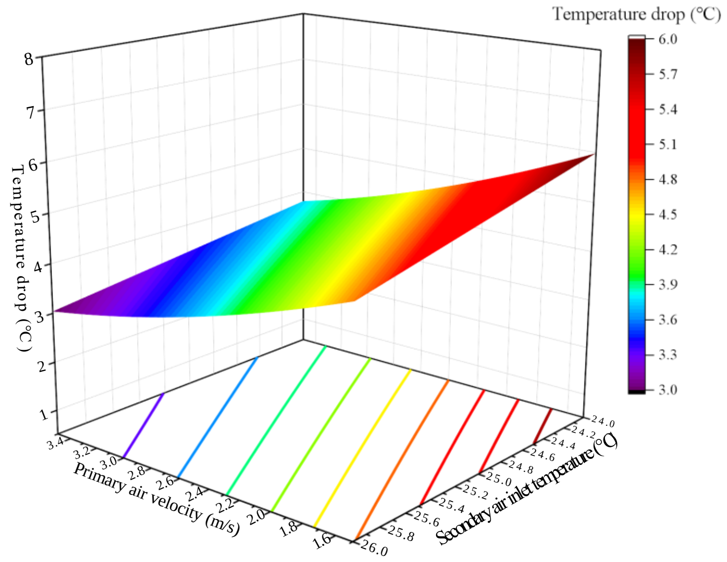

(b) Periodic spraying mode

Fig. 5.3.3 The response surface and contour for the influence of factors on primary air outlet temperature

5.3.3 Response of wet-bulb efficiency

The results of ANOVA for the response of wet-bulb efficiency under two spraying modes are listed in Table 5.3.4 and Table 5.3.5. Under the consistent spraying mode (Table 5.3.4), the total sum of squares is 0.3290, with 0.3276 of it explained by the model. The residual sum of squares is 0.0014, indicating a good fit of the model to the data. All the linear terms, four out of ten interactive terms, and three out of five square terms pass the AIC, and their p-values are within the upper bound of 0.05, which are all the significant terms to be used in the regression model formulation as Eq. (51).

Table 5.3.5 shows the ANOVA results for the intermittent spraying mode, the numbers of qualified linear, interactive, and square terms are five, four, and three. These terms are used to formulate the regression model of wet-bulb efficiency under the periodic spraying plan, as expressed by Eq. (52).

$$\eta_{wb,con} = 2.13684 + 0.00988815t_{p,in} - 0.112913v_p - 0.126977t_{s,in} - 0.534719RH_{s,in} - 0.0313113v_s - 0.00298465t_{p,in}v_p + 0.0034596t_{p,in}t_{s,in} + 0.0224793t_{p,in}RH_{s,in} + 0.0153617t_{s,in}v_s - 0.00146953t_{p,in}^2 + 0.020139v_p^2 - 0.108649v_s^2 \quad (51)$$

$$\eta_{wb,int} = 2.44152 + 0.0090889t_{p,in} - 0.113918v_p - 0.144867t_{s,in} - 0.907353RH_{s,in} - 0.0325939v_s - 0.00298465t_{p,in}v_p + 0.0040147t_{p,in}t_{s,in} + 0.0341017\,t_{p,in}RH_{s,in} + 0.015362\,t_{s,in}v_s - 0.00175414t_{p,in}^2 + 0.0203216v_p^2 - 0.107919v_s^2 \quad (52)$$

Table 5.3.4 ANOVA for the response of wet-bulb efficiency (consistent spraying mode)

Source	Sum of Squares	df	Mean Square	F-value	p-value	
Model	0.3276	12	0.0273	643.08	< 0.0001	++
A - $t_{p,in}$	0.0817	1	0.0817	1924.33	< 0.0001	++
B - v_p	0.1468	1	0.1468	3458.60	< 0.0001	++
C - $t_{s,in}$	0.0035	1	0.0035	81.97	< 0.0001	++
D - $RH_{s,in}$	0.0014	1	0.0014	33.81	< 0.0001	++
E - v_s	0.0734	1	0.0734	1728.49	< 0.0001	++

AB	0.0006	1	0.0006	13.43	0.0009	+
AC	0.0008	1	0.0008	18.05	0.0002	+
AD	0.0003	1	0.0003	7.62	0.0094	+
CE	0.0002	1	0.0002	5.56	0.0245	+
A^2	0.0055	1	0.0055	128.71	< 0.0001	++
B^2	0.0040	1	0.0040	94.43	< 0.0001	++
E^2	0.0073	1	0.0073	171.77	< 0.0001	++
Residual	0.0014	33	0.0000			
Lack of Fit	0.0014	28	0.0001			
Pure Error	0.0000	5	0.0000			
Cor Total	0.3290	45				

Note: ++ means extremely significant (p-value<0.001); + means significant (0.001<p-value<0.05) and - means insignificant (p-value>0.05)

Table 5.3.5 ANOVA for the response of wet-bulb efficiency (periodic spraying mode)

Source	Sum of Squares	df	Mean Square	F-value	p-value	
Model	0.3604	12	0.0300	591.60	< 0.0001	++
A - $t_{p,in}$	0.1109	1	0.1109	2184.38	< 0.0001	++
B - v_p	0.1471	1	0.1471	2897.09	< 0.0001	++
C - $t_{s,in}$	0.0047	1	0.0047	92.08	< 0.0001	++
D - $RH_{s,in}$	0.0004	1	0.0004	7.11	0.0118	+
E - v_s	0.0736	1	0.0736	1449.02	< 0.0001	++
AB	0.0006	1	0.0006	11.23	0.0020	+

AC	0.0010	1	0.0010	20.32	< 0.0001	++
AD	0.0007	1	0.0007	14.66	0.0005	
CE	0.0002	1	0.0002	4.65	0.0385	+
A^2	0.0078	1	0.0078	153.33	< 0.0001	++
B^2	0.0041	1	0.0041	80.38	< 0.0001	++
E^2	0.0072	1	0.0072	141.69	< 0.0001	++
Residual	0.0017	33	0.0001			
Lack of Fit	0.0017	28	0.0001			
Pure Error	0.0000	5	0.0000			
Cor Total	0.3621	45				

Note: ++ means extremely significant (p-value<0.001); + means significant (0.001<p-value<0.05) and - means insignificant (p-value>0.05)

The variation trend and sensitivity of the influential single parameters are shown by the perturbation plot in Fig. 5.3.4. The curves observed on the graph of intermittent spraying appear to be shifted downwards by a small amount in comparison to the curves on the graph of consistent spraying. It can be noticed that the primary air inlet temperature ($t_{p,in}$), primary air velocity (v_p), and secondary air velocity (v_s) have higher sensitivity, while the slopes of $t_{p,in}$ and v_s generally reduce. The curves of secondary air inlet temperature ($t_{s,in}$) and secondary air relative humidity ($RH_{s,in}$) are flat under both traditional spraying and intermittent spraying strategies, indicating the less influence on the response compared with the former three factors. In addition, the slopes of the primary air inlet temperature ($t_{p,in}$) and secondary air velocity (v_s) generally decrease, indicating that the degree of influence weakens when the two input parameters become larger.

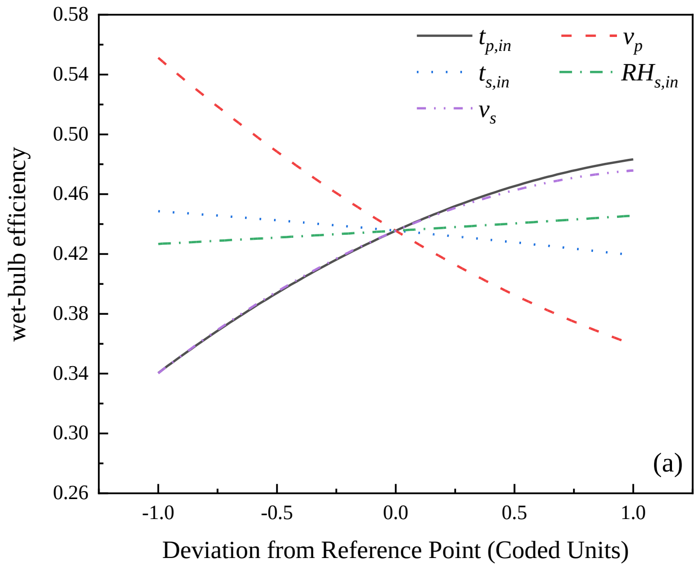

(a) consistent spraying mode

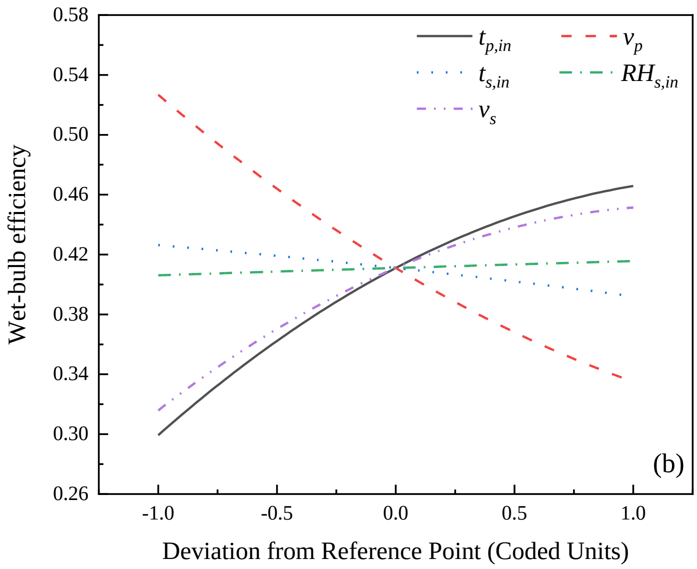

(b) periodic spraying mode

Fig. 5.3.4 Perturbation plot of wet-bulb efficiency

The response surfaces and contours of wet-bulb efficiency are presented in Fig. 5.3.5. For this response, only one interactive term ($t_{s,in}v_s$) that contains both controllable parameters meets the requirements of AIC and p-value checking. The low secondary air inlet temperature ($t_{s,in}$) and high secondary air velocity (v_s) lead to a greater response value under the two spraying conditions. When the secondary air inlet temperature ($t_{s,in}$) is 24℃ and the secondary air velocity (v_s) is 1.5 m/s, the wet-bulb efficiencies reach the peak values of 0.482 and 0.460 for the conventional spraying and periodic spraying, respectively.

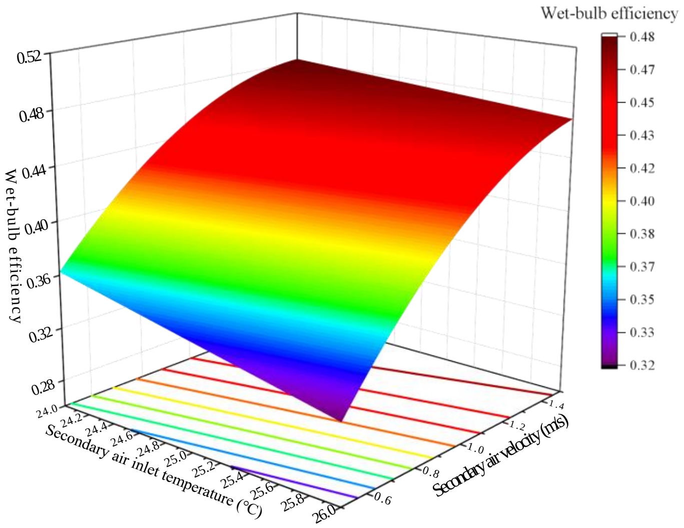

(a) Consistent spraying mode

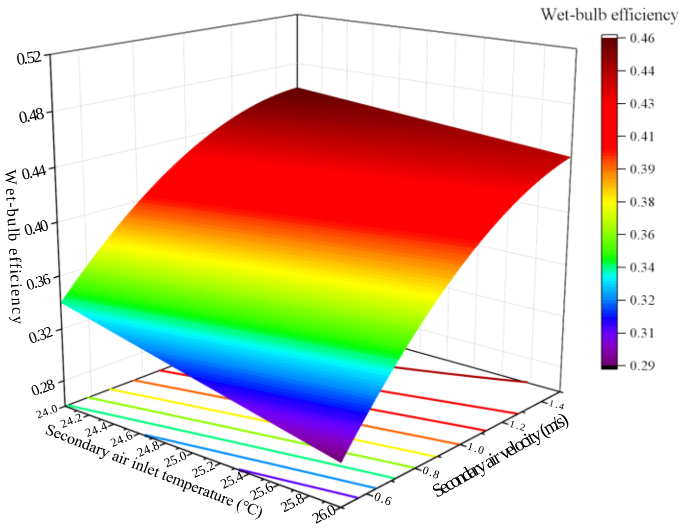

(b) Periodic spraying mode

Fig. 5.3.5 The response surface and contour for the influence of factors on wet-bulb efficiency

5.3.4 Response of *COP*

Table 5.3.6 presents the results of ANOVA for COP in a consistent spraying mode. The overall fit of the model is highly significant, with an F-value of 1502.82 and a p-value less than

0.0001. The model explains a significant portion of the variance in the response variable, as indicated by the sum of square value of 1449.40. After the AIC testing, five linear terms, four interactive terms, and two square terms are available. The p-value of all terms except v_s is within 0.05, which is significant so as to be included in the regression model. However, the linear term is also involved to ensure that the model is hierarchical although the p-value exceeds the upper bound. Thus, the regression model of the COP under consistent mode can be written by Eq. (53).

Under the periodic spraying mode, as shown in Table 5.3.7, the total sum of squares is 4588.05 with 4568.68 from the model. All linear terms are significant as their p-values are much lower than 0.05. Besides, three interactive terms and two square terms satisfy the AIC and range of p-value. Therefore, they are used for developing the regression model of *COP*, and the final format is written by Eq. (54).

$$COP_{con} = 31.4183 + 1.96468t_{p,in} - 0.336358v_p - 2.67225t_{s,in} - 22.8679RH_{s,in} - 10.5006v_s + 0.16869t_{p,in}v_p + -0.163553t_{p,in}v_s + 1.98825v_pv_s + 0.81318t_{s,in}v_s - 1.08789v_p^2 - 5.02043v_s^2 \quad (53)$$

$$COP_{int} = 57.7062 + 5.17544t_{p,in} - 2.35812v_p - 5.5639t_{s,in} - 37.836RH_{s,in} - 36.0146v_s - 1.31159t_{p,in}v_s + 7.92069v_pv_s + 2.30796t_{s,in}v_s - 1.50371v_p^2 + -5.48835v_s^2 \quad (54)$$

Table 5.3.6 ANOVA for the response of *COP* (consistent spraying mode)

Source	Sum of Squares	df	Mean Square	F-value	p-value	
Model	1449.40	11	131.76	1502.82	< 0.0001	++
A - $t_{p,in}$	1264.91	1	1264.91	14426.86	< 0.0001	++
B - v_p	14.01	1	14.01	159.80	< 0.0001	++
C - $t_{s,in}$	55.30	1	55.30	630.70	< 0.0001	++

D - $RH_{s,in}$	83.67	1	83.67	954.30	< 0.0001	++
E - v_s	0.1284	1	0.1284	1.46	0.2346	-
AB	1.82	1	1.82	20.77	< 0.0001	++
AE	0.4280	1	0.4280	4.88	0.0340	+
BE	3.95	1	3.95	45.09	< 0.0001	++
CE	0.6613	1	0.6613	7.54	0.0096	+
B^2	12.07	1	12.07	137.68	< 0.0001	++
E^2	16.07	1	16.07	183.26	< 0.0001	++
Residual	2.98	34	0.0877			
Lack of Fit	2.98	29	0.1028			
Pure Error	0.0000	5	0.0000			
Cor Total	1452.38	45				

Note: ++ means extremely significant (p-value<0.001); + means significant (0.001<p-value<0.05) and - means insignificant (p-value>0.05)

Table 5.3.7 ANOVA for the response of *COP* (periodic spraying mode)

Source	**Sum of Squares**	**df**	**Mean Square**	**F-value**	**p-value**	
Model	4568.68	10	456.87	825.70	< 0.0001	++
A - $t_{p,in}$	3821.92	1	3821.92	6907.36	< 0.0001	++
B - v_p	61.21	1	61.21	110.63	< 0.0001	++
C - $t_{s,in}$	169.62	1	169.62	306.55	< 0.0001	++
D - $RH_{s,in}$	229.05	1	229.05	413.96	< 0.0001	++
E - v_s	154.51	1	154.51	279.25	< 0.0001	++

AE	27.52	1	27.52	49.74	< 0.0001	++
BE	62.74	1	62.74	113.39	< 0.0001	++
CE	5.33	1	5.33	9.63	0.0038	+
B²	23.06	1	23.06	41.68	< 0.0001	++
E²	19.20	1	19.20	34.71	< 0.0001	++
Residual	19.37	35	0.5533			
Lack of Fit	19.37	30	0.6455			
Pure Error	0.0000	5	0.0000			
Cor Total	4588.05	45				

Note: ++ means extremely significant (p-value<0.001); + means significant (0.001<p-value<0.05) and - means insignificant (p-value>0.05)

The perturbation plots of *COP* under conventional consistent spraying and periodic spraying conditions are presented in Fig. 5.3.6. Under both two spraying modes, the primary air inlet temperature ($t_{p,in}$) is observed as the most sensitive among the five single linear factors, which is almost a straight line with positive slope. While it can be seen that the secondary air inlet temperature ($t_{s,in}$) and relative humidity ($RH_{s,in}$) both have a negative slope, indicating that the response values decrease when the two input factors increase. For the consistent spraying condition, the slopes of primary air velocity (v_p) and secondary air velocity (v_s) are both positive in the beginning, while the two curves generally become flat and then slightly towards down given the higher value of the two factors. For the periodic spraying, the slopes of these two lines are relatively flat at lower input value, and they increase as the input values increase with a negative slope, which means that the higher channel air velocities can reduce the response values of *COP*.

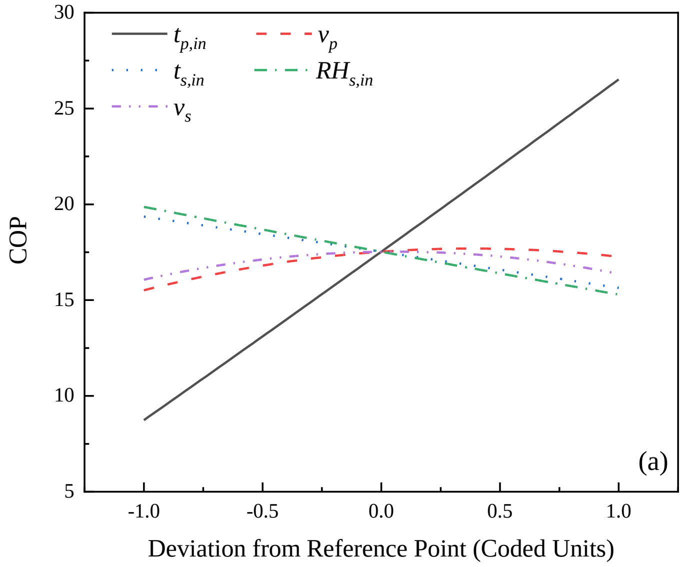

(a) consistent spraying mode

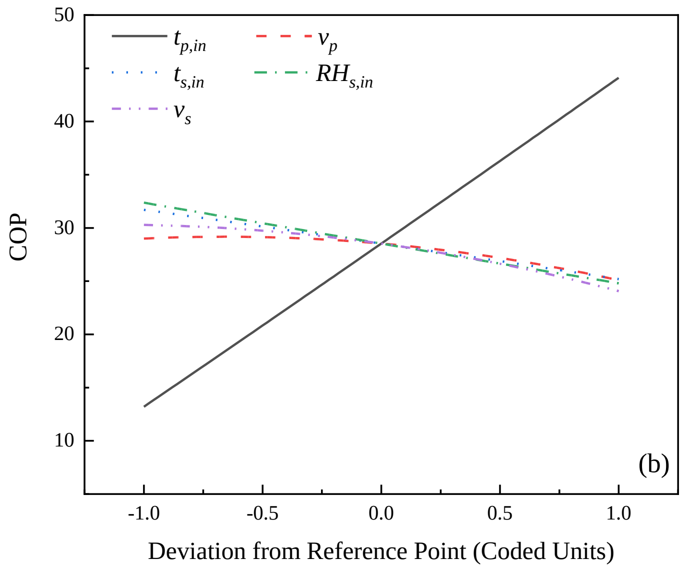

(b) periodic spraying mode

Fig. 5.3.6 Perturbation plot of *COP*

Regarding the response surfaces and contours of *COP* under the traditional continuous spraying and the intermittent spraying, the significant interactive terms with controllable parameters are $v_p v_s$ and $t_s v_s$ based on the results of ANOVA. As shown in Fig. 5.3.7(a) and (c), under the consistent spraying mode, it is noticed that the response value may not be unlimitedly improved by changing the factors to maximum or minimum value based on the variation trends of the single factor. The interactive factors need to be controlled simultaneously for getting the better performance. The peak response value is achieved as 17.8 and 19.4 when v_p= 3.05 m/s, v_s= 1.11 m/s and $t_{s,in}$= 24℃, v_s= 0.95 m/s, respectively. While the under the intermittent spraying conditions (Fig. 5.3.7(b) and (d)), the peak value is obtained by minimizing the channel air velocities (v_p and v_s) and the secondary air inlet temperature (t_s). Specifically, the *COPs* both reach the maximum at 34.7 when v_p= 1.5 m/s, v_s= 0.5 m/s and $t_{s,in}$= 24℃, v_s=0.5 m/s.

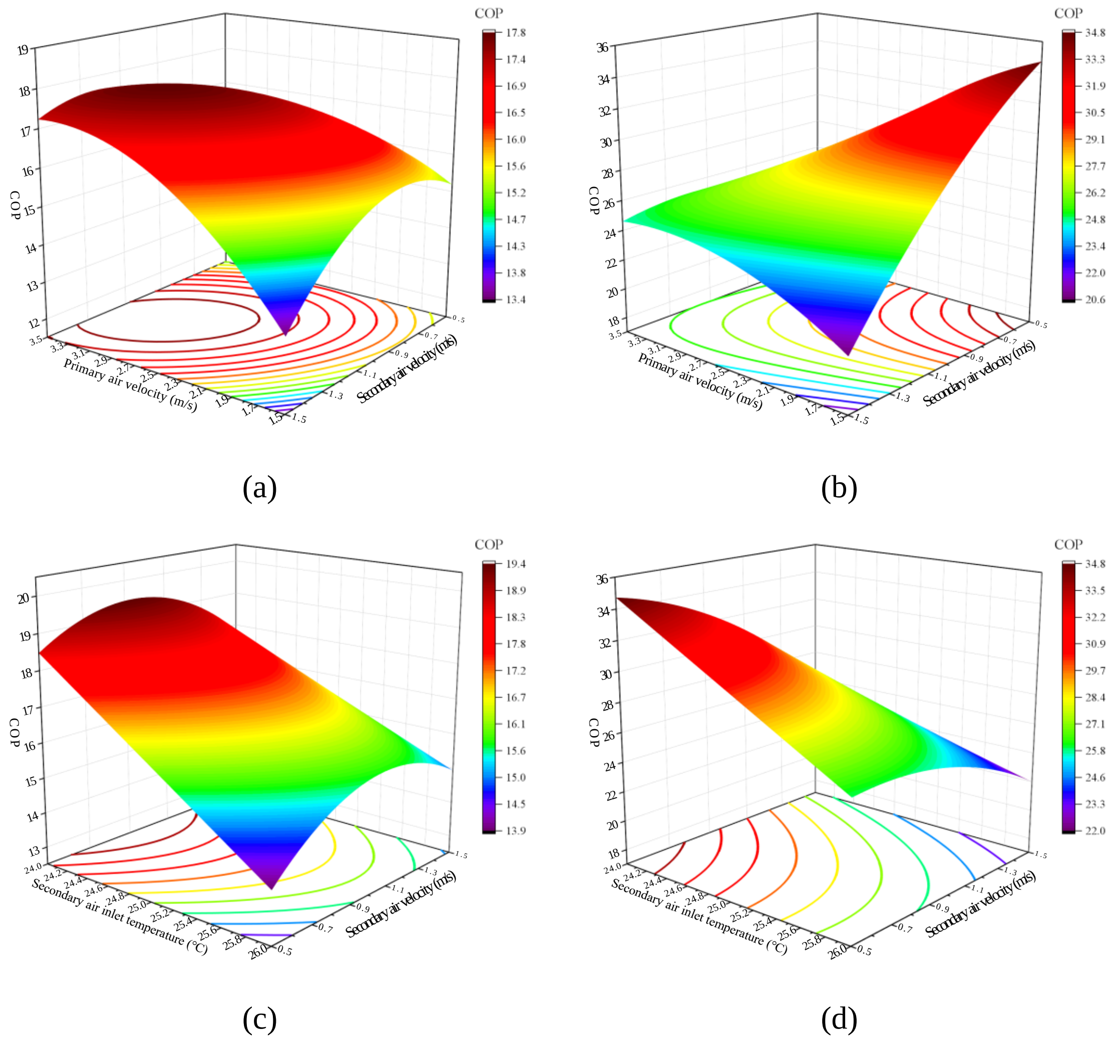

Fig. 5.3.7 The response surfaces and contours for the influence of factors on *COP* (a) v_p~ v_s (consistent spraying) (b) v_p~ v_s (periodic spraying) (c) t_s~v_s (consistent spraying) (d) t_s~v_s (periodic spraying)

5.3.5 Optimization of design parameters using desirability function

In addition to its use in forecasting, this RSM-based model can be used to optimize the IEC during the design stage of the AC system. The primary objectives of the optimization are to achieve greater cooling performance and higher energy efficiency. As discussed earlier, the PIEC system can operate under consistent and periodic spraying modes, and the performance indicators under these two spraying conditions are primary air temperature drop, wet-bulb efficiency, and *COP*. Therefore, the multi-objective optimization can be proposed using the desirability function considering the input parameter ranges in Table 5.2.1. The desirability function works by transforming each response variable into a dimensionless score between 0 and 1, where 0 represents the worst possible value and 1 represents the target value [147].

$$D = ({d_1}^{WF_1}{d_2}^{WF_2} \dots {d_n}^{WF_n})^{\frac{1}{\sum_1^n WF_n}} \tag{55}$$

where D is overall desirability score;

d_1, d_2, ..., d_n are desirability scores for each response variable;

WF_1, WF_2, ..., WF_n are the weighting factors for each response variable.

The optimization goals can be categorized into in range, maximize, and minimize, and the individual desirability needs to be calculated according to the different goals [148].

When the goal is to maximize one response, Eq. (56) should be employed:

$$d = \begin{cases} 0, & (y \leq l) \\ \left(\dfrac{y-l}{U-l}\right)^r, & l \leq y \leq U \\ 1, & (U \leq y) \end{cases} \tag{56}$$

When the goal is to minimize one response, Eq. (57) is utilized:

$$d = \begin{cases} 1, & (U \leq y) \\ \left(\frac{U-y}{U-l}\right)^r, & l \leq y \leq U \\ 1, & (y \leq l) \end{cases} \tag{57}$$

where *d* is desirability score for the response variable;

y is actual value of the response variable;

l is lower limit of the acceptable range for the response variable;

U is upper limit of the acceptable range for the response variable;

r is weight of a corresponding response.

The weighting factors for each response variable are based on the relative importance of each response variable to the overall design objective. They are typically set by the user based on the problem and the design requirements. Once the desirability scores and weighting factors are determined, the overall desirability score is calculated using the weighted product of the individual desirability scores. The resulting score ranges between 0 and 1, with 1 representing the most desirable design [149]. During the optimization process, the indicators under the two spraying conditions are given equal importance. Then, the desirability is maximized based on the goals and the limited range of the input factors presented in Table 5.3.8, which can achieve the greatest desirability of 0.97 and 0.99 for traditional and periodic spraying, respectively, among all solutions.

Table 5.3.8 Optimized solution of the PIEC under the two spraying modes.

Name	Goal	Solution	
		Consistent	Intermittent
$t_{p,in}$	is in range	32	32

v_p	is in range	1.5	1.5
$t_{s,in}$	is in range	24	24
$RH_{s,in}$	is in range	0.4	0.42
v_s	is in range	1.2	1.1
$\Delta t_{p,con}$	is in range	10.1	-
$\eta_{wb, con}$	Maximize	0.61	-
COP_{con}	Maximize	27.3	-
$\Delta t_{p, int}$	Maximize	-	9.6
η_{wb_int}	Maximize	-	0.59
COP_{int}	Maximize	-	49.1
Desirability		0.974	0.99

5.4 Chapter summary

In this chapter, the response surface methodology (RSM) was employed to develop the regression models of the PIEC under consistent and intermittent spraying conditions for performance prediction and optimization. In this regard, five factors were determined as the inputs, and three indicators were selected as the output responses for both consistent and intermittent spraying modes. The Box-Behnken Design (BBD) was employed to generate the matrix for the RSM-based model, and the matrix response data were obtained from the 3-D established PIEC model validated by the experimental results. The regression models and the effects of the single and interactive factors are accordingly presented. Finally, the multi-objective optimizations of the controllable parameters are conducted for the PIEC under the two spraying modes based on the desirability function approach. In addition to obtaining the regression models of the responses under different spraying modes, the main findings can be summarized as follows.

1) The sensitivity of the input factors changes in the different responses. Primary air temperature and velocity exhibit greater sensitivity for responses of primary air temperature drop and wet-bulb efficiency in the consistent and intermittent spraying modes, while primary air and secondary air relative humidity display higher sensitivity than another three inputs for the response of COP under the two spraying modes.

2) The response value may not be unlimitedly improved by altering the factors to maximum or minimum value based on the variation trends of single factors. The interactive factors need to be controlled simultaneously for getting the better performance. The most significant *COP* under the consistent spraying is achieved when v_p= 3.05 m/s v_s= 1.11 m/s and $t_{s,in}$= 24℃, v_s= 0.95 m/s. While the *COP* reaches maximum when v_p= 1.5 m/s, v_s= 0.5 m/s and $t_{s,in}$= 24℃, v_s= 0.5 m/s in the intermittent spraying mode.

3) The adjustable input factors are optimized as v_p= 1.5 m/s, v_s= 1.2 m/s, $t_{s,in}$= 24℃ and v_p= 1.5 m/s, v_s= 1.1 m/s, $t_{s,in}$= 24℃ for consistent and periodic spraying modes, respectively. These optimizations result in the highest desirability, considering the simultaneous maximized primary air temperature drop, wet-bulb efficiency, and *COP*.

In summary, the simplified approach for forecasting the performance of the PIEC system using regression models based on RSM can provide a more practical and convenient alternative to the computationally-intensive 3-D CFD model, which can facilitate the implementation and optimization of the PIEC system in engineering applications.

Chapter 6 Energy, exergy, and environmental (3E) analysis of the PIEC system

Based on the 3-D model and the empirical model obtained from response surface methodology (RSM), the cooling performance of the indirect evaporative cooler with porous material on the secondary air channel surface (PIEC) can be predicted under the consistent and periodic spraying modes. Therefore, the performance comparisons should be carried out between the traditional consistent spraying and periodic spraying modes from the energy, exergy, and environmental (3E) perspectives, which are presented in this chapter.

This chapter is written based on an accepted manuscript of this thesis author. The paper is titled "*A novel indirect evaporative cooler with porous media under dual spraying modes: a comparative analysis from energy, exergy, and environmental perspectives*" accepted by *Journal of Building Engineering*.

6.1 Significance of 3E evaluation

The importance of performing 3E evaluations is rooted in their ability to offer a comprehensive analysis of the performance and sustainability of energy systems [150]. The energy evaluation assist in determining the energy efficiency of a system, recognizing energy waste and consumption concerns in some cases, and suggesting methods to decrease energy usage [46]. The exergy evaluation is more sophisticated, which considers energy quality and evaluates the irreversibility of energy transformations within a system [151]. The environmental evaluation examines the ecological impact of energy systems, such as identifying pollutant emissions, greenhouse gas emissions, and the utilization of natural resources [152].

6.2 Performance indicators of 3E evaluation

6.2.1 Energy indicator

Three indicators are employed as energy indicators, namely, wet-bulb efficiency, cooling capacity, and *COP*, which have been pervasively used and written from Eq. (58) to Eq. (59) and Eq. (61) [153-155].

$$\eta_{wb} = \frac{t_{p,in} - t_{p,out}}{t_{p,in} - t_{wb,s,in}} \tag{58}$$

$$Q = m_p c_{pa}\left(t_{p,in} - t_{p,out}\right) \tag{59}$$

where $t_{p,out}$ is the outlet temperature in the consistent spraying mode, which needs to be replaced and calculated by Eq. (60) during a ranged cycle in the periodic spraying scenarios.

$$t'_{p,out} = \frac{\int_{\tau_0}^{\tau_2} t_{p,out}\, d\tau}{\tau_2 - \tau_0} \tag{60}$$

where τ_0 and τ_2 represent the start and end time points of a cycle, respectively.

$$COP = \frac{Q}{W_{fans} + (W_{pump} or\ W_{pump}')} \tag{61}$$

The power load from fans can be calculated by Eq. (62) according to the existing IEC literature [112]. The values of fan power are figured according to the supply air volume and an assumed distribution resistance of 30 Pa for both primary air and secondary air loops.

$$W_{fan} = \frac{Q\Delta P_i}{\eta_0 \eta_1} \cdot K \tag{62}$$

$$P_i = \frac{f_{Re}L}{ReD_e} \cdot \frac{\rho u^2}{2} \tag{63}$$
$$(\, i = p, s)$$

$$f_{Re} = 96 * (1 - 1.3553\alpha + 1.9467\alpha^2 - 1.7012\alpha^3 + 0.9564\alpha^4 - 0.2537\alpha^5) \tag{64}$$

where Q is air flow rate, m^3/h;

f_{Re} is friction coefficient;

L is length of IEC, m;

D_e is equivalent diameter, m;

Re is Reynolds number;

α is the dimensionless shape factor;

η_0, η_1 are internal efficiency mechanical efficiency of the fan;

K is the motor capacity coefficient.

The water pump power in the consistent mode and equivalent power of a cycle under periodic spraying can be obtained by the following equations, which are both related to the head loss of the nozzle, gravity, and valves.

$$W_{pump} = m_{sp} \cdot g \cdot h_{total} \cdot K \tag{65}$$

$$W_{pump}{}' = \frac{\int_{\tau_0}^{\tau_1} m_{sp} \cdot g \cdot h_{total} \cdot K d\tau}{\tau_2 - \tau_0} \tag{66}$$

where τ_1 is time point pausing the water spraying;

g is the gravitational acceleration, m/s^2;

h_{total} is total heat loss, m;

m_{sp} is the mass flow of the spraying water, kg/s;

$$h_{total} = h_{nozzle} + h_{gravity} + h_{valve} \tag{67}$$

where h_{nozzle}, $h_{gravity}$ and h_{value} are the head loss from water nozzles, the gravity, and water valves on the pipeline, m.

6.2.2 Exergy indicator

Exergy is a measure of the amount of work that can be extracted from a system as it comes to equilibrium with a reference environment, taking into account the quality and availability of the energy. It is a concept in thermodynamics that provides a more complete understanding of the potential for energy conversion and the limitations imposed by the laws of thermodynamics. The total exergy of the moist air is mainly the sum of its thermal exergy, chemical exergy, and mechanical exergy (Eq. (68)) [151, 156, 157].

$$Ex = Ex_{ther} + Ex_{chem} + Ex_{mech} \tag{68}$$

where Ex_{ther}, Ex_{chem}, Ex_{mech}, are thermal, chemical, and mechanical exergy, W (consistent spraying) and Wh (periodic spraying);

The thermal exergy is the part of the total exergy of a substance that is associated with its temperature and can be converted into useful work in a thermal process, which can be expressed by Eq. (69):

$$Ex_{ther} = m(c_{pa} + \omega c_{pv})(T - T_0 - T_0 \ln(\frac{T}{T_0})) \tag{69}$$

where T, T_0 are temperature and temperature at saturated air dead state, K;

m is mass flow rate, kg/s;

ω is humidity ratio, kg/kg(dry air);

c_{pa}, c_{pv} are specific heat capacity of dry air and water vapor at constant pressure, J/(kg·K);

The chemical exergy is the maximum amount of useful work that can be obtained from a chemical substance as it reacts with a reference environment at a specified temperature, pressure, and composition. It is related to the air humidity ratio and is calculated by Eq. (70):

$$Ex_{chem} = m((1 + 1.608w)T_0R_a l\,n\left(\frac{1 + 1.608\omega_0}{1 + 1.608\omega}\right) + 1.608wT_0R_a l\,n\left(\frac{\omega}{\omega_0}\right)) \tag{70}$$

where R_a is specific gas constant for dry air,

ω, ω_0 are humidity ratio and humidity ratio at saturated air dead state, kg/kg(dry air).

The mechanical exergy, also known as work exergy, is the part of the total exergy of a substance that can be converted into useful work in a mechanical process, which is related to the pressure and can be formulated by Eq. (71):

$$Ex_{mech} = m(1 + 1.608\omega)R_aT_0\ln\left(\frac{P}{P_0}\right)) \tag{71}$$

where P, P_0 are humidity ratio and humidity ratio at saturated air dead state, kg/kg(dry air);

Several assumptions can be made prior to calculating the exergy for different operating conditions. Firstly, it has been proved that the energy conversion predominantly leads to the heat and mass transfer in the IEC rather than the work from minor pressure changes. Therefore, mechanical exergy because of the pressure drop is usually ignored in IEC exergy analysis [124]. Secondly, the saturation point of the primary inlet air is determined as the reference/dead state [158]. Thirdly, the tiny convection that arises in the porous layer is not considered. Fourthly, in the continuous mode, the inlet and outlet water status is identical. In the periodic mode, one cycle is taken as the objective for analysis, and the inlet and outlet statuses of the wet porous media are identical. Therefore, the water exergy in the stable spraying mode and the exergy of the wet porous media in the periodic spraying mode are both neglected.

Hence, the exergy balance equation of the PIEC can be formulated by Eq. (72):

$$Ex_{p,in} + Ex_{s,in} - Ex_{p,out} - Ex_{s,out} - Ex_{loss} + Ex_{fan} + Ex_{pump} = 0 \tag{72}$$

When evaluating the exergy performance of the IEC system, the exergy efficiency usually needs to be calculated. Ratlamwala and Dincer mentioned that the definition of this indicator varies based on different understandings [159]. It is necessary to summarize the commonly-used definitions in published IEC research as follows: 1) the ratio of output exergy to supply exergy [160, 161]; 2) the ratio of produced exergy by conversion to the supplied exergy for maintaining the transfer process [124, 162]. In recent studies, the latter definition has become popular because it weakens the influence of the dead state and allows for a greater extent of variation in the results due to changes in input parameters. Hence, the second definition is adopted in this study as shown in Eq. (73).

$$\eta_{ex} = \frac{\Delta Ex_p}{\Delta Ex_s + Ex_{fan} + Ex_{pump}} \tag{73}$$

The exergy loss ratio is defined as the exergy loss to the input exergy as formulated in Eq. (74).

$$\eta_{loss} = \frac{Ex_{loss}}{Ex_{in}} \tag{74}$$

6.2.3 Environmental indicator

The CO_2 emission, which is the most important when it comes to carbon peaking and carbon neutrality, is determined as the environmental indicator and can be calculated by Eq. (75). In this study, the emission coefficient of CO_2 can be appointed as 0.581 kg/kWh according to the latest notice issued by the official governmental ministry [163].

$$m_{emission} = f_{CO_2}E \tag{75}$$

$$E = \frac{Q}{COP}\tau \tag{76}$$

where f_{CO_2} is greenhouse gas emission intensity, kg/kWh;

E is energy consumption of the system, kWh;

τ is system operation time, h.

6.3 Periodic spraying and consistent spraying

As known from the experiments and simulation in the previous two chapters, the PIEC can cool the air under both consistent and periodic spraying conditions. Fig. 6.3.1 exhibits the temperature variation and the spraying system operation under the two modes, represented by scenarios 1 and scenarios 2, respectively. The PIEC is wetted in advance during the preparation stage in both two cases, and then the two fans start working. In scenario 1, when the lowest temperature is obtained, the water system continues working to distribute liquid water into the secondary channel. Because water is sufficient for evaporation, the outlet temperature keeps as constant. In scenario 2, after getting the lowest temperature, the outlet supply air temperature fluctuates within 0.5℃ by controlling the on/off status of the water system for several cycles.

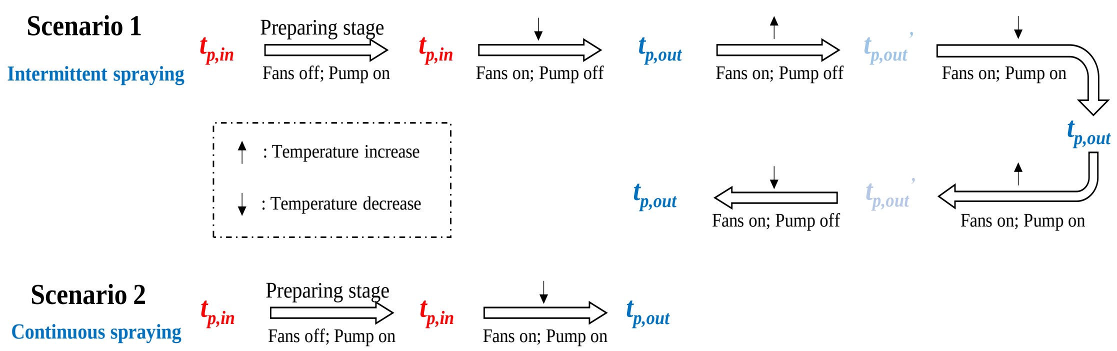

(a) Temperature variation

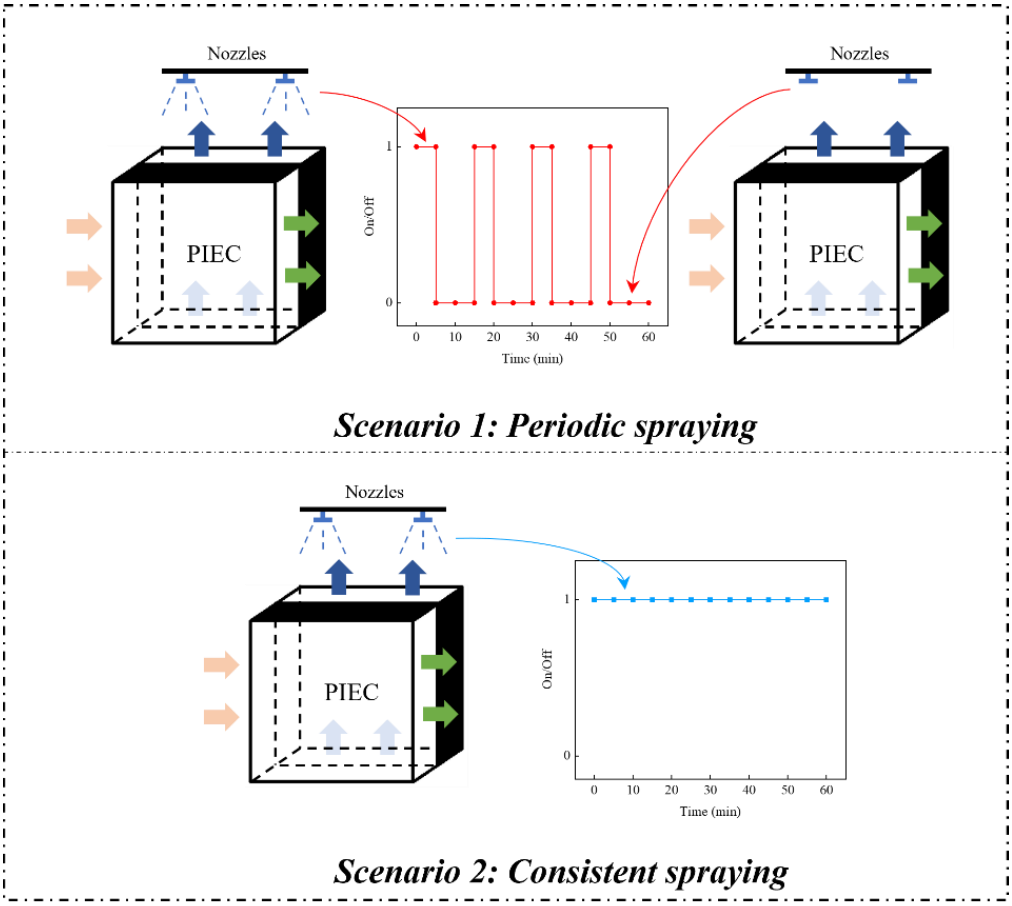

(b) Spraying system operation

Fig. 6.3.1 Scenarios with two spraying modes of the PIEC water system

In order to present the pair of cases for comparison, a pre-test is carried out as an example to illustrate the two spraying modes with the input parameters of $t_{p,in}$ = 30°C, $RH_{p,in}$ = 40%, v_p =3 m/s, $t_{s,in}$ = 25°C, $RH_{s,in}$ = 60%, v_s = 2 m/s, and d = 4 mm. Fig. 6.3.2 shows the variation of the primary air outlet temperature in the 9000 seconds of simulation. The light pink area is the spraying period. The rest of the time is named interval or non-spraying period, corresponding to the light green region. Under the periodic spraying mode, the PIEC is thoroughly wetted to ensure the air can be cooled to the lowest temperature, and then the water supply is interrupted. It can be seen that the temperature drops rapidly from 30°C to 24.82°C, and it gradually turns up and reaches 25.32°C due to the insufficient amount of water, which is also the signal (0.5°C temperature rise threshold) to recover the water spraying. The outlet temperature determines the opening point of the spray system, which eventually forms several cycles within the range of every double-headed arrow. For recurrent spraying conditions, the temperature varies periodically so that any cycle (such as the solid brown line) can be taken for 3E analysis. In this scenario, the water is sprayed for 120 s (pink area) and paused for 2040 s (light green area). While for continuous spraying conditions, the temperature value can be stabilized at the lowest point (such as point A in Fig. 6.3.2), and its corresponding inlet and outlet parameters of the heat exchanger are used for 3E evaluation.

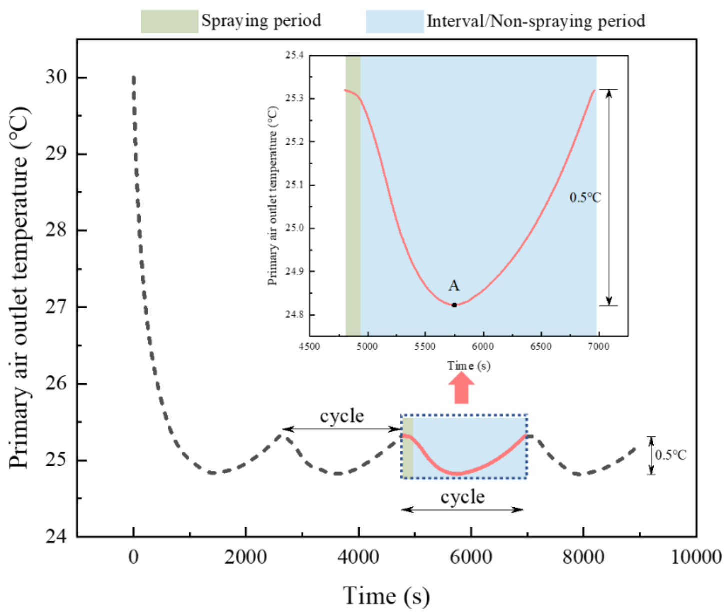

Fig. 6.3.2 PIEC primary air outlet temperature profile under periodic spraying

In order to compare the 3E performance under different spraying conditions, the simulations are conducted based on the input parameters listed in Table 6.3.1, and the results are used to calculate the 3E indicators in the following section.

Table 6.3.1 Range of input parameters for PIEC performance analysis

Parameter	Range	Parameter	Range
$t_{p,in}$ (°C)	24-36	$RH_{s,in}$ (%)	60

$RH_{p,in}$ (%)	40	u_s (m/s)	1-3
u_p (m/s)	1.5-3.5	d (mm)	4, 5
$t_{s,in}$ (°C)	25	L (mm)	400

6.4 Energy performance

6.4.1 Influence of the primary air inlet temperature

Fig. 6.4.1 displays the influence of primary air inlet temperature on the wet-bulb efficiency, cooling capacity, and *COP* of the PIEC system under the two spraying modes. It is observed that all three energy indicators exhibit an increasing trend with higher inlet temperature. The wet-bulb efficiency and cooling capacity under the continuous spraying mode are slightly higher than those under the intermittent condition. For instance, when the channel height is 4 mm, the wet-bulb efficiency (solid black line) increases from 0.34 to 0.54 as input temperature grows from 24°C to 36°C, which is slightly superior to the values on the black dash line (Fig. 6.4.1(a)). A similar trend is observed for cooling capacity (Fig. 6.4.1(b)), with values increasing from 222.26 W to 1234.5 W and 193.7 W to 1202.3 W under continuous and intermittent modes, respectively. The *COP* values vary from 5.2 to 28.9 on the dashed line, which are greater than those on the solid line. Furthermore, the differences between the two lines are enlarged to 9.2 with the higher inlet temperature, and the growth ratio is up to 36.6% among these cases. When the channel height is 5 mm, the wet-bulb efficiency (solid red curve) increases from 0.28 to 0.46 as the input temperature grows from 24°C to 36°C, which is also marginally above the red dashed line. The cooling capacity ranges from 229.6 W to 1309.7 W under the consistent spraying condition, which is a little bit greater than them from 196.3 W to 1268.7 W with the intermittent spraying mode. Regarding the *COPs*, the enlarged differences between the two spraying plans are noticed with the higher inlet temperature as in the cases of d=4 mm, and the most significant increasing rate is 31.3%.

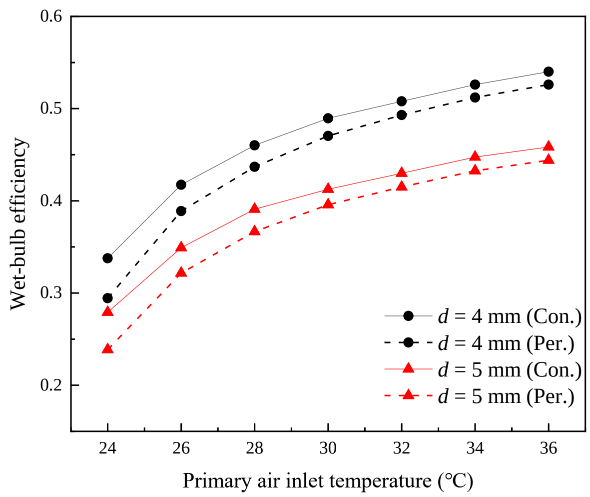

(a) Wet-bulb efficiency

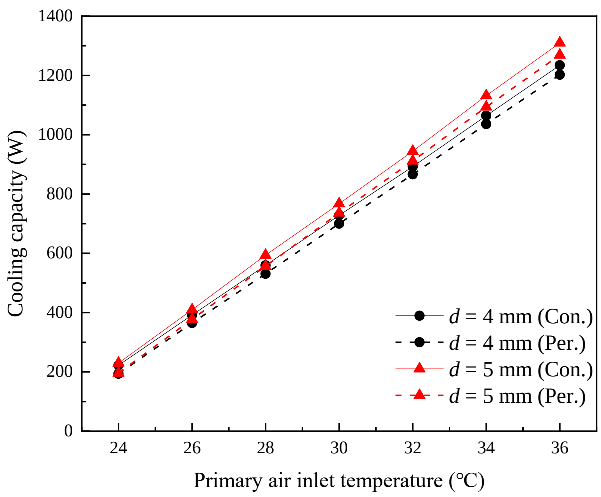

(b) Cooling capacity

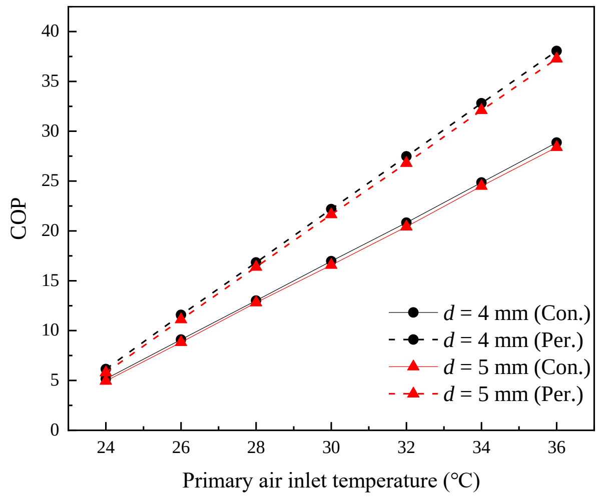

(c) *COP*

Fig. 6.4.1 Influence of the primary air inlet temperature on (a) Wet-bulb efficiency (b) Cooling capacity, and (c) *COP* under consistent and periodic spraying

6.4.2 Influence of the primary air velocity

The impact of the primary air velocity on the three indicators is depicted in Fig. 6.4.2. It can be found that the wet-bulb efficiency and cooling capacity with consecutive spraying are slightly higher than those in intermittent spraying conditions because the periodic mode cannot always maintain the lowest temperature as it is in the consistent circumstance. However, the tendencies of the three indicators are different. Taking the pair of cases that d = 4 mm for instance, the wet-bulb efficiency (solid orange line) declines significantly from 0.66 to 0.45 with the increase of primary air speed (Fig. 6.4.2(a)), and the values on the dashed line also fall from 0.64 to 0.43. Nonetheless, the cooling capacity shows an opposite trend and expands from 490.7 W to 798.1 W and from 474.2 W to 752.5 W in the two scenarios, given the faster velocity (Fig. 6.4.2(b)). *COP*s are enhanced by the higher air velocity, but the extent of the growth gradually weakens. The periodic strategy can achieve a 32.8% improvement of *COP* on average compared with the traditional plan (Fig. 6.4.2(c)). When the channel height is 5 mm, the wet-bulb efficiency (solid green curve) decreases from 0.58 to 0.38 as primary air velocity from 1.5 m/s to 3.5 m/s, which is also slightly higher than the green dash line. The cooling capacity ranges from 535.4 W to 827.0 W under the consistent spraying condition, which marginally exceeds them under the periodic spraying mode from 519.3 W to 787.9 W. Regarding the *COPs*, the periodic spraying can enhance the COP with the growing velocity from 1.5 m/s to 3.5 m/s, but the slope of the curve gradually becomes flat, which achieves the most significant increasing rate of 38.9% among the studied cases. In summary, raising the primary air velocity can stably promote the energy saving of the periodic spraying plan with a tiny temperature fluctuation, while the further elevation of *COP* will be quite limited when the speed reaches a certain value.

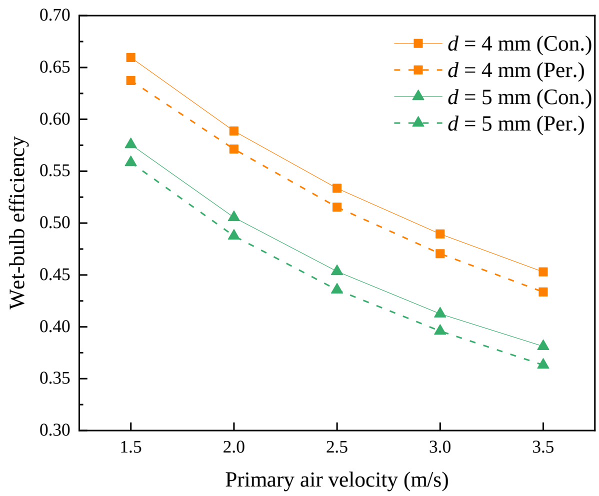

(a) Wet-bulb efficiency

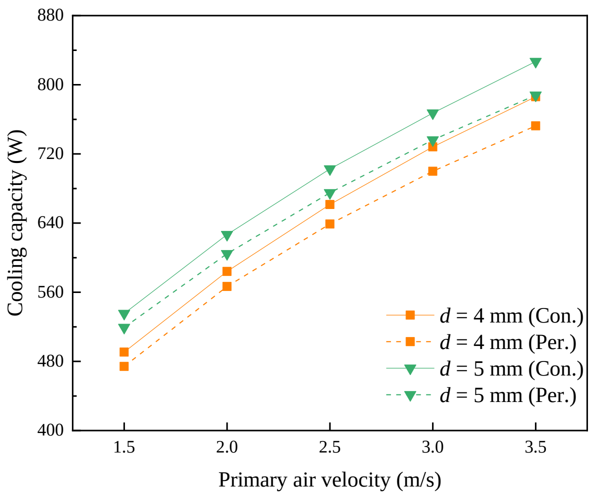

(b) Cooling capacity

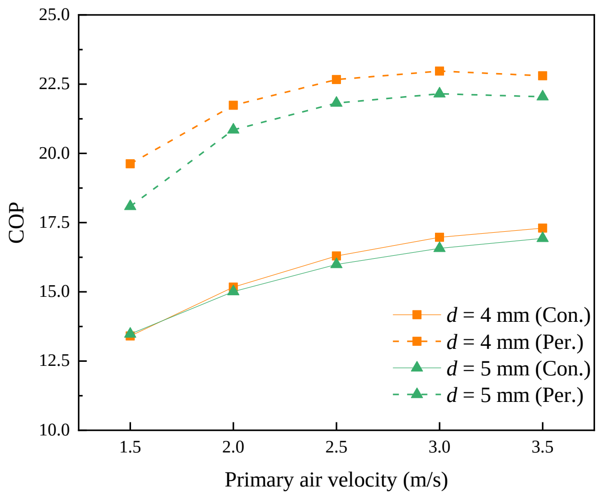

(c) *COP*

Fig. 6.4.2 Influence of the primary air velocity on (a) Wet-bulb efficiency (b) Cooling capacity, and (c) *COP* under consistent and periodic spraying

6.4.3 Influence of the secondary air velocity

The secondary air velocity is an essential parameter, and the influence of it on the three performance indicators is presented in Fig. 6.4.3. By and large, the increasing trend of wet-bulb efficiency and cooling capacity is noticed with the development of the secondary air velocity, and the stable spraying mode contributes to the greater performance. Contrary to the former two indicators, *COP*s suffer from great loss, and it is visibly upgraded by using the recurrent spraying plan. Taking a couple of scenarios that d = 4 mm as an example, in Fig. 6.4.3(a)-(b), the points on the solid blue line are larger than those on the dash blue line, and the best wet-bulb efficiency and cooling capacity are 0.43 and 767.12 W under the stable spraying mode. The maximum *COP* is obtained as 31.2 when the velocity is 1 m/s, which is 58.7% more than the traditional condition. When the channel height is 5 mm, the wet-bulb efficiency (solid purple curve) increases from 0.37 to 0.43 as primary air velocity from 1 m/s to 3 m/s, which is slightly higher than the purple dash line. The cooling capacity ranges from 680.7 W to 803.7 W under the consistent spraying condition, which marginally exceeds them under the periodic spraying mode from 651.1 W to 780.9 W. Regarding the *COP*s, the greatest increasing rate is 51.0% when the secondary air velocity is 1 m/s. Nonetheless, the *COP* improvement shrinks rapidly with the air speed from 1 m/s to 3 m/s in the two pairs of scenarios.

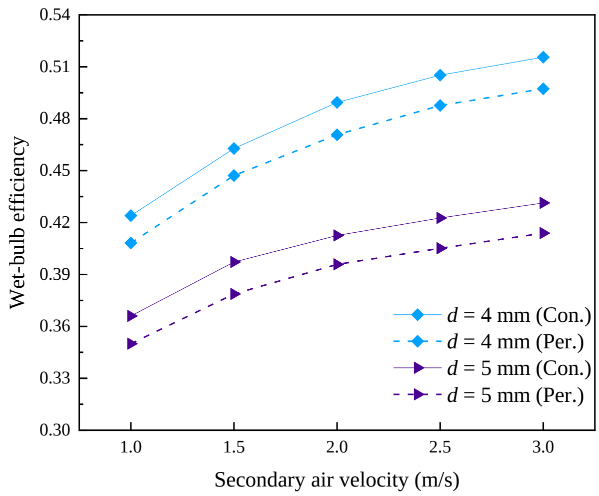

(a) Wet-bulb efficiency

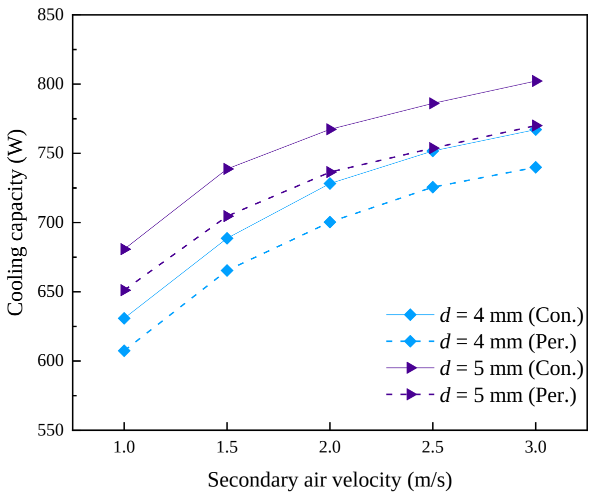

(b) Cooling capacity

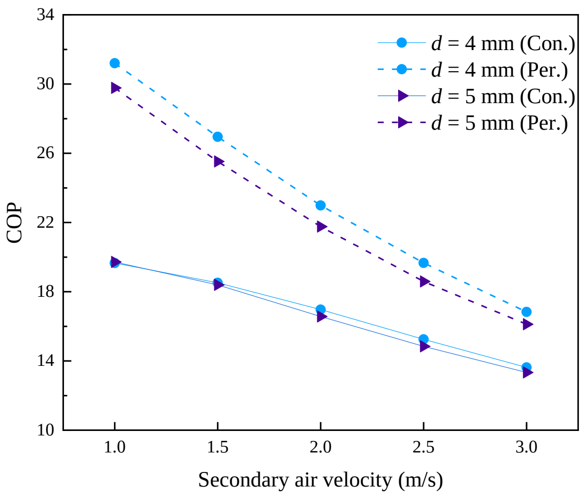

(c) COP

Fig. 6.4.3 Influence of the secondary air velocity on (a) Wet-bulb efficiency (b) Cooling capacity, and (c) COP under consistent and periodic spraying

6.5 Exergy performance

6.5.1 Exergy flow and distribution

The exergy flow variations of two example cases of the PIEC are presented in Fig. 6.5.1 under two spraying conditions. The input parameters are fixed as: $t_{p,in}$ = 30°C, $RH_{\mathrm{p,in}}$ = 40%, u_p =3 m/s, $t_{s,in}$ = 25℃, $RH_{s,in}$ = 60%, u_s = 2 m/s, d = 4 mm. For continuous spraying mode, the whole process relies on the transformation of the secondary air chemical exergy, which has three destinations: primary air thermal exergy, secondary air thermal exergy, and destruction. The former two items are the majority of the conversion. In Fig. 6.5.1(a), there is 6.42 W thermal exergy converted to the primary air. Meanwhile, the secondary air gains 1.59W thermal exergy and reaches 5.65 W, accompanied by the rapid reduction of secondary air chemical exergy from 70 W to 25.35 W. The primary air chemical exergy remains the same because there is no moisture content change.

For each cycle generated under intermittent spraying conditions, the variation trend is similar to that of traditional spraying. As shown in Fig. 6.5.1(b), the primary air acquires 3.56 Wh of thermal exergy, while the chemical exergy remains fixed. The thermal exergy of the secondary air increases slightly from 2.44 Wh to 2.77 Wh, while the chemical exergy decreases significantly from 42.02 Wh to 19.94 Wh. The mechanical exergy is to maintain the fluid flowing, which can be regarded that has no influence on the value of the air thermal and chemical exergy, which is ultimately converted to a part of destruction. In addition, it is noticed that destruction inevitably exists no matter which spraying conditions, indicating the irreversibility of the whole process. The exergy efficiency and loss ratio are discussed in the following sections with varied input air conditions.

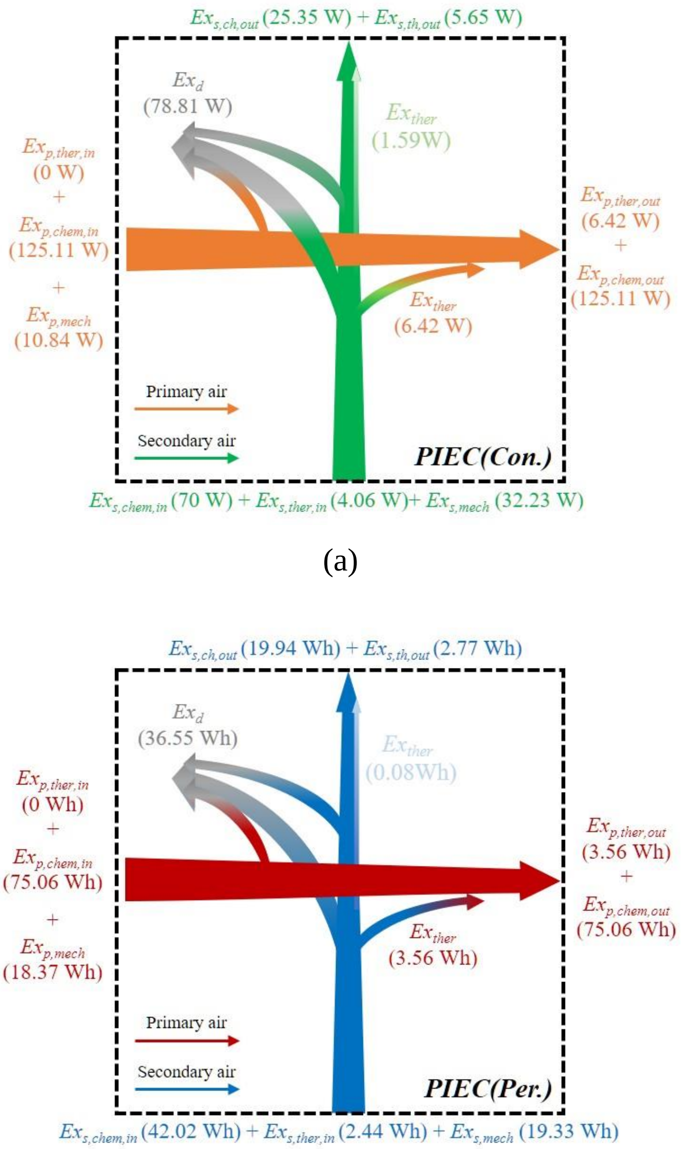

(a)

(b)

Fig. 6.5.1 Exergy flow variation of PIEC in the condition of (a) consistent spraying and (b) periodic spraying

6.5.2 Influence of the primary air inlet temperature

As mentioned in section 6.2.2, the saturation point of the inlet primary air is determined as the reference state for exergy performance calculation. The temperature and humidity ratio of the dead state increases with the growing inlet temperature. Therefore, the primary air absorption ability, the secondary air absorption ability, and the cooling ability of secondary air are relatively enhanced.

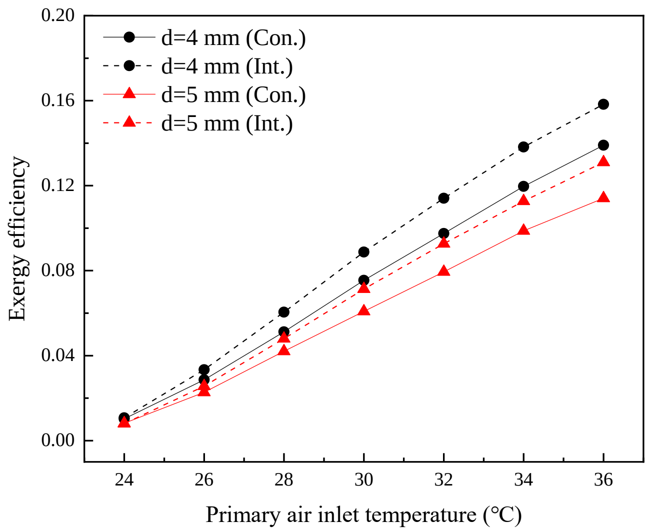

(a) Exergy efficiency

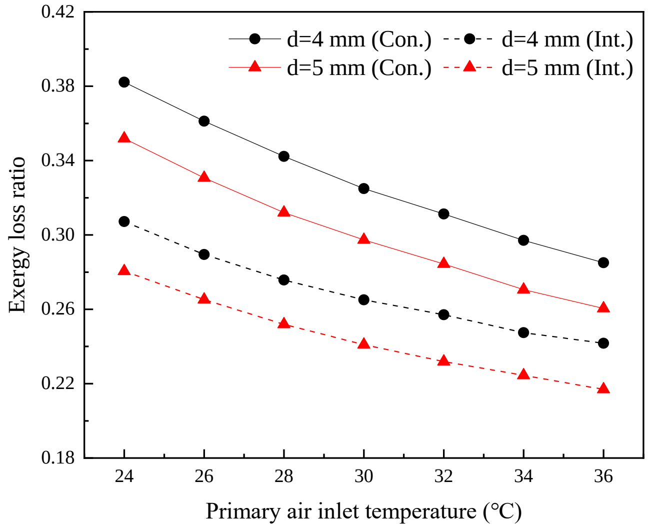

(b) Exergy loss ratio

Fig. 6.5.2 Influence of the primary air inlet temperature on (a) exergy efficiency (b) exergy loss ratio under consistent and periodic spraying

The exergy efficiency and exergy loss ratio are used as indicators to examine the exergy performance of the PIEC in two spraying modes. The impact of the primary air inlet temperature on the two indicators is shown in Fig. 6.5.2. The higher inlet temperature leads to the greater exergy efficiency, while the exergy loss ratio varies concurrently. For the exergy efficiency, the red and black dash curves are above the solid lines, indicating the enhancement by the periodic spraying. Regarding the exergy loss ratio, the scenarios of intermittent strategies achieve lower values on average and perform better than the conventional mode. The reduction of the loss ratio is 0.07 and 0.06 on average in the scenarios of d = 4 mm and d = 5 mm, respectively.

The inlet exergy of primary air and secondary air under the two spraying modes is identical, so the exergy efficiency depends on the variation extent of the other two outlet exergy. Although the primary air under traditional mode can obtain a little more exergy, the exergy consumed from the secondary side under continuous spraying is more than that under periodic spraying mode. In other words, under periodic spraying mode, the acquired primary air exergy is slightly low, but the consumed exergy from the secondary air is much lower than the traditional mode, resulting in the better exergy efficiency. For the PIEC, the humidity difference between the water membrane and secondary air decreases with the limited water evaporation during the non-spraying duration. Meanwhile, the lack of water leads to the temperature increase of the heat transfer plate, and the temperature difference between the primary air and plate is smaller. These two fewer differences diminish the exergy loss ratio in the periodic spraying cases.

6.5.3 Influence of the primary air velocity

The impact of the primary air velocity on exergy efficiency and exergy loss ratio under two spraying modes is shown in Fig. 6.5.3. The two indicators drop with the development of primary air velocity. Periodic spraying cases show higher exergy efficiency and lower exergy loss ratio compared with the traditional mode. For instance, in the pair of cases with d = 4 mm, the exergy efficiency falls from 0.08 to 0.07 with the growing speed from 1.5 m/s to 3.5 m/s, exceeding the solid line (Fig. 6.5.3(a)). Regarding the exergy loss ratio, dash lines are below the solid line in Fig. 6.5.3 (b), which means that the period spraying can reduce the exergy loss ratio. The loss ratio under consistent mode decreases from 0.39 to 0.31, while the range is 0.31 to 0.26 in the periodic conditions.

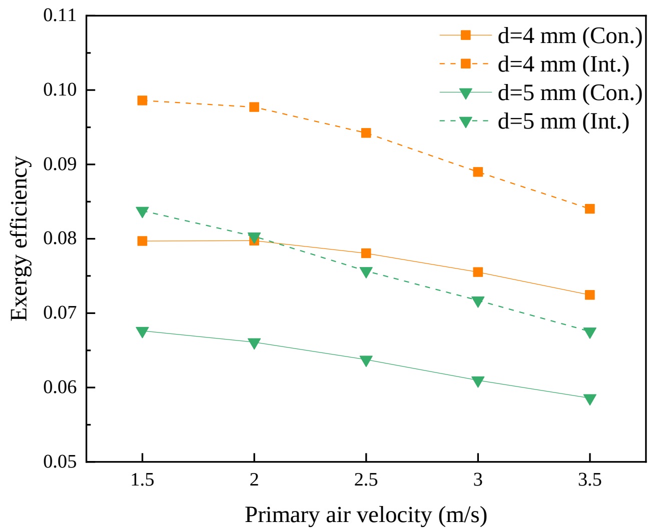

(a) Exergy efficiency

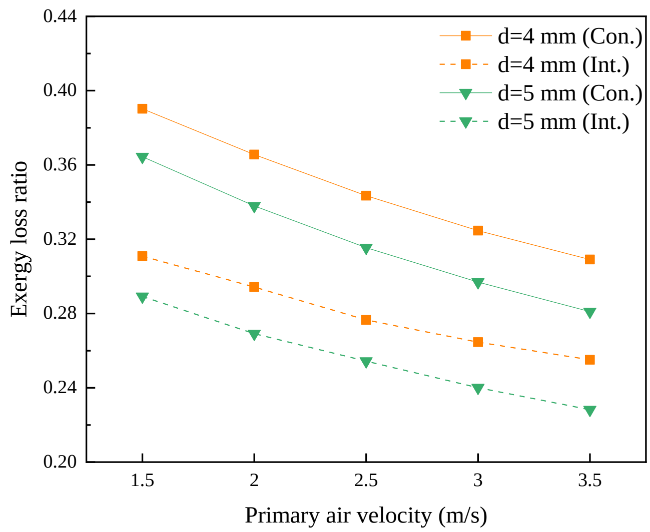

(b) Exergy loss ratio

Fig. 6.5.3 Influence of the primary air velocity on (a) exergy efficiency (b) exergy loss ratio under consistent spraying and periodic spraying

Given the same inlet temperature, the higher primary air speed leads to the larger total inlet exergy as well as the exergy destruction. The degree of the obtained exergy in the primary air is still less than that of the converted exergy from the secondary air so that the declining tendency occurs in Fig. 6.5.3(a). The increasing degree of the total inlet exergy is much greater than the exergy loss, which leads to the decreasing trend in Fig. 6.5.3(b). When the periodic spraying is implemented, the humidity gradient between the secondary air and the water film is narrowed due to the limited water reserved by PIEC in the whole cycle. Although the exergy obtained by the primary air decreases slightly, the exergy efficiency is still improved compared with continuous spraying. The periodic spraying reduces the temperature difference between the plate and the primary air as well as the moisture content difference of the secondary air, which promotes the decrease of the exergy loss ratio.

6.5.4 Influence of the secondary air velocity

Fig. 6.5.4 exhibits the impact of the secondary air velocity on exergy efficiency and exergy loss ratio under conventional spraying and recurrent spraying. It is found that the two indicators have the opposite trend with the growing secondary air speed from 1 m/s to 3 m/s. Taking the couple cases of d = 4 mm for discussion, the exergy efficiency declines from 0.084 to 0.064 and from 0.102 to 0.073 for persistent and periodic modes, respectively. The exergy loss ratio increases up to 0.197 and 0.157 with the faster speed of 3 m/s, respectively. It is found that the dash exergy efficiency curves are higher but the corresponding exergy loss ratio is lower, indicating the better performance using the periodic spraying plan.

The faster secondary air augments the entire input exergy. However, as mentioned previously, the primary air outlet temperature is limitedly reduced by increasing of secondary air speed. Therefore, the degree of exergy obtained by primary air is smaller than the exergy consumption of secondary air growth, leading to the situation that the exergy efficiency decreases all the way. In addition, the increase of the secondary air velocity can enlarge the moisture content difference between the secondary air and the water membrane, which enhances water evaporation and takes away more latent heat. The plate temperature decreases, and the gradient between it and primary air is expanded. The above two potential differences lead to a bigger exergy loss ratio.

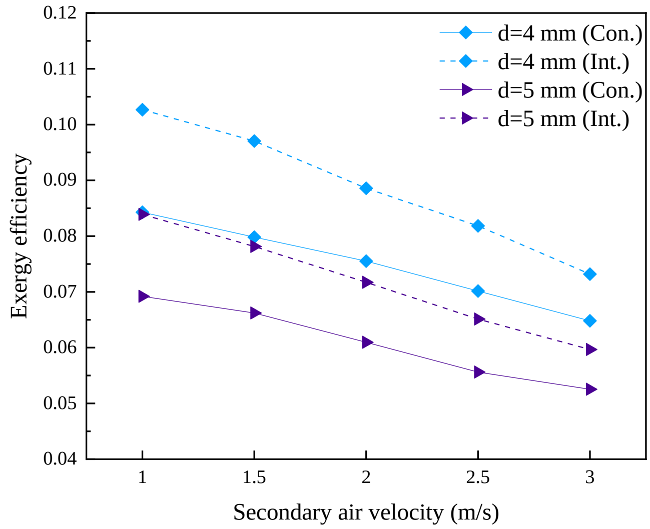

(a) exergy efficiency

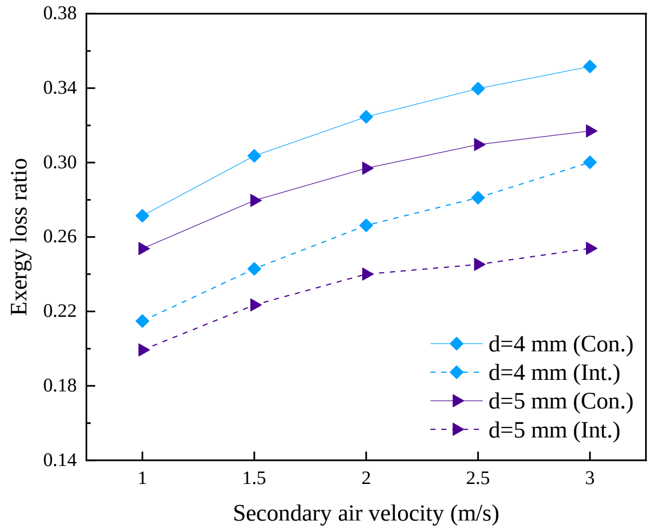

(b) exergy loss ratio

Fig. 6.5.4 Influence of the secondary air velocity on (a) exergy efficiency (b) exergy loss ratio under consistent spraying and periodic spraying

When intermittent spraying is used, the results resemble the previous two influencing factors. The moisture content potential between the water film and secondary air shrinks because of the gradual evaporation of the remaining water, and the rising plate temperature brings the closer temperature difference between the plate and the primary air. Compared with traditional spraying, the two potential differences both dwindle, thus reducing the exergy loss ratio.

6.6 Environmental performance

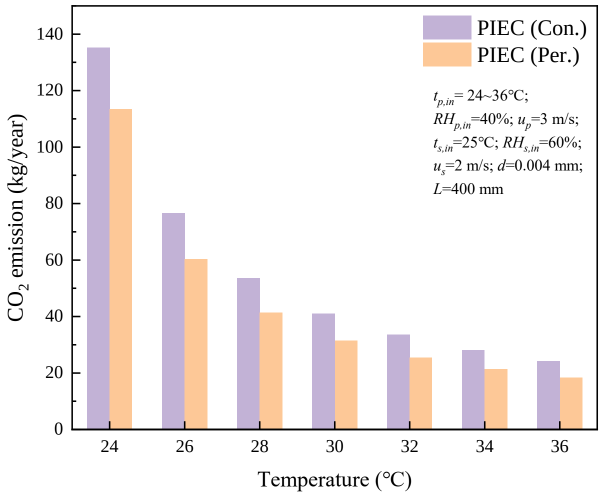

(a) *d*= 4 mm

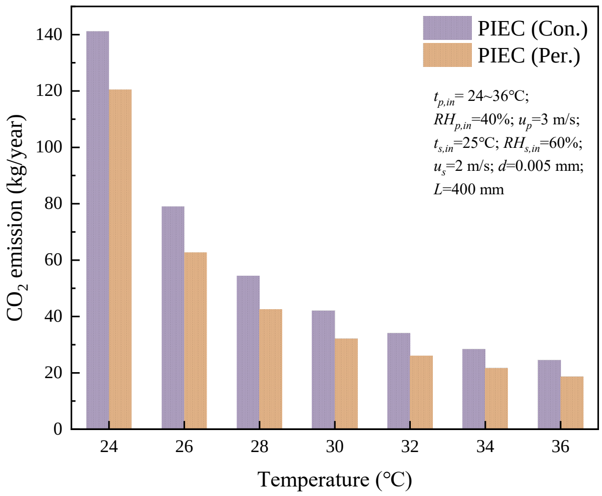

(b) *d*= 5 mm

Fig. 6.6.1 CO_2 emission of the PIEC under consistent and periodic spraying mode

As discussed in section 4.1, the PIEC has advantageous COP values that allow it to treat cooling loads with lower energy consumption under both continuous and periodic spraying modes, making it a promising technology for indirectly mitigating greenhouse gas emissions. For environmental evaluation, it is assumed that the PIEC handles the same cooling load (1 kW) under the dual spraying modes [47]. The annual operation time of the AC system is set as 1200 h. The estimated CO_2 emissions of the PIEC in the ranged primary air inlet temperature are displayed in Fig. 6.6.1.

As shown in Fig. 6.6.1, the CO_2 emission is further lessened by the periodic spraying strategy, which reduces with the growing temperature because the *COP*s of the PIEC are higher in the high inlet temperature cases, as presented in section 6.3. The annual CO_2 emission of PIEC under periodic spraying can be decreased by the range from 16% to 24.2% (d=4 mm) and from 14.6% to 23.8% (d=5 mm) compared with the consistent spraying for every kilowatt cooling load, indicating favorable environmental benefits.

6.7 Summary

This chapter presents the energy, exergy, and environmental (3E) analysis of a proposed indirect evaporative cooler incorporated with the porous layer in the secondary air channel (PIEC). The porous layer, located on the channel surface, is responsible for collecting spraying water, while the bare surface faces the primary air side. Based on simulation results from the established 3-D PIEC model, performance comparisons are conducted from 3E perspectives under traditional consistent spraying and unique periodic spraying modes. The brief performance comparison is summarized in Table 6.7.1. The main conclusions are presented as follows as well.

Table 6.7.1 Summary of 3E performance indicators under two spraying modes

Perspective	Performance indicator	The better one
Energy	η_{wb}	1

	Q_c	1
	COP	2
Exergy	η_{ex}	2
	η_{loss}	2
Environment	$m_{emission}$	2

1: Consistent spraying; 2: Intermittent spraying.

1) The consistent spraying maintains the performance constant because of the sufficient water supply. While under the intermittent spraying condition, the stored water in the wet porous media can temporarily maintain the evaporation process for air cooling and delay the temperature rise during the non-spraying period, the outlet temperature can be controlled to fluctuate within the threshold, resulting in small cycles.

2) The larger wet-bulb efficiency can be obtained with the higher primary air inlet temperature, lower primary air velocity, and faster secondary air velocity under the continuous spraying. The cooling capacity can be enhanced by the greater primary air inlet temperature and faster air speed in two channels. However, the periodic spraying plan can substantially improve the COPs by up to 58.1% among the studied cases at the cost of tiny temperature fluctuation, which can be employed in situations regarding energy saving as the priority.

3) In both consistent and periodic spraying modes, higher exergy efficiency results from greater primary air inlet temperature and lower air velocities in both channels, while a lower exergy loss ratio occurs in cases with high primary air inlet temperature, fast primary air velocity, and slow secondary air velocity. The primary air inlet

temperature is observed as the most sensitive factor to the two exergy indicators.

4) Using the periodic spraying mode can not only enhance the exergy efficiency and lessen the exergy loss ratio, but also achieve higher energy saving performance than the consistent spraying mode, which is owing to the reduction of temperature potential difference in the primary air side and humidity potential difference in the secondary air side.

5) The periodic spraying strategy further improves COPs, thereby reducing greenhouse gas emissions of the system. The annual CO2 emissions under periodic spraying mode can be reduced in the range of 16% to 24.2% and 14.6% to 23.8% compared with them in traditional consistent spraying for every kilowatt cooling load. This finding highlights the significant environmental benefits of this unique spraying mode in the context of the PIEC.

Chapter 7 Conclusions and recommendations for future work

In this thesis, a novel indirect evaporative cooler with porous material on the secondary air channel (PIEC) was newly proposed and investigated. Experimental and theoretical studies were conducted and presented. A PIEC prototype was designed and manufactured by assembling the hybrid plates made by sintering the porous nickel layer on the stainless-steel sheets, which was evaluated on a lab test rig in steady and dynamic states. The cool exhaust air from indoor environment was utilized as the secondary air to strengthen the evaporative cooling effect. The porous structure can provide spaces for the storage of spraying water, and the cooling effect can be maintained for a period of time even if the water system is paused. Therefore, the traditional continuous water spraying mode can be replaced by the intermittent spraying strategy. Then, a three-dimensional (3-D) model for the PIEC was established with the validation of the experimental data. The temperature and humidity distributions can be presented over time. The effects of essential parameters on the performance of the PIEC were analyzed as well. The cooling performance of the PIEC using different spraying strategies was predicted. Furthermore, in order to straightforwardly forecast the primary air temperature drop, wet-bulb efficiency, and the COP of the PIEC under consistent and periodic spraying modes, the regression models were proposed based on the response surface methodology. The desirability function was employed to optimize the adjustable input factors in ranges. Finally, a comprehensive comparison of the PIEC performance between the conventional consistent spraying and the newly intermittent spraying was conducted from energy, exergy, and environmental (3E) perspectives. The main findings from this thesis and the recommended future work are shown as follows.

7.1 Summary of the research findings and contributions

7.1.1 Experimental study on the performance evaluation of the PIEC

The novel PIEC was proposed, designed, and manufactured. The comprehensive experiments were conducted for a PIEC prototype in a constructed test platform at the PolyU lab. The purpose of the experiments is not only to investigate the water retention ability of the porous structure of the PIEC and explore the feasibility of using different spraying modes for the PIEC, but also to investigate the PIEC cooling performance under different spraying conditions and to collect real data for the validation of the PIEC simulation mode. The main conclusions from the experimental studies are:

1) The enhancement of wet-bulb efficiency, reaching up to 0.642 for the prototype, can be attributed to the increased primary air inlet temperature and secondary air velocity, in conjunction with the reduced primary air velocity. Under steady-state conditions of consistent spraying, the system exhibited a maximum cooling capacity of 339.1 W and a coefficient of performance (COP) of 7.2.

2) The secondary air channel surface, featuring the sintered porous layer, demonstrated a reliable water retention capacity, thereby facilitating the implementation of an intermittent spraying strategy. Moreover, the pressure drop experienced by the secondary air channels during non-spraying conditions was observed to be lower compared to that during continuous spraying mode.

3) The threshold temperatures for reactivating the water pump were established by adding 0.5℃ to the minimum temperature obtained from dynamic experiments. The overall durations and intervals for non-spraying periods were calculated based on the variation in inlet conditions. The longest interval was 2105 s, implying a potential reduction of 94.6% in pump operation time. By adopting the intermittent spraying scheme, the

average COPs of the PIEC system were enhanced by 117.5%, with the highest COP reaching 17.3.

4) Taking into account the fluctuating inlet air properties under actual climatic conditions, the PIEC can be strategically positioned before a supplementary cooling coil as pre-cooling equipment for fresh air supply. This configuration can ensure that the AC system reliably delivers air at a satisfactory temperature to maintain the indoor environment while achieving energy-saving objectives.

7.1.2 Dynamic modeling and validation of the PIEC with consistent and intermittent spraying modes

The 3-D model was established for the proposed PIEC with experimental validations. This model can predict the cooling performance under the consistent and periodic spraying conditions, and the temperature and humidity distributions can be obtained over time. The effects of essential parameters were investigated as well. The main conclusions from the simulation study are:

1) The dynamic variation process of a temperature cycle can be categorized into three stages, and the optimal wet-bulb efficiency occurs at the end of the first stage. The greater wet-bulb efficiency due to higher primary inlet air temperature produces greater secondary air velocity, and slower primary air velocity. Furthermore, narrowing down channel height and using the material with larger porosity and pore diameter are also conducive to improving the wet-bulb efficiency.

2) According to the simulation and experimental studies of the PIEC, periodic spraying strategies are determined. A spraying time of 120 s is conducted at the beginning of each cycle to supplement liquid water, and the remaining time is the interval for the

non-spraying period. In the studied ranges, higher primary inlet air temperature and faster secondary airspeed shrink the interval significantly.

3) The longest and shortest non-spraying intervals are identified as 2410 s and 1270 s, corresponding to 95.2% and 91.4% reduction of water pump working time compared with conventional consistent water spraying mode. Meanwhile, the intermittent water spraying leads to the noticeable improvement of COP of the PIEC system.

7.1.3 Study on the regression model and optimization of the PIEC

In this section, the response surface methodology is employed to develop the regression model of the three essential responses under traditional consistent spraying and novel periodic spraying conditions so that the performance of the PIEC can be predicted in a more straightforward approach. The BBD matrix is generated, and each case is calculated based on the established PIEC model. The effect of single and controllable interactive factors on the responses are presented. Then, the optimizations of the adjustable parameters are conducted based on the maximized desirability considering wet-bulb efficiency, cooling capacity, and *COP* under each spraying strategy. The main conclusions from the study on the RSM-based regression models are:

1) The sensitivity of the input factors changes in the different responses. The primary air temperature and velocity are more sensitive for the response of primary air temperature drop and wet-bulb efficiency under the consistent and intermittent spraying conditions, while the primary air and secondary air relative humidity are more sensitive than the other three inputs for the response of COP under the two spraying modes.

2) The response value may not be unlimitedly improved by changing the factors to maximum or minimum value based on the variation trends of the single factor. The

interactive factors need to be controlled simultaneously for getting the better performance. The most significant *COP* value under the consistent spraying is achieved given the adjustable conditions of v_p= 3.05 m/s v_s= 1.11 m/s and $t_{s,in}$= 24℃, v_s= 0.95 m/s. While the *COP* reaches maximum when v_p= 1.5 m/s, v_s= 0.5 m/s and $t_{s,in}$= 24℃, v_s= 0.5 m/s in the intermittent spraying mode.

3) The adjustable input parameters are optimized as v_p= 1.5 m/s, v_s= 1.2 m/s, $t_{s,in}$= 24℃ and v_p= 1.5 m/s, v_s= 1.1 m/s, $t_{s,in}$= 24℃ for consistent and periodic spraying modes, respectively, which achieves the highest desirability considering the maximized primary air temperature drop, wet-bulb efficiency, and *COP*.

7.1.4 Energy, exergy, and environmental analysis on the PIEC system under the dual spraying modes

In this work, the energy, exergy, and environmental (3E) evaluation is carried out and compared for the PIEC system under consistent spraying and intermittent spraying. This comparison can demonstrate the characteristics of performance for each spray scheme, especially highlighting the advantages of PIEC in the intermittent spraying mode. The main conclusions from the study on the 3E performance comparison between the two spraying modes are:

1) The consistent spraying maintains the performance constant because of the sufficient water supply. During the non-spraying period, the stored water in the wet porous media can temporarily maintain the evaporation process for air cooling and delay the temperature rise. Under the intermittent spraying condition, the outlet temperature can be controlled to fluctuate within the threshold and generate small cycles.

2) The larger wet-bulb efficiency can be obtained with the higher primary air inlet

temperature, lower primary air velocity, and faster secondary air velocity under the continuous spraying. The cooling capacity can be enhanced by the greater primary air inlet temperature and faster air speed in two channels. However, the periodic spraying plan can substantially improve the *COP*s by up to 58.1% among the studied cases at the cost of tiny temperature fluctuation, which can be employed in situations regarding energy saving as the priority.

3) In both two spraying modes, the greater primary air inlet temperature and lower air velocities in two channels can contribute to a higher exergy efficiency, while the lower exergy loss ratio happens in the cases with low primary air inlet temperature, fast primary air velocity, and slow secondary air velocity. Furthermore, using the periodic spraying mode can not only enhance the exergy efficiency and lessen the exergy loss ratio, but also achieve higher energy saving performance than the consistent spraying mode, which is owing to the reduction of temperature potential difference in the primary air side and humidity potential difference in the secondary air side.

4) The periodic spraying strategy further improves *COP*s, thereby reducing greenhouse gas emissions of the system. The annual CO_2 emissions under periodic spraying mode can be reduced in the range of 16% to 24.2% and 14.6% to 23.8% compared with them under traditional consistent spraying for every kilowatt cooling load. This finding highlights the significant environmental benefits of this unique spraying mode in the context of the PIEC.

7.2 Recommendations for future work

Although this thesis has made some contribution to the understanding of the plate-type cross-flow PIEC and validated its feasibility to cool the air under consistent spraying and periodic spraying modes, further research may enable the large-scale applications. Future work can be conducted as follows:

1) The hybrid porous plates used for experiments in this thesis are non-standard customized, and the size of the plate is limited due to the current manufacturing craft, which leads to the higher cost of the PIEC compared with the normal IEC available in the market, although the two metal materials are easily available. Therefore, future research should focus on finding materials with lower costs and simplified manufacturing processes. The economic analysis can be carried out once the initial investment of the PIEC is reduced. The reduced and acceptable cost is the important premise of further commercialization and application.

2) At present, intermittent spraying is implemented with a temperature rise threshold of 0.5℃ and stable input parameters. However, it is noted that the outdoor environment is subject to fluctuations and the temperature rise threshold may vary with various application scenarios and end-user requirements. As such, further research can be carried out to explore the solution and negotiate the variation of fresh air, supply air temperature rise, energy saving, and customer demands. If this novel PIEC can be widely used in the future, the dynamic carbon emission coefficient may be considered for a more comprehensive analysis as well.

3) Water used in experiments was of good quality and in relatively small quantity with no observed impact on the porous media. However, However, the presence of water-soluble calcium and magnesium compounds may influence the long-term performance of the porous layer, especially in regions with poor water quality that are more susceptible to scaling. Scaling can heighten thermal resistance during heat transfer and potentially clog or fill the pores, diminishing the water storage capacity of the porous

medium. Consequently, further investigation is necessary to explore the long-term effects of different water qualities on the porous zone.

4) In this thesis, exhaust air from indoor spaces, which is relatively clean and maintains a stable condition, was employed as the source of secondary air. Nevertheless, when outdoor air is used as secondary air, some physical impurities and potential microorganisms in the air may generally accumulate in the pores, ultimately affecting the performance of the porous media. Therefore, the influence of the quality of the secondary air on the PIEC performance should also be in long-term monitoring.

Appendix

Table A1 The matrix based on BBD

F_1	F_2	F_3	F_4	F_5	R_1	R_2	R_3	R_4	R_5	R_6
$t_{p,in}$	v_p	t_s	$RH_{s,in}$	v_s	Δt_{p_con}	$\eta_{wb,con\_}$	COP_{con}	$\Delta t_{p,int}$	η_{wb_int}	COP_{int}
℃	m/s	℃	%	m/s						
28	2.5	25	0.5	1	23.57	0.44	17.53	23.82	0.41	28.53
32	2.5	25	0.5	1.5	24.60	0.52	24.73	24.85	0.50	36.99
24	2.5	25	0.5	0.5	22.40	0.26	7.50	22.65	0.22	12.75
32	2.5	24	0.5	1	24.70	0.49	28.53	24.95	0.47	47.39
24	1.5	25	0.5	1	21.29	0.44	7.51	21.54	0.40	13.32
24	2.5	25	0.4	1	21.31	0.34	10.74	21.56	0.31	16.79
32	2.5	25	0.5	0.5	26.45	0.39	25.54	26.70	0.37	49.10
28	2.5	25	0.5	1	23.57	0.44	17.53	23.82	0.41	28.53

28	3.5	25	0.6	1	24.82	0.37	15.13	25.07	0.34	22.00
28	3.5	24	0.5	1	23.94	0.37	19.32	24.19	0.35	28.47
28	3.5	25	0.4	1	23.82	0.35	19.90	24.07	0.33	29.22
28	2.5	24	0.5	1.5	22.66	0.49	18.02	22.91	0.46	26.70
28	1.5	25	0.5	0.5	23.34	0.46	15.43	23.59	0.43	36.03
28	2.5	25	0.6	0.5	24.94	0.36	14.23	25.19	0.33	26.48
24	2.5	25	0.5	1.5	21.66	0.38	8.00	21.91	0.34	11.14
28	2.5	26	0.6	1	24.66	0.43	13.20	24.91	0.40	21.28
32	3.5	25	0.5	1	26.30	0.40	26.87	26.55	0.38	40.21
28	2.5	25	0.5	1	23.57	0.44	17.53	23.82	0.41	28.53
28	3.5	26	0.5	1	24.70	0.35	15.72	24.95	0.33	22.80
28	1.5	24	0.5	1	21.77	0.57	17.05	22.02	0.54	31.77
28	2.5	25	0.5	1	23.57	0.44	17.53	23.82	0.41	28.53

24	3.5	25	0.5	1	22.27	0.28	8.34	22.52	0.24	11.23
32	2.5	25	0.4	1	24.58	0.47	29.03	24.83	0.45	47.93
28	2.5	25	0.6	1.5	23.82	0.49	14.10	24.07	0.46	20.74
28	2.5	26	0.4	1	23.38	0.42	18.28	23.63	0.39	29.67
28	2.5	24	0.6	1	23.67	0.46	17.09	23.92	0.43	27.98
28	3.5	25	0.5	1.5	23.92	0.40	16.92	24.17	0.38	23.13
28	2.5	24	0.5	0.5	24.06	0.36	18.30	24.31	0.34	34.47
28	2.5	25	0.4	0.5	24.00	0.34	18.58	24.25	0.32	34.81
28	1.5	26	0.5	1	22.98	0.54	13.77	23.23	0.51	25.38
32	2.5	26	0.5	1	25.64	0.48	24.90	25.89	0.46	41.23
28	2.5	25	0.4	1.5	22.49	0.46	18.60	22.74	0.44	27.40
28	2.5	24	0.4	1	22.52	0.43	21.62	22.77	0.41	35.39
24	2.5	24	0.5	1	21.41	0.37	10.35	21.66	0.33	16.19

28	1.5	25	0.4	1	21.64	0.54	17.43	21.89	0.51	32.24
32	1.5	25	0.5	1	23.38	0.61	23.35	23.63	0.59	43.76
28	2.5	25	0.5	1	23.57	0.44	17.53	23.82	0.41	28.53
28	2.5	26	0.5	0.5	25.12	0.31	13.40	25.37	0.28	24.73
24	2.5	25	0.6	1	22.47	0.33	6.10	22.72	0.28	8.91
28	1.5	25	0.6	1	23.11	0.57	13.39	23.36	0.54	24.91
28	1.5	25	0.5	1.5	21.96	0.59	13.83	22.21	0.57	22.14
28	3.5	25	0.5	0.5	25.52	0.24	13.55	25.77	0.22	21.18
32	2.5	25	0.6	1	25.77	0.49	24.37	26.02	0.47	40.60
28	2.5	26	0.5	1.5	23.64	0.47	14.75	23.89	0.44	21.59
24	2.5	26	0.5	1	22.37	0.30	6.52	22.62	0.26	9.58
28	2.5	25	0.5	1	23.57	0.44	17.53	23.82	0.41	28.53

Note:

F: factor; R: response.

References

[1] X. Liu, X. Liu, Y. Jiang, T. Zhang, and B. Hao, "PEDF (photovoltaics, energy storage, direct current, flexibility), a power distribution system of buildings for grid decarbonization: Definition, technology review, and application," *CSEE Journal of Power and Energy Systems,* pp. 1-18, 2022.

[2] G. G. A. f. Buildings and Construction, "International Energy Agency and the United Nations Environment Program: 2019 Global Status Report for Buildings and Construction: Towards a Zero-Emission, Efficient and Resilient Buildings and Construction Sector," ed: United Nations Environment Program Nairobi, Kenya, 2019.

[3] H. Yu *et al.*, "Prioritizing urban planning factors on community energy performance based on GIS-informed building energy modeling," *Energy and Buildings,* vol. 249, p. 111191, 2021/10/15/ 2021.

[4] Z. Liu, Y. Liu, B.-J. He, W. Xu, G. Jin, and X. Zhang, "Application and suitability analysis of the key technologies in nearly zero energy buildings in China," *Renewable and Sustainable Energy Reviews,* vol. 101, pp. 329-345, 2019/03/01/ 2019.

[5] N. Zhou, N. Khanna, W. Feng, J. Ke, and M. Levine, "Scenarios of energy efficiency and CO2 emissions reduction potential in the buildings sector in China to year 2050," *Nature Energy,* vol. 3, no. 11, pp. 978-984, 2018/11/01 2018.

[6] (2020). *Hong Kong Energy End-use Data 2020*.

[7] S. Abdullah *et al.*, "Technological development of evaporative cooling systems and its integration with air dehumidification processes: A review," *Energy and Buildings,* vol. 283, p. 112805, 2023/03/15/ 2023.

[8] G. Zhu, T. Wen, Q. Wang, and X. Xu, "A review of dew-point evaporative cooling: Recent advances and future development," *Applied Energy,* vol. 312, p. 118785, 2022/04/15/ 2022.

[9] J. Lin and K. J. Chua, "Fundamental Analysis of Dew-Point Evaporative Cooler," in *Indirect Dew-Point Evaporative Cooling: Principles and Applications*, J. Lin and K. J. Chua, Eds. Cham: Springer International Publishing, 2023, pp. 79-106.

[10] W. H. Carrier, "Apparatus for treating air," ed: Google Patents, 1906.

[11] R. H. Mohammed, M. El-Morsi, and O. Abdelaziz, "Indirect evaporative cooling for buildings: A comprehensive patents review," *Journal of Building Engineering,* vol. 50, p. 104158, 2022/06/01/ 2022.

[12] Y. Min, Y. Chen, and H. Yang, "Numerical study on indirect evaporative coolers considering condensation: A thorough comparison between cross flow and counter flow," *International Journal of Heat and Mass Transfer*, vol. 131, pp. 472-486, 2019/03/01/ 2019.

[13] Y. M. Xuan, F. Xiao, X. F. Niu, X. Huang, and S. W. Wang, "Research and applications of evaporative cooling in China: A review (II)—Systems and equipment," *Renewable and Sustainable Energy Reviews,* vol. 16, no. 5, pp. 3523-3534, 2012/06/01/ 2012.

[14] Y. Chen, Y. Luo, and H. Yang, "Fresh Air Pre-cooling and Energy Recovery by Using Indirect Evaporative Cooling in Hot and Humid Region – A Case Study in Hong Kong," *Energy Procedia,* vol. 61, pp. 126-130, 2014/01/01/ 2014.

[15] S. Pedrazzi, G. Allesina, and A. Muscio, "Indirect evaporative cooling by sub-roof forced ventilation to counter extreme heat events," *Energy and Buildings,* vol. 229, p. 110491, 2020/12/15/ 2020.

[16] H. Yang, W. Shi, Y. Chen, and Y. Min, "Research development of indirect evaporative cooling technology: An updated review," *Renewable and Sustainable Energy Reviews,* vol. 145, p. 111082, 2021/07/01/ 2021.

[17] D. Pandelidis *et al.*, "Water desalination through the dewpoint evaporative system," *Energy Conversion and Management,* vol. 229, p. 113757, 2021/02/01/ 2021.

[18] Q. Chen, M. Burhan, M. W. Shahzad, D. Ybyraiymkul, F. H. Akhtar, and K. C. Ng, "Simultaneous production of cooling and freshwater by an integrated indirect evaporative cooling and humidification-dehumidification desalination cycle," *Energy Conversion and Management,* vol. 221, p. 113169, 2020/10/01/ 2020.

[19] H. M. U. Raza, M. Sultan, M. Bahrami, and A. A. Khan, "Experimental investigation of evaporative cooling systems for agricultural storage and livestock air-conditioning in Pakistan," *Building simulation,* vol. 14, no. 3, pp. 617-631, 2021.

[20] J. Lin, H. N. Chu, K. Thu, M. Wojtala, F. Gao, and K. J. Chua, "Novel battery thermal management via scalable dew-point evaporative cooling," *Energy Conversion and Management,* vol. 283, p. 116948, 2023/05/01/ 2023.

[21] Y. M. Xuan, F. Xiao, X. F. Niu, X. Huang, and S. W. Wang, "Research and application of evaporative cooling in China: A review (I) – Research," *Renewable and Sustainable Energy Reviews,* vol. 16, no. 5, pp. 3535-3546, 2012/06/01/ 2012.

[22] S. Chakraborty, D. Vernon, A. Jha, and V. Narayanan, "Performance characterization of M-cycle indirect evaporative cooler and heat recovery ventilator for commercial buildings – Experiments and model," *Energy and Buildings,* vol. 281, p. 112762, 2023/02/15/ 2023.

[23] Y. Chen, H. Yan, and H. Yang, "Comparative study of on-off control and novel high-low control of regenerative indirect evaporative cooler (RIEC)," *Applied Energy,* vol. 225, pp. 233-243, 2018/09/01/ 2018.

[24] B. Riangvilaikul and S. Kumar, "Numerical study of a novel dew point evaporative cooling system," *Energy and Buildings,* vol. 42, no. 11, pp. 2241-2250, 2010/11/01/ 2010.

[25] D. Pandelidis and S. Anisimov, "Numerical analysis of the heat and mass transfer processes in selected M-Cycle heat exchangers for the dew point evaporative cooling," *Energy Conversion and Management,* vol. 90, pp. 62-83, 2015/01/15/ 2015.

[26] J. Lin, K. Thu, T. D. Bui, R. Z. Wang, K. C. Ng, and K. J. Chua, "Study on dew point evaporative cooling system with counter-flow configuration," *Energy Conversion and Management,* vol. 109, pp. 153-165, 2016/02/01/ 2016.

[27] Y. Chen, Y. Luo, and H. Yang, "A simplified analytical model for indirect evaporative cooling considering condensation from fresh air: Development and application," *Energy and Buildings,* vol. 108, pp. 387-400, 2015/12/01/ 2015.

[28] X. Cui, K. J. Chua, M. R. Islam, and K. C. Ng, "Performance evaluation of an indirect pre-cooling evaporative heat exchanger operating in hot and humid climate," *Energy Conversion and Management,* vol. 102, pp. 140-150, 2015/09/15/ 2015.

[29] G. Zhu, W. Chen, D. Zhang, and T. Wen, "Performance evaluation of counter flow dew-point evaporative cooler with a three-dimensional numerical model," *Applied Thermal Engineering,* vol. 219, p. 119483, 2023/01/25/ 2023.

[30] J. Lin *et al.*, "Unsteady-state analysis of a counter-flow dew point evaporative cooling system," *Energy,* vol. 113, pp. 172-185, 2016/10/15/ 2016.

[31] W. Li, Y. Li, W. Shi, and J. Lu, "Energy and exergy study on indirect evaporative cooler used in exhaust air heat recovery," *Energy,* vol. 235, p. 121319, 2021/11/15/ 2021.

[32] J. Castillo-González, F. Comino, F. J. Navas-Martos, and M. Ruiz de Adana, "Manufacturing and experimental analysis of a dew-point indirect evaporative cooler using fused deposition modelling 3D printing and polymeric materials," *Applied Thermal Engineering,* vol. 230, p. 120683, 2023/07/25/ 2023.

[33] A. E. Kabeel and M. Abdelgaied, "Numerical and experimental investigation of a novel configuration of indirect evaporative cooler with internal baffles," *Energy Conversion and Management,* vol. 126, pp. 526-536, 2016/10/15/ 2016.

[34] G. Zhu, T.-T. Chow, and C. K. Lee, "Performance analysis of counter-flow regenerative heat and mass exchanger for indirect evaporative cooling based on data-driven model," *Energy and Buildings,* vol. 155, pp. 503-512, 2017/11/15/ 2017.

[35] A. Pakari and S. Ghani, "Regression models for performance prediction of counter flow dew point evaporative cooling systems," *Energy Conversion and Management,* vol. 185, pp. 562-573, 2019/04/01/ 2019.

[36] Y. Wan, A. Soh, Y. Shao, X. Cui, Y. Tang, and K. J. Chua, "Numerical study and correlations for heat and mass transfer coefficients in indirect evaporative coolers with condensation based on orthogonal test and CFD approach," *International Journal of Heat and Mass Transfer,* vol. 153, p. 119580, 2020/06/01/ 2020.

[37] N. Nemati, A. Omidvar, and B. Rosti, "Performance evaluation of a novel hybrid cooling system combining indirect evaporative cooler and earth-air heat exchanger," *Energy,* vol. 215, p. 119216, 2021/01/15/ 2021.

[38] Y. Chen, H. Yang, and Y. Luo, "Investigation on solar assisted liquid desiccant dehumidifier and evaporative cooling system for fresh air treatment," *Energy,* vol. 143, pp. 114-127, 2018/01/15/ 2018.

[39] Y. Wan, Z. Huang, A. Soh, and K. Jon Chua, "On the performance study of a hybrid indirect evaporative cooling and latent-heat thermal energy storage system under commercial operating conditions," *Applied Thermal Engineering,* vol. 221, p. 119902, 2023/02/25/ 2023.

[40] X. C. Guo and T. S. Zhao, "A parametric study of an indirect evaporative air cooler," *International Communications in Heat and Mass Transfer,* vol. 25, no. 2, pp. 217-226, 1998/02/01/ 1998.

[41] C. Zhan, X. Zhao, S. Smith, and S. B. Riffat, "Numerical study of a M-cycle cross-flow heat exchanger for indirect evaporative cooling," *Building and Environment,* vol. 46, no. 3, pp. 657-668, 2011/03/01/ 2011.

[42] D. Pandelidis, S. Anisimov, K. Rajski, E. Brychcy, and M. Sidorczyk, "Performance comparison of the advanced indirect evaporative air coolers," *Energy,* vol. 135, pp. 138-152, 2017/09/15/ 2017.

[43] W. Shi, Y. Min, Y. Chen, and H. Yang, "Development of a three-dimensional numerical model of indirect evaporative cooler incorporating with air dehumidification," *International Journal of Heat and Mass Transfer,* vol. 185, p. 122316, 2022/04/01/ 2022.

[44] Y. Min, Y. Chen, H. Yang, and C. Guo, "Characteristics of primary air condensation in indirect evaporative cooler: Theoretical analysis and visualized validation," *Building and Environment,* vol. 174, p. 106783, 2020/05/01/ 2020.

[45] C. Guo, Q. Liu, B. Zheng, Y. You, and Y. Li, "Development of model based on condensation area ratio and effect on heat transfer capacity of indirect evaporative cooling," *Applied Thermal Engineering,* vol. 164, p. 114557, 2020/01/05/ 2020.

[46] R. Kousar, M. Ali, M. K. Amjad, and W. Ahmad, "Energy, Exergy, Economic, Environmental (4Es) comparative performance evaluation of dewpoint evaporative cooler configurations," *Journal of Building Engineering,* vol. 45, p. 103466, 2022/01/01/ 2022.

[47] H. Zhang, H. Ma, and S. Ma, "Energy, exergy, economic and environmental analysis of an indirect evaporative cooling integrated with liquid dehumidification," *Energy,* vol. 253, p. 124147, 2022/08/15/ 2022.

[48] J.-Y. Park, B.-J. Kim, S.-Y. Yoon, Y.-S. Byon, and J.-W. Jeong, "Experimental analysis of dehumidification performance of an evaporative cooling-assisted internally cooled liquid desiccant dehumidifier," *Applied Energy,* vol. 235, pp. 177-185, 2019/02/01/ 2019.

[49] B. Zhou, J. Lv, M. Zhu, L. Wang, L. Liang, and Q. Chen, "Simulation study of a thin membrane inclined automatic wicking dew-point evaporative cooling device," *Journal of Building Engineering,* vol. 72, p. 106601, 2023/08/01/ 2023.

[50] T. R. Kiran and S. P. S. Rajput, "An effectiveness model for an indirect evaporative cooling (IEC) system: Comparison of artificial neural networks (ANN), adaptive neuro-fuzzy inference system (ANFIS) and fuzzy inference system (FIS) approach," *Applied Soft Computing,* vol. 11, no. 4, pp. 3525-3533, 2011/06/01/ 2011.

[51] W. Shi, X. Ma, Y. Gu, Y. Min, and H. Yang, "Indirect evaporative cooling maps of China: Optimal and quick performance identification based on a data-driven model," *Energy Conversion and Management,* vol. 268, 2022.

[52] Y. Min, Y. Chen, and H. Yang, "A statistical modeling approach on the performance prediction of indirect evaporative cooling energy recovery systems," *Applied Energy,* vol. 255, p. 113832, 2019/12/01/ 2019.

[53] S. Delfani, J. Esmaeelian, H. Pasdarshahri, and M. Karami, "Energy saving potential of an indirect evaporative cooler as a pre-cooling unit for mechanical cooling systems in Iran," *Energy and Buildings,* vol. 42, no. 11, pp. 2169-2176, 2010/11/01/ 2010.

[54] Y. Min, Y. Chen, W. Shi, and H. Yang, "Applicability of indirect evaporative cooler for energy recovery in hot and humid areas: Comparison with heat recovery wheel," *Applied Energy,* vol. 287, 2021.

[55] X. Cui, L. Sun, S. Zhang, and L. Jin, "On the study of a hybrid indirect evaporative pre-cooling system for various climates," *Energies (Basel),* vol. 12, no. 23, p. 4419, 2019.

[56] W.-Y. Li, Y.-C. Li, L.-y. Zeng, and J. Lu, "Comparative study of vertical and horizontal indirect evaporative cooling heat recovery exchangers," *International Journal of Heat and Mass Transfer,* vol. 124, pp. 1245-1261, 2018/09/01/ 2018.

[57] D. Pandelidis *et al.*, "Performance study of a novel dew point evaporative cooler in the climate of central Europe using building simulation tools," *Building and Environment,* vol. 181, p. 107101, 2020/08/15/ 2020.

[58] A. Pacak, B. Baran, K. Sierpowski, Z. Malecha, and D. Pandelidis, "Application of computational fluid dynamics (CFD) methods to analyze energy efficiency of indirect evaporative coolers," *International Communications in Heat and Mass Transfer,* vol. 143, p. 106727, 2023/04/01/ 2023.

[59] W. Li, W. Shi, J. Wang, Y. Li, and J. Lu, "Experimental study of a novel household exhaust air heat pump enhanced by indirect evaporative cooling," *Energy and Buildings,* vol. 236, p. 110808, 2021/04/01/ 2021.

[60] Y. Zhang, H. Zhang, H. Yang, Y. Chen, and C. W. Leung, "Counter-crossflow indirect evaporative cooling-assisted liquid desiccant dehumidifier: Model development and parameter analysis," *Applied Thermal Engineering,* vol. 217, p. 119231, 2022/11/25/ 2022.

[61] T. R. Tulsidasani, R. L. Sawhney, S. P. Singh, and M. S. Sodha, "Recent research on an indirect evaporative cooler (IEC) Part 1: optimization of the COP," *International journal of energy research,* vol. 21, no. 12, pp. 1099-1108, 1997.

[62] F. Wang, T. Sun, X. Huang, Y. Chen, and H. Yang, "Experimental research on a novel porous ceramic tube type indirect evaporative cooler," *Applied Thermal Engineering,* vol. 125, pp. 1191-1199, 2017/10/01/ 2017.

[63] T. Sun, X. Huang, Y. Qu, F. Wang, and Y. Chen, "Theoretical and experimental study on heat and mass transfer of a porous ceramic tube type indirect evaporative cooler," *Applied Thermal Engineering,* vol. 173, p. 115211, 2020/06/05/ 2020.

[64] T. Sun, T. Tang, C. Yang, W. Yan, X. Cui, and J. Chu, "Cooling performance and optimization of a tubular indirect evaporative cooler based on response surface methodology," *Energy and Buildings*, vol. 285, p. 112880, 2023/04/15/ 2023.

[65] F. Gao, K. Thu, S. Wang, F. Zhao, J. Lin, and K. Wu, "Numerical investigation of a novel tubular dew-point evaporative cooler," *Applied Thermal Engineering,* vol. 223, p. 120064, 2023/03/25/ 2023.

[66] S. B. Riffat and J. Zhu, "Mathematical model of indirect evaporative cooler using porous ceramic and heat pipe," *Applied Thermal Engineering,* vol. 24, no. 4, pp. 457-470, 2004/03/01/ 2004.

[67] R. Boukhanouf, O. Amer, H. Ibrahim, and J. Calautit, "Design and performance analysis of a regenerative evaporative cooler for cooling of buildings in arid climates," *Building and Environment,* vol. 142, pp. 1-10, 2018/09/01/ 2018.

[68] K. Rajski, J. Danielewicz, and E. Brychcy, "Performance evaluation of a gravity-assisted heat pipe-based indirect evaporative cooler," *Energies (Basel),* vol. 13, no. 1, p. 200, 2020.

[69] D. Pandelidis *et al.*, "Performance analysis of rotary indirect evaporative air coolers," *Energy Conversion and Management,* vol. 244, p. 114514, 2021/09/15/ 2021.

[70] R. Chengqin and Y. Hongxing, "An analytical model for the heat and mass transfer processes in indirect evaporative cooling with parallel/counter flow configurations," *International Journal of Heat and Mass Transfer,* vol. 49, no. 3, pp. 617-627, 2006/02/01/ 2006.

[71] X. Zhao, S. Liu, and S. B. Riffat, "Comparative study of heat and mass exchanging materials for indirect evaporative cooling systems," *Building and Environment,* vol. 43, no. 11, pp. 1902-1911, 2008/11/01/ 2008.

[72] Y. Chen, H. Yang, and Y. Luo, "Parameter sensitivity analysis and configuration optimization of indirect evaporative cooler (IEC) considering condensation," *Applied Energy,* vol. 194, pp. 440-453, 2017/05/15/ 2017.

[73] S. De Antonellis, C. M. Joppolo, P. Liberati, S. Milani, and L. Molinaroli, "Experimental analysis of a cross flow indirect evaporative cooling system," *Energy and Buildings,* vol. 121, pp. 130-138, 2016/06/01/ 2016.

[74] J. Lee and D.-Y. Lee, "Experimental study of a counter flow regenerative evaporative cooler with finned channels," *International Journal of Heat and Mass Transfer,* vol. 65, pp. 173-179, 2013/10/01/ 2013.

[75] S. De Antonellis, L. Cignatta, C. Facchini, and P. Liberati, "Effect of heat exchanger plates geometry on performance of an indirect evaporative cooling system," *Applied Thermal Engineering,* vol. 173, p. 115200, 2020/06/05/ 2020.

[76] O. Khalid, M. Ali, N. A. Sheikh, H. M. Ali, and M. Shehryar, "Experimental analysis of an improved Maisotsenko cycle design under low velocity conditions," *Applied Thermal Engineering,* vol. 95, pp. 288-295, 2016/02/25/ 2016.

[77] S. Bolotin, B. Vager, and V. Vasilijev, "Comparative analysis of the cross-flow indirect evaporative air coolers," *International Journal of Heat and Mass Transfer,* vol. 88, pp. 224-235, 2015/09/01/ 2015.

[78] A. E. Kabeel, M. M. Bassuoni, and M. Abdelgaied, "Experimental study of a novel integrated system of indirect evaporative cooler with internal baffles and evaporative condenser," *Energy Conversion and Management,* vol. 138, pp. 518-525, 2017/04/15/ 2017.

[79] Y. Zhou, T. Zhang, F. Wang, and Y. Yu, "Performance analysis of a novel thermoelectric assisted indirect evaporative cooling system," *Energy,* vol. 162, pp. 299-308, 2018/11/01/ 2018.

[80] D. Meng, J. Lv, Y. Chen, H. Li, and X. Ma, "Visualized experimental investigation on cross-flow indirect evaporative cooler with condensation," *Applied Thermal Engineering,* vol. 145, pp. 165-173, 2018/12/25/ 2018.

[81] M. Guilizzoni, S. Milani, P. Liberati, and S. De Antonellis, "Effect of plates coating on performance of an indirect evaporative cooling system," *International Journal of Refrigeration,* vol. 104, pp. 367-375, 2019/08/01/ 2019.

[82] A. Khandelwal, P. Talukdar, and S. Jain, "Energy savings in a building using regenerative evaporative cooling," *Energy and Buildings,* vol. 43, no. 2, pp. 581-591, 2011/02/01/ 2011.

[83] C. Hutter, D. Büchi, V. Zuber, and P. Rudolf von Rohr, "Heat transfer in metal foams and designed porous media," *Chemical Engineering Science,* vol. 66, no. 17, pp. 3806-3814, 2011/09/01/ 2011.

[84] C.-C. Chen and P.-C. Huang, "Numerical study of heat transfer enhancement for a novel flat-plate solar water collector using metal-foam blocks," *International Journal of Heat and Mass Transfer,* vol. 55, no. 23, pp. 6734-6756, 2012/11/01/ 2012.

[85] J. Lv, H. Xu, M. Zhu, Y. Dai, H. Liu, and Z. Li, "The performance and model of porous materials in the indirect evaporative cooling system: A review," *Journal of Building Engineering,* vol. 41, p. 102741, 2021/09/01/ 2021.

[86] S. Rashidi, M. H. Kashefi, K. C. Kim, and O. Samimi-Abianeh, "Potentials of porous materials for energy management in heat exchangers – A comprehensive review," *Applied Energy,* vol. 243, pp. 206-232, 2019/06/01/ 2019.

[87] R. Boukhanouf, A. Alharbi, H. G. Ibrahim, O. Amer, and M. Worall, "Computer modelling and experimental investigation of building integrated sub-wet bulb temperature evaporative cooling system," *Applied Thermal Engineering,* vol. 115, pp. 201-211, 2017/03/25/ 2017.

[88] Y. Chen, H. Yan, and Y. Min, "Visualized study of wetting enhancement and thermal performance of fiber-coated indirect evaporative cooler," *Applied Thermal Engineering,* vol. 221, p. 119904, 2023/02/25/ 2023.

[89] Z. Duan, X. Zhao, C. Zhan, X. Dong, and H. Chen, "Energy saving potential of a counter-flow regenerative evaporative cooler for various climates of China: Experiment-based evaluation," *Energy and Buildings,* vol. 148, pp. 199-210, 2017/08/01/ 2017.

[90] L. Jia, J. Liu, C. Wang, X. Cao, and Z. Zhang, "Study of the thermal performance of a novel dew point evaporative cooler," *Applied Thermal Engineering,* vol. 160, p. 114069, 2019/09/01/ 2019.

[91] C. Zhan, Z. Duan, X. Zhao, S. Smith, H. Jin, and S. Riffat, "Comparative study of the performance of the M-cycle counter-flow and cross-flow heat exchangers for indirect evaporative cooling – Paving the path toward sustainable cooling of buildings," *Energy,* vol. 36, no. 12, pp. 6790-6805, 2011/12/01/ 2011.

[92] Z. Duan, C. Zhan, X. Zhao, and X. Dong, "Experimental study of a counter-flow regenerative evaporative cooler," *Building and Environment,* vol. 104, pp. 47-58, 2016/08/01/ 2016.

[93] Y. Golizadeh Akhlaghi *et al.*, "A constraint multi-objective evolutionary optimization of a state-of-the-art dew point cooler using digital twins," *Energy Conversion and Management,* vol. 211, p. 112772, 2020/05/01/ 2020.

[94] S. Kashyap, J. Sarkar, and A. Kumar, "Effect of surface modifications and using hybrid nanofluids on energy-exergy performance of regenerative evaporative cooler," *Building and Environment,* vol. 189, p. 107507, 2021/02/01/ 2021.

[95] Y. Min, W. Shi, B. Shen, Y. Chen, and H. Yang, "Enhancing the cooling and dehumidification performance of indirect evaporative cooler by hydrophobic-coated primary

air channels," *International Journal of Heat and Mass Transfer,* vol. 179, p. 121733, 2021/11/01/ 2021.

[96] S. Kashyap, J. Sarkar, and A. Kumar, "Performance enhancement of regenerative evaporative cooler by surface alterations and using ternary hybrid nanofluids," *Energy,* vol. 225, p. 120199, 2021/06/15/ 2021.

[97] R. Tariq, C. Zhan, N. Ahmed Sheikh, and X. Zhao, "Thermal Performance Enhancement of a Cross-Flow-Type Maisotsenko Heat and Mass Exchanger Using Various Nanofluids," *Energies*, vol. 11, no. 10, 2018.

[98] Y. Chen, H. Yan, and Y. Pan, "Wetting and evaporative performance analysis of wet channels in indirect evaporative cooler with hydrophilic nano-coating," *Applied Thermal Engineering,* vol. 229, p. 120622, 2023/07/05/ 2023.

[99] F. Wang, C. Liang, and X. Zhang, "Research of anti-frosting technology in refrigeration and air conditioning fields: A review," *Renewable and Sustainable Energy Reviews,* vol. 81, pp. 707-722, 2018/01/01/ 2018.

[100] D. Zhuang, G. Ding, H. Hu, H. Fujino, and S. Inoue, "Condensing droplet behaviors on fin surface under dehumidifying condition. Part II: Experimental validation," *Applied Thermal Engineering,* vol. 105, pp. 345-352, 2016/07/25/ 2016.

[101] Y. Min, Y. Chen, and H. Yang, "Investigation on dynamic behaviour of condensation heat transfer in indirective evaporative cooler," *Indoor + built environment,* vol. 31, no. 8, pp. 2024-2035, 2022.

[102] E. Velasco Gómez, A. Tejero González, and F. J. Rey Martínez, "Experimental characterisation of an indirect evaporative cooling prototype in two operating modes," *Applied Energy,* vol. 97, pp. 340-346, 2012/09/01/ 2012.

[103] S.-W. Ham and J.-W. Jeong, "DPHX (dew point evaporative heat exchanger): System design and performance analysis," *Energy,* vol. 101, pp. 132-145, 2016/04/15/ 2016.

[104] H.-J. Kim, S.-W. Ham, D.-S. Yoon, and J.-W. Jeong, "Cooling performance measurement of two cross-flow indirect evaporative coolers in general and regenerative operation modes," *Applied Energy,* vol. 195, pp. 268-277, 2017/06/01/ 2017.

[105] A. Y. T. Al-Zubaydi and G. Hong, "Experimental study of a novel water-spraying configuration in indirect evaporative cooling," *Applied Thermal Engineering,* vol. 151, pp. 283-293, 2019/03/25/ 2019.

[106] R. Ramkumar, "Experimental investigation of indirect evaporative cooler using clay pipe," *Journal of Thermal Engineering,* vol. 3, pp. 1163-1163, 04/01 2017.

[107] N.-H. Kim, "Performance of an indirect evaporative cooler (IEC) made of PET/cellulose composite sheet as wetting media," *Applied Thermal Engineering,* vol. 186, p. 116492, 2021/03/05/ 2021.

[108] S. De Antonellis, C. M. Joppolo, and P. Liberati, "Performance measurement of a cross-flow indirect evaporative cooler: Effect of water nozzles and airflows arrangement," *Energy and Buildings,* vol. 184, pp. 114-121, 2019/02/01/ 2019.

[109] T. Sun, X. Huang, Y. Chen, and H. Zhang, "Experimental investigation of water spraying in an indirect evaporative cooler from nozzle type and spray strategy perspectives," *Energy and Buildings*, vol. 214, p. 109871, 2020/05/01/ 2020.

[110] S. O. L. Lacour, F. Trinquet, P. E. Vendee, A. Vallet, A. Delahaye, and L. Fournaison, "Assessment of the wet area of a heat exchanger exposed to a water spray," *Applied Thermal Engineering,* vol. 128, pp. 434-443, 2018/01/05/ 2018.

[111] H. Montazeri, B. Blocken, and J. L. M. Hensen, "Evaporative cooling by water spray systems: CFD simulation, experimental validation and sensitivity analysis," *Building and Environment*, vol. 83, pp. 129-141, 2015/01/01/ 2015.

[112] X. Ma, W. Shi, and H. Yang, "Study on water spraying distribution to improve the energy recovery performance of indirect evaporative coolers with nozzle arrangement optimization," *Applied Energy,* vol. 318, 2022.

[113] F. Habashi, "Nickel, Physical and Chemical Properties." New York, NY: Springer New York, pp. 1520-1520.

[114] K. H. Lo, C. H. Shek, and J. K. L. Lai, "Recent developments in stainless steels," *Materials Science and Engineering: R: Reports,* vol. 65, no. 4, pp. 39-104, 2009/05/29/ 2009.

[115] F. Habashi, "Nickel, Physical and Chemical Properties," in *Encyclopedia of Metalloproteins*, R. H. Kretsinger, V. N. Uversky, and E. A. Permyakov, Eds. New York, NY: Springer New York, 2013, pp. 1520-1520.

[116] J. W. Gooch, "Stainless Steel," in *Encyclopedic Dictionary of Polymers*, J. W. Gooch, Ed. New York, NY: Springer New York, 2011, pp. 695-695.

[117] A. Khursheed, *Scanning electron microscope optics and spectrometers*. Singapore ;: World Scientific, 2011.

[118] K. Y. Law, "Definitions for Hydrophilicity, Hydrophobicity, and Superhydrophobicity: Getting the Basics Right," *J Phys Chem Lett,* vol. 5, no. 4, pp. 686-8, Feb 20 2014.

[119] B. Zheng, C. Guo, T. Chen, Q. Shi, J. Lv, and Y. You, "Development of an experimental validated model of cross-flow indirect evaporative cooler with condensation," *Applied Energy,* vol. 252, p. 113438, 2019/10/15/ 2019.

[120] C. Geffray *et al.*, "8 - Verification and validation and uncertainty quantification," in *Thermal Hydraulics Aspects of Liquid Metal Cooled Nuclear Reactors*, F. Roelofs, Ed.: Woodhead Publishing, 2019, pp. 383-405.

[121] H. W. Coleman and W. G. Steele, *Experimentation, validation, and uncertainty analysis for engineers,* Fourth edition. ed. Hoboken, NJ, USA: Wiley, 2018.

[122] J. Lin, D. T. Bui, R. Wang, and K. J. Chua, "On the fundamental heat and mass transfer analysis of the counter-flow dew point evaporative cooler," *Applied Energy,* vol. 217, pp. 126-142, 2018/05/01/ 2018.

[123] E. Purlis, "Modelling convective drying of foods: A multiphase porous media model considering heat of sorption," *Journal of Food Engineering*, vol. 263, pp. 132-146, 2019/12/01/ 2019.

[124] Y. Yang, C. Ren, C. Yang, M. Tu, B. Luo, and J. Fu, "Energy and exergy performance comparison of conventional, dew point and new external-cooling indirect evaporative coolers," *Energy Conversion and Management*, vol. 230, p. 113824, 2021/02/15/ 2021.

[125] Y. Zhu, P. Wang, D. Sun, Z. Qu, and B. Yu, "Multiphase porous media model with thermo-hydro and mechanical bidirectional coupling for food convective drying," *International Journal of Heat and Mass Transfer,* vol. 175, p. 121356, 2021/08/01/ 2021.

[126] T. Su, Z. Zhang, J. Han, S. Zhang, X. Wang, and W. Zhang, "Sensitivity analysis of intermittent microwave convective drying based on multiphase porous media models," *International Journal of Thermal Sciences,* vol. 153, p. 106344, 2020/07/01/ 2020.

[127] W. Chen, Y. Wang, D. Wang, Y. Liu, and J. Liu, "Predicting the effective thermal conductivity of porous building materials using improved Menger sponge fractal structure," *International Journal of Thermal Sciences,* vol. 184, p. 107985, 2023/02/01/ 2023.

[128] N. Popham, "Resin infusion for the manufacture of large composite structures," *Marine Composites: Design and Performance; Pemberton, R., Summerscales, J., Graham-Jones, J., Eds,* pp. 227-268, 2019.

[129] M. Kaviany, *Principles of heat transfer in porous media*, 2nd ed. ed. (Mechanical engineering series.). New York ;: Springer-Verlag, 1995.

[130] A. K. Datta, "Porous media approaches to studying simultaneous heat and mass transfer in food processes. II: Property data and representative results," *Journal of Food Engineering,* vol. 80, no. 1, pp. 96-110, 2007/05/01/ 2007.

[131] W. Liu, A. Fan, and X. Huang, *Theory and application of heat and mass transfer in porous media*. Science Press, 2006.

[132] C. Kumar, "Modelling intermittent microwave convective drying (IMCD) of food materials," 2015.

[133] L. Hou, R. Li, S. Wang, and A. K. Datta, "Numerical analysis of heat and mass transfers during intermittent microwave drying of Chinese jujube (Zizyphus jujuba Miller)," *Food and bioproducts processing,* vol. 129, pp. 10-23, 2021.

[134] M. Tabatabaian, *Comsol®5 for engineers* (Comsol® 5 for engineers). Dulles, Virginia: Mercury Learning and Information, 2016.

[135] I. S. D. Patrick Amestoy, Jean-Yves L'Excellent, J. Koster, "MUltifrontal Massively Parallel Solver (MUMPS version 4.2 beta) user's guide," *LIP TR-2002-02, Laboratoire de l'informatique du parallélisme.,* 2022.

[136] H. Wang and Z. J. Zhai, "Analyzing grid independency and numerical viscosity of computational fluid dynamics for indoor environment applications," *Building and environment,* vol. 52, pp. 107-118, 2012.

[137] Y. Chen, H. Yang, and Y. Luo, "Indirect evaporative cooler considering condensation from primary air: Model development and parameter analysis," *Building and Environment,* vol. 95, pp. 330-345, 2016/01/01/ 2016.

[138] P. H. Jadhav and G. N, "Optimum design of heat exchanging device for efficient heat absorption using high porosity metal foams," *International Communications in Heat and Mass Transfer,* vol. 126, p. 105475, 2021/07/01/ 2021.

[139] U. Kemerli and K. Kahveci, "Forced convection in finned metal foams: The effects of porosity and effective thermal conductivity," *International Journal of Thermal Sciences,* vol. 161, p. 106756, 2021/03/01/ 2021.

[140] P. H. Jadhav, N. Gnanasekaran, D. A. Perumal, and M. Mobedi, "Performance evaluation of partially filled high porosity metal foam configurations in a pipe," *Applied Thermal Engineering,* vol. 194, p. 117081, 2021/07/25/ 2021.

[141] W. Yan, X. Meng, X. Cui, Y. Liu, Q. Chen, and L. Jin, "Evaporative cooling performance prediction and multi-objective optimization for hollow fiber membrane module using response surface methodology," *Applied Energy,* vol. 325, p. 119855, 2022/11/01/ 2022.

[142] R. L. Wasserstein and N. A. Lazar, "The ASA's Statement on p-Values: Context, Process, and Purpose," *The American statistician,* vol. 70, no. 2, pp. 129-133, 2016.

[143] M. H. Kutner, *Applied linear statistical models*, 5th ed. / Michael H. Kutner ... [et al.]. ed. (McGraw-Hill/Irwin series operations and decision sciences). Boston: McGraw-Hill Irwin, 2005.

[144] T. P. Ryan, *Modern regression methods* (Modern Regression Methods). John Wiley & Sons, Inc., 2018.

[145] S. Wellek, *Testing statistical hypotheses of equivalence and noninferiority*, 2nd ed. ed. Boca Raton: CRC Press, 2010.

[146] DesignExpert. (2023, 1st May). *DesignExpert* [Online]. Available: https://www.statease.com/software/design-expert/.

[147] R. Vijayakumar and N. Pannirselvam, "Employing desirability function analysis for the multi-response optimisation of mild steel embossed plate shear connector using Taguchi technique," *Sustainable Energy Technologies and Assessments,* vol. 54, p. 102863, 2022/12/01/ 2022.

[148] B. Şimşek, T. Uygunoğlu, H. Korucu, and M. M. Kocakerim, "Analysis of the effects of dioctyl terephthalate obtained from polyethylene terephthalate wastes on concrete mortar: A response surface methodology based desirability function approach application," *Journal of Cleaner Production,* vol. 170, pp. 437-445, 2018/01/01/ 2018.

[149] R. Kumar, "Effects of high volume dolomite sludge on the properties of eco-efficient lightweight concrete: Microstructure, statistical modeling, multi-attribute optimization through Derringer's desirability function, and life cycle assessment," *Journal of Cleaner Production,* vol. 307, p. 127107, 2021/07/20/ 2021.

[150] W. Shi, H. Yang, X. Ma, and X. Liu, "A novel indirect evaporative cooler with porous media under dual spraying modes: A comparative analysis from energy, exergy, and environmental perspectives," *Journal of Building Engineering,* p. 106874, 2023/05/18/ 2023.

[151] A. M. Blanco-Marigorta, A. Tejero-González, J. M. Rey-Hernández, E. Velasco Gómez, and R. Gaggioli, "Exergy analysis of two indirect evaporative cooling experimental prototypes," *Alexandria Engineering Journal,* vol. 61, no. 6, pp. 4359-4369, 2022/06/01/ 2022.

[152] Y. Cui, J. Zhu, S. Zoras, and L. Liu, "Review of the recent advances in dew point evaporative cooling technology: 3E (energy, economic and environmental) assessments," *Renewable and Sustainable Energy Reviews,* vol. 148, p. 111345, 2021/09/01/ 2021.

[153] A. Adam, D. Han, W. He, M. Amidpour, and H. Zhong, "Numerical investigation of the heat and mass transfer process within a cross-flow indirect evaporative cooling system for hot and humid climates," *Journal of Building Engineering,* vol. 45, p. 103499, 2022/01/01/ 2022.

[154] P. Xu, X. Ma, X. Zhao, and K. S. Fancey, "Experimental investigation on performance of fabrics for indirect evaporative cooling applications," *Building and Environment,* vol. 110, pp. 104-114, 2016/12/01/ 2016.

[155] A. Badiei, Y. G. Akhlaghi, X. Zhao, J. Li, F. Yi, and Z. Wang, "Can whole building energy models outperform numerical models, when forecasting performance of indirect evaporative cooling systems?," *Energy Conversion and Management,* vol. 213, p. 112886, 2020/06/01/ 2020.

[156] S. Kashyap, J. Sarkar, and A. Kumar, "Exergy, economic, environmental and sustainability analyses of possible regenerative evaporative cooling device topologies," *Building and Environment,* vol. 180, p. 107033, 2020/08/01/ 2020.

[157] M. Farmahini-Farahani, S. Delfani, and J. Esmaeelian, "Exergy analysis of evaporative cooling to select the optimum system in diverse climates," *Energy*, vol. 40, no. 1, pp. 250-257, 2012/04/01/ 2012.

[158] R. Chengqin, L. Nianping, and T. Guangfa, "Principles of exergy analysis in HVAC and evaluation of evaporative cooling schemes," *Building and Environment*, vol. 37, no. 11, pp. 1045-1055, 2002/11/01/ 2002.

[159] T. A. H. Ratlamwala and I. Dincer, "Efficiency assessment of key psychometric processes," *International Journal of Refrigeration*, vol. 36, no. 3, pp. 1142-1153, 2013/05/01/ 2013.

[160] H. Caliskan, I. Dincer, and A. Hepbasli, "A comparative study on energetic, exergetic and environmental performance assessments of novel M-Cycle based air coolers for buildings," *Energy Conversion and Management*, vol. 56, pp. 69-79, 2012/04/01/ 2012.

[161] H. Caliskan, I. Dincer, and A. Hepbasli, "Exergoeconomic, enviroeconomic and sustainability analyses of a novel air cooler," *Energy and Buildings*, vol. 55, pp. 747-756, 2012/12/01/ 2012.

[162] J. Lin, D. T. Bui, R. Wang, and K. J. Chua, "On the exergy analysis of the counter-flow dew point evaporative cooler," *Energy*, vol. 165, pp. 958-971, 2018/12/15/ 2018.

[163] MEE, (2022, 9th May). *Notice on Key Work Related to the Management of Greenhouse Gas Emission Report of Enterprises in 2022* [Online]. Available: https://www.mee.gov.cn/xxgk2018/xxgk/xxgk06/202203/t20220315_971468.html.